Study of Spectral Signatures and Accretion Dynamics of Black Holes During Outbursts

A thesis submitted

in partial fulfillment for the award of the degree of

Doctor of Philosophy

by

Aneesha U

Department of Earth & Space Sciences

Indian Institute of Space Science and Technology

Thiruvananthapuram, India

September 2020

Certificate

This is to certify that the thesis titled ***Study of Spectral Signatures and Accretion Dynamics of Black Holes During Outbursts*** submitted by **Aneesha U**, to the Indian Institute of Space Science and Technology, Thiruvananthapuram, in partial fulfillment for the award of the degree of **Doctor of Philosophy** is a bona fide record of the original work carried out by him/her under my supervision. The contents of this thesis, in full or in parts, have not been submitted to any other Institute or University for the award of any degree or diploma.

Dr. Samir Mandal
Associate Professor

Dr Samir Mandal
Associate Professor & Head

Place: Thiruvananthapuram
Date: September 2020

Declaration

I declare that this thesis titled ***Study of Spectral Signatures and Accretion Dynamics of Black Holes During Outbursts*** submitted in partial fulfillment for the award of the degree of **Doctor of Philosophy** is a record of the original work carried out by me under the supervision of **Dr. Samir Mandal**, and has not formed the basis for the award of any degree, diploma, associateship, fellowship, or other titles in this or any other Institution or University of higher learning. In keeping with the ethical practice in reporting scientific information, due acknowledgments have been made wherever the findings of others have been cited.

Place: Thiruvananthapuram
Date: September 2020

Aneesha U
(SC14D007)

This thesis is dedicated to my mother

Acknowledgements

I would like to express my gratitude to all those who supported me and helped while I was writing this thesis.

First of all, I thank IIST for giving me the opportunity to do the research work and providing the research atmosphere. I thank the Director IIST for providing the needed facilities for completion of the thesis work.

I would like to express my sincere gratitude to my research supervisor Dr. Samir mandal for his patient guidance, positive criticism of my work, and useful advice. He always supported me during every worse moment and gave me a helping hand whenever I needed.

I would like to express my very great appreciation to Dr Anuj Nandi who is also my doctoral committee member for the useful feedback of my work. I also thank my collaborators H Sreehari and D Radhika, Tilak B. Katoch for the support they extended for the work progress.

The useful suggestions from my doctoral committee members Dr. Gulab Dewangan, Dr. Anandmayee Tej, Dr. Resmi Lekshmi, and Dr. Umesh R. Kadhane helped me to improve the quality of my work. I also thank Dr. Anand Narayanan, Dr. Jagadheep D, and Dr. Sarita Vig for the support they provided.

I thank all my friends Dhanya, Arun, Praveen, Deepak, Joel, Sachin, Swagat, Veena, Namitha, Dinil, Geethu, Anna, Sreelakshmi, Babitha, Sai Krishnan, and Shalini who made my Ph.D. life so lively and memorable. I will always remember the evening tea at the ISRO junction, Friday dinner at the kammalam restaurant, Saturday movies at the Rani theatre, morning breakfast at the chechi's shop, and the cooking experiments.

I am grateful to my relatives and neighbours who provided me the internet support for the completion of the thesis during the lockdown days. I also thank my cousins who gave me the mental support during the stressful situations. Finally, I thank my mother, father, and brother for being always with me.

Abstract

Unlike other astrophysical objects, black holes cannot be observed directly using electromagnetic radiation. In a binary system, a black hole can accrete material from the companion star due to its extreme gravity. The accreted matter releases a huge amount of potential energy and a fraction of this is emitted as radiation, mainly in X-ray. Therefore, the study of the nature of X-ray radiation is important to understand the underline accretion process. Black hole X-ray binaries can be persistent showing continuous X-ray activity or transient which exhibits occasional outburst in between long quiescent phases. In this thesis, we attempt to understand the accretion physics around outbursting as well as persistent black hole X-ray binaries through spectral studies utilising various X-ray instruments data.

In Chapter 1, we introduce the astrophysical compact objects and X-ray binaries (XRBs) in general, with particular emphasis on black hole XRBs. We provide an outline on accretion around compact objects via Roche lobe overflow as well as wind accretion. Also, we make an effort to summarize various accretion disc models discussed in the literature. Jet/outflow is an integral part of the accretion process and we have touched upon the jet characteristics to highlight X-ray-radio correlation. It is well accepted that the outburst process may trigger because of instability in the accretion disk. A short description of the disc instability model in presence of irradiation is presented. During the outburst, the source passes through different spectral states which are also mentioned. Finally, we present the motivation behind this thesis and selection of sources.

We have used the two-component accretion flow model extensively for spectral modelling of X-ray data. Therefore, in Chapter 2, we describe the essential insights of the two-component accretion model. We give a brief account of different radiation processes such as bremsstrahlung, Compton scattering and Synchrotron which are required to calculate the radiation spectrum. Few additional model components like, photoelectric absorption, and line emission, which is used for spectral modelling, are also discussed.

In Chapter 3, we highlight the key aspects of different space X-ray observatories (RXTE, XMM-Newton, Swift, AstroSat) whose data have been used in our study. We outline the data reduction techniques for individual X-ray instruments and tasks for extracting useful scientific products.

In Chapter 4, we aim to understand the accretion dynamics of H 1743-322 during outbursts. We analysed all the RXTE/PCA data during 2003-2011. We have performed phe-

nomenological spectral modelling and extract the spectral parameters. Similarly, we have done spectral modelling with two-component accretion model and estimated the accretion parameters. We study the evolution of spectral parameters and understand the spectral state transitions during outbursts. We model the accretion parameters evolution with a toy model and estimate the characteristic time scales that govern the dynamics of the outbursts. We employ the irradiated disc instability model in two-component accretion scenario to understand the evolution of the outburst. We discuss the issues regarding the two-component spectral modelling of 2003 outburst and understand the requirement of additional contribution from the jet. Also, we study the evolution of accretion dynamics with the activity of the jet observed in radio frequency.

In Chapter 5, we study the second outbursting source GX 339-4 having very different outbursts characteristics. We carry out both phenomenological and two-component spectral modelling of RXTE/PCA data over a period 2002-2012. Also, simultaneous broadband (Swift, RXTE, XMM-Newton) spectral studies are performed for better constrain on the spectral parameters. We connect the evolution of the spectral parameters with the accretion parameters. The evolution of the accretion rates is modelled with a logarithmic time variation. We provide a unified view of all the outbursts in the light of the irradiated disc instability picture. Finally, we discuss a possible physical scenario behind outbursts with short and long rise time.

To complement our work on outbursting sources, in Chapter 6 we study the spectral variability and accretion properties of two persistent sources GRS 1758-258 and 1E 1740.7-2942 using AstroSat observations during the period 2016-2018. Both these sources are close to the galactic centre and we discuss the contamination issues in AstroSat observations. We perform broadband spectral modelling of both the sources. The variation in the spectral parameters is discussed in connection with the same of the accretion parameters. We compare the behaviour of the persistent sources in the hardness intensity diagram with that of the outbursting sources studied in the previous chapters and connect the nature of the persistent source with the irradiation phase of the outbursting source.

In Chapter 7, we summarise the thesis work and indicate the future scope of the study.

Contents

List of Figures

List of Tables

Abbreviations

XRB	X-Ray Binary
DIM	Disc Instability Model
NS	Neutron Star
BH	Black Hole
ULX	Ultra Luminous X-ray Sources
UV	Ultra Violet
LMXB	Low Mass X-ray Binary
HMXB	High Mass X-ray Binary
AGN	Active Galactic Nuclei
FRED	Fast Rise Exponential Decay
FRSD	Fast Rise Slow Decay
SRSD	Slow Rise Slow Decay
PDS	Power Density Spectrum
QPO	Quasi Periodic Oscillation
LHS	Low Hard State
HIMS	Hard Intermediate State
SIMS	Soft Intermediate State
HSS	High Soft State
HID	Hardness Intensity Diagram
PSR	Post Shock Region
RXTE	Rossi X-ray Timing Explorer
ASM	All Sky Monitor
PCA	Proportional Counter Array
PCU	Proportional Counter Units
HEXTE	High Energy X-ray Timing Explorer
XMM	X-Ray Multi-Mirror Mission
EPIC	European Photon Imaging Cameras

OM	Optical Monitor
RGS	Reflection Grating Spectrometers
MOS	Metal Oxide Semi conductor
CCD	Charge Coupled Device
PSF	Point Spread Function
HPD	Half Power Diameter
BAT	Burst Alert Telescope
XRT	X-ray Telescope
UVOT	Ultraviolet/Optical Telescope
SXT	Soft X-ray Telescope
LAXPC	Large Area X-ray Proportional Counter
CZTI	Cadmium-Zinc-Telluride Imager
SSM	Scanning Sky Monitor
UVIT	Ultraviolet Imaging Telescope
FWHM	Full Width at Half Maximum
MJD	Modified Julian Date
FoV	Field of View
ARF	Ancillary Response File
RMF	Response Matrix File
IM	Imaging Mode
PD	PhotoDiode mode
WT	Windowed Timing mode
PC	Photon Counting mode
FW	Fast Windowed
BM	Bias Map
Cal	Calibration

Nomenclature

$\mathrm{M}_{\odot}$	Solar mass
$\mathrm{R}_{\odot}$	Solar radius
gm	Gram
cm	Centimeter
s	second
G	Gravitational constant
c	Velocity of light
k	Boltzmann constant
$\mathrm{T_e}$	Electron temperature
$\mathrm{T_p}$	Proton temperature
$\mathrm{m_e}$	Electron mass
$\mathrm{m_p}$	Proton mass
yr	year
Z	Atomic number
e	Charge
$\mathrm{g_{ff}}$	Gaunt factor
M	Mass of the compact object
$\mathrm{M_s}$	Mass of the companion star
$\mathrm{P_{orb}}$	Orbital period
$\mathrm{v_{sr}}$	Radial valocity of the secondary
L	Luminosity
η	Accretion efficiency
σ_{T}	Thomson scattering cross section
$\mathrm{L_{Edd}}$	Eddington luminosity
σ	Stefan-Boltzmann constant
x	Radial distance
$\mathrm{r_g}$	Schwarzschild radius

ρ	Mass density
P	Pressure
v	Radial velocity
γ_{a}	Adiabatic index
$\mathrm{c_s}$	Sound speed
$\mathrm{M_{Edd}}$	Eddington accretion rate
$\mathrm{T_{eff}}$	Effective temperature
$\mathrm{T_c}$	Colour temperature
ν	Frequency
h	Planck constant
H	Disc vertical height
Σ	Surface density
α_{vis}	Viscosity parameter
$\mathrm{m_{bh}}$	Mass of the accreting object in units of solar mass
$\mathcal{M}$	Mach number
λ	Specific angular momentum
i	Inclination angle
α	Spectral index
B	Magnetic field
θ_0	Pitch angle
γ	Lorentz factor
$\mathrm{n_H}$	Hydrogen column density
$\mathrm{T_{in}}$	Inner disc temperature
Γ_{p}	Photon index
$\dot{\mathrm{m}}_{\mathrm{d}}$	Keplerian accretion rate
$\dot{\mathrm{m}}_{\mathrm{h}}$	Sub Keplerian accretion rate
$\mathrm{x_s}$	Shock location
$\dot{\mathrm{m}}_{\mathrm{dc}}$	Critical accretion rate
$\mathrm{R_0}$	Outer radius of accretion disc
$\mathrm{f(M)}$	Mass function
D	Distance
a	Spin
q	Mass ratio
$\mathrm{t_r}$	Rising time of soft flux or $\dot{m}_d$
$\mathrm{t_h}$	Rising time of hard flux or $\dot{m}_h$

$\mathrm{t_d}$	Time scale after which $\dot{m}_d$ decline
$\mathrm{t_s}$	Time scale after which $\dot{m}_h$ & x_s starts to increase

Chapter 1

Introduction

In this chapter, we introduce compact objects and X-ray binary systems (XRBs) in general. We provide a brief description of accretion processes in XRBs and various accretion disc models. XRBs can be persistent or transient (outbursting) in nature. We introduce the disc instability model to study the outburst mechanism in XRBs. The X-ray spectral states observed in XRBs are defined.

1.1 Astrophysical Compact Objects

Stars appear to be static due to a delicate balance between force due to gravity and the gradient of pressure. But stars do evolve due to the nuclear burning at the core. The stellar interior becomes unstable against gravity at the end of nuclear burning and the collapsed core becomes a compact object: a white dwarf or a neutron star, or a black hole. A low mass main sequence star undergoes different evolutionary stages and finally, the stellar core becomes a white dwarf at the centre of a planetary nebula. White dwarfs are supported by electron degeneracy pressure. The observed mass of the white dwarfs is in the range $0.17M_{\odot} - 1.13M_{\odot}$ (Burleigh & Jordan, 1998; Kilic et al., 2007), though the theoretical limit of the maximum mass of a white dwarf is $1.44M_{\odot}$ (Chandrasekhar, 1939). More massive stars ($8M_{\odot} < M < 25M_{\odot}$), evolve faster and end their life through supernova events. The compact core forms a neutron star (NS) if the core survives against gravity due to the neutron degeneracy pressure. The observed estimate of the mass of neutron star lies in the range $1.15M_{\odot} - 2.4M_{\odot}$ (Lattimer, 2012). Rhoades & Ruffini (1974) predicted a maximum mass of neutron stars as $3.2M_{\odot}$ using the causality argument. Even more, massive stars ($M > 25M_{\odot}$) are expected to have core mass higher than neutron star and the core completely collapses into a singularity forming a black hole (BH). Since the final stage of the evolution of massive stars is poorly understood, the dividing line between the

Table 1.1: Properties of stellar compact objects

Object	Mass (M)	Radius (R)	Mean density ($\mathrm{gm/cm^3}$)	Surface potential (GM/Rc^2)
White dwarf	$\lesssim \mathrm{M}_\odot$	$\sim 10^{-2}\,\mathrm{R}_\odot$	$\leq 10^7$	$\sim 10^{-4}$
Neutron star	$\sim 1-3\,\mathrm{M}_\odot$	$\sim 10^{-5}\,\mathrm{R}_\odot$	$\leq 10^{15}$	$\sim 10^{-1}$
Black hole	$\gtrsim 3\mathrm{M}_\odot$	$\sim GM/c^2$	$\sim M/R^3$	~ 1

$\mathrm{M}_\odot = 1.98 \times 10^{33}$ gm, $\mathrm{R}_\odot = 6.95 \times 10^{10}$ cm

maximum mass of neutron stars and the minimum mass of black holes is very uncertain.

Black holes are possibly the simplest objects in the universe. They are characterised by the mass, rotational angular momentum and charge. There is no observational evidence of charged BHs because any excess charge possibly be neutralised very quickly. The rotational properties of a BH is represented by a dimensionless quantity called spin which scales between zero to unity. There is a region around the black hole, called event horizon, from where even light cannot escape and hence black holes can not be observed directly using electromagnetic wave. The size of the event horizon of a non-rotating BH (or Schwarzschild BH) is $r_g = 2GM/c^2$, where G is the universal gravitational constant, M is the mass of the BH and c is the speed of light in vacuum. Whereas the same for an extremely rotating BH (Kerr BH) reduces to GM/c^2. The observed estimates of the mass of BH in XRBs vary in the range $3 - 20M_\odot$ (Corral-Santana et al., 2016). Although there are other classes of BHs do exist in nature. It is generally believed that the centre of galaxies harbour supermassive black holes of masses ranging between a few million to a few billion solar mass. The luminosity scale of ultra-luminous X-ray sources (ULXs) indicate the possibility of intermediate mass BHs (Winter et al., 2006) of a few hundred to few thousands of solar mass. Though an independent estimation of the mass of the central source of ULXs is required to confirm the hypothesis.

A brief comparison of different characteristics of stellar compact objects is given in Table 1.1. The white dwarfs are brighter in optical/UV wavelength whereas neutron stars/black holes are luminous in X-ray due to very strong gravitational influence.

1.2 X-ray Binary System

X-ray binaries (XRBs) are binary systems where the primary is a core collapse compact object, either a neutron star (NSXRB) or a black hole (BHXRB). A stellar binary system can evolve into an XRB if the stellar remnant stayed gravitationally bound to the secondary companion star after the supernova event. In an alternate picture, the stellar remnant may

receive high kick velocity during the supernova explosion and may capture a companion star, forming an XRB system. The X-ray activity is a result of accretion of material from the companion star to the primary.

The accreted material hit the NS surface and produce thermal radiation. Therefore, the low energy X-ray radiation spectrum of NSXRB is a superposition of two thermal components: emission from the surface and the accretion disc. Whereas BH does not have a hard surface and the thermal emission comes from the accretion disc only. A rotating neutron star in XRB shows periodic X-ray pulses or oscillations in the X-ray bursts due to thermonuclear explosion on the surface of the accreting NS. Zdziarski (1998) have proposed that the X-ray spectrum extended beyond 50 keV is a signature of BHXRB. Whereas a typical plasma of temperature is $kT_e < 30\,\mathrm{keV}$ for NSXRBs, where k is Boltzmann constant and T_e is electron temperature. However, Piraino et al. (1999) has shown that the spectra of a neutron star source, 4U 0614+091, can extend beyond 220 keV. The power density spectra (PDS) of accreting black holes do not show much variability beyond 50 Hz whereas accreting neutron stars manifest strong variability above 500 Hz (Sunyaev & Revnivtsev, 2000).

XRBs can be classified as low mass X-ray binary (LMXBs) or high mass X-ray binary (HMXB) according to the mass of the donor star. In LMXB, the secondary is a low mass ($M_s \leq 1\,\mathrm{M}_\odot$), K-M spectral type star and is generally optically faint. Few examples of this category are Sco X-1, GRS 1915-102, GX 339-4 etc. In the case of HMXBs, the companion is early type massive O-B stars ($M_s \geq 10\,\mathrm{M}_\odot$) which are very luminous. The X-ray sources such as Cen X-3, Cyg X-1, LMC X-1 etc. fall into the HMXB category. A few XRBs accrete material from B-F spectral type stars which are having intermediate mass, say for example Her X-1. These intermediate mass X-ray binary systems (Hopman et al., 2004; Portegies Zwart et al., 2004) are thought to be the progenitors of some LMXBs through episodes of enhanced mass transfer.

LMXBs and HMXBs show differences in their characteristics due to the large difference in the companion mass. The lifespan of HMXBs are short around $\sim 10^5 - 10^7\,\mathrm{yr}$ since the massive companion evolve faster, whereas the same for the LMXBs is longer around $10^7 - 10^9\,\mathrm{yr}$. This results in the distribution of HMXBs along the galactic plane associated with young stellar populations whereas LMXBs are found towards the galactic centre, galactic bulge, galactic plane, and in globular clusters. The distributions of the HMXBs and LMXBs in the sky are shown in Figure 1.1.

Both LMXBs and HMXBs appear as either persistent or transient sources. The WATCHDOG catalogue (Tetarenko et al., 2016) has listed 66 transient and 11 persistent black hole

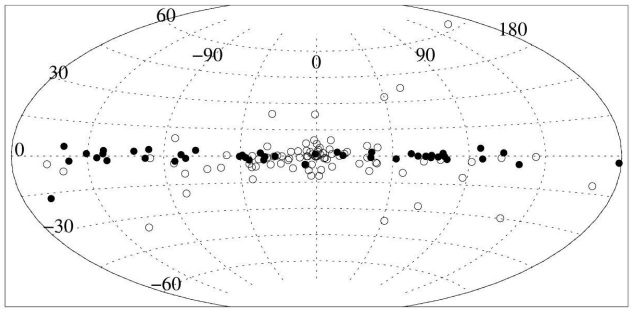

Figure 1.1: Distribution of XRBs on the sky in galactic coordinates. Note that significant concentration of HMXBs (filled circles) towards the galactic plane and the clustering of LMXBs (open circles) in the galactic bulge (credit : Grimm et al. (2002)).

XRBs. The persistent sources say example Cyg X-1 and LMC X-3, always have detectable X-ray fluxes. On the other hand, transient sources, example GX 339-4, H 1743-322, are characterized by a long period of inactivity (quiescence), lasting over months to years (Parmar et al., 1995; Tanaka & Shibazaki, 1996; Hameury & Lasota, 2016; Tetarenko et al., 2016), separated by short period outbursts (Lochner & Roussel-Dupre, 1994; Tetarenko et al., 2016). During outbursts, their X-ray brightness increases by several orders of magnitudes. X-ray transients in quiescence usually show a very low X-ray flux because possibly, the accretion rate onto the compact object is smaller than the mass transfer from the secondary to the accretion disc. In a few cases, the optical emission shows a 'hot-spot' (Hynes, 2010) where the mass transferring stream from the companion impacts with the edge of the accretion disc around the compact object. These observations show that accretion disc is present in quiescence and it is possible to calculate the mass transfer rate from the brightness of the hot spot.

Since the discovery of Cyg X-1, the first detection of BH source in the early seventies, several stellar-mass black holes (Tetarenko et al., 2016) have been identified in XRBs. Even then the observational identification of black holes is not straightforward and the most reliable method to estimate the mass of the compact object is based on the mass function of the systems. In the following section, we discuss briefly the dynamical method of mass estimation to reveal the nature of the compact object.

1.2.1 Identification of Black Holes in XRBs

In a binary system the mass function (Frank et al., 1992) of the primary is given by,

$$f(M) = \frac{M^3 \sin^3 i}{(M + M_s)^2} = \frac{P_{orb} v_{sr}^3}{2\pi G} \tag{1.1}$$

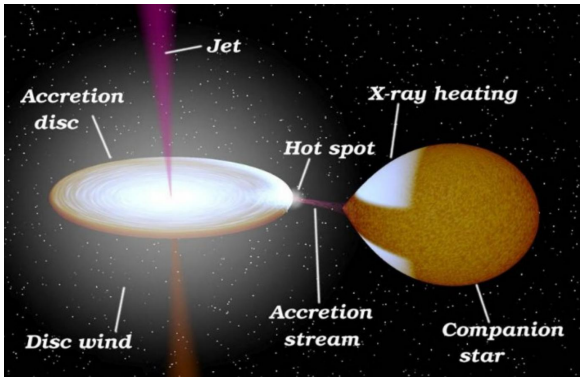

Figure 1.2: Artists impression of an X-ray binary that shows the accretion disc surrounding a black hole. (credit : NASA/R. Hynes)

where M, M_s are the masses of the compact object and the companion star respectively, and i represents the binary inclination angle. The orbital period (P_{orb}) and the semi amplitude of radial velocity (v_{sr}) of the secondary are optically measurable quantities. The mass function provides a lower limit on the mass of the primary. In XRBs with $f(M) \gtrsim 3M_{\odot}$ can be identified as black hole XRBs. The true mass of the primary can be estimated dynamically if i and M_s are known from spectroscopic and photometric measurements. In LMXB, the companion star is very faint and therefore the optical search for the secondary is practically impossible. Although, the nova-like optical brightening (Alfonso-Garzón et al., 2018) during the X-ray outburst in LMXB, allows the identification of the optical counterpart when the X-ray activity returns to quiescence. Whereas the companion star in HMXB is optically bright which makes the estimation of the orbital parameters easier.

1.3 Accretion onto Compact Objects

During the middle of the twentieth century, it was realised that the gravity power the most luminous objects in the universe. The infall of matter from the surrounding medium to the compact objects due to strong gravity is known as the accretion process. The release of the gravitational potential energy of the accreted matter onto the gravitating body is the main source of power in the compact binary systems, active galactic nuclei (AGN) and quasars. An artistic representation of the accretion process in an XRB is shown in Figure 1.2. The extreme compactness of these sources makes the accretion process more powerful than nuclear fusion in a star. In the Newtonian picture, the resulting luminosity (L) is equal to the rate of gravitational energy release i.e., $L = GM\dot{M}/2R$, where M is the mass of the compact object, $\dot{M} = dM/dt$ is the accretion rate and R is the size of the object. This

radiated luminosity is a fraction (η) of the available energy i.e., $L = \eta \dot{M} c^2$ (Frank et al., 1992) where the accretion efficiency is defined as $\eta = GM/2Rc^2$. A typical value of $\eta \sim 10^{-4}$ for a white dwarf and $\eta \sim 0.1$ for a neutron star whereas the same varies between $0.06 - 0.4$ in the case of a black hole depending on the spin of the object and the type of accretion flow.

The protons in the accreted matter experience the effect of gravity whereas the radiated luminosity exerts a force on the electrons due to the scattering with the photons. Since electrons and protons are coupled via Coulomb interaction, there is a maximum luminosity beyond which force due to radiation will push the accreting matter outward rather than falling onto the object. In the simplistic picture of spherical accretion, the inward gravitational force on the protons, GMm_p/R^2, at a radial distance R will be balanced by the force due to radiation, $\sigma_T L_{\rm max}/4\pi R^2 c$, at the maximum luminosity ($L_{\rm max}$). Here, σ_T is the Thomson scattering cross-section and m_p is the mass of the proton. This maximum luminosity is called the Eddington luminosity and is defined as,

$$L_{Edd} = \frac{4\pi G M m_p c}{\sigma_T} = 1.3 \times 10^{38} \Big(\frac{M}{M_\odot}\Big) \quad {\rm erg\,s^{-1}} \tag{1.2}$$

The luminosity of AGNs, quasars are observed as high as $\sim 10^{47}$ erg s^{-1}, and usually attributed to the accretion onto a supermassive BH ($M \sim 10^9 M_\odot$). The existence of the Eddington luminosity provides a maximum accretion rate $\dot{M}_{Edd} = L_{Edd}/\eta c^2$ for an accreting compact object. A typical value of $\dot{M}_{Edd} \sim 1.3 \times 10^{18}$ g s^{-1} for $M = 1\,M_\odot$ with $\eta = 0.1$. It is important to note that, the Eddington limit applies only to spherically symmetrical accretion and the flow can even be super-Eddington with more complicated geometry. Also, Eddington luminosity provides a characteristic temperature (T_b) if the emission process is assumed like a blackbody, i.e., $T_b = \left(\frac{L_{Edd}}{4\pi R^2 \sigma}\right)^{1/4}$, where σ is the Stefan-Boltzmann constant. Therefore, the typical accretion disc temperature $T_b \sim 10^7$ K for $1\,M_\odot$ object and expect the accretion disc would be luminous in X-ray (~ 1 keV). In a thermal medium, the virial argument, $GMm_p/2R = 3kT_{th}$, offers possibly an upper limit on the temperature (T_{th}) of the accreting plasma as $T_{th} < 10^{12}$ K.

The accretion process in LMXBs and HMXBs are significantly different due to the nature of the companion star. In HMXBs, the O/B type secondary star produces strong stellar wind and the compact object passes through the stellar wind while revolving around the companion. Therefore, the wind material is gravitationally captured by the compact primary and is called wind accretion. This process is generally very inefficient as only a very tiny fraction of the material is accreted by the primary. Also, the process is radiatively

inefficient as the accreted material is having a very low angular momentum. Whereas the accretion in LMXBs happens through Roche lobe overflow. In a binary system, the Roche lobe defines an equipotential surface around a star such that the stellar material within the Roche lobe remains gravitationally bound to the star. The Roche lobes of the individual stars cross each other at a saddle type point, the first Lagrangian point (L_1), where the resultant force on a test mass is zero. During the stellar evolution, the companion star (spectral type K-M) can expand or the binary separation can shrink such that the stellar surface fills the Roche lobe. As a result, matter from the companion can freely pass through the L_1 point and enter into the Roche lobe of the compact primary. In this case, accreted matter posses a Keplerian angular momentum as this was co-rotating with the companion before crossing the L_1 point. In the next section, we provide brief descriptions of the accretion processes having both low and high angular momentum.

1.3.1 Spherical Accretion

The spherically symmetric accretion of matter around a gravitating object was first studied by Bondi (1952). In this case, the accreting matter does not possess any angular momentum and the flow is having a large radial velocity. A Bondi type accretion may be applicable to an isolated compact object surrounded by a large density of stellar material. Assume a compact object of mass M surrounded by a medium with uniform density ρ_∞ and pressure P_∞ at a large distance from the compact object. Ignoring the self-gravity of the accreting matter, the momentum conservation equation is

$$v\frac{dv}{dx} + \frac{1}{\rho}\frac{dP}{dx} + \frac{1}{2x^2} = 0, \tag{1.3}$$

where x is the radial distance of the flow in units of Schwarzschild radius ($r_g = 2GM/c^2$), ρ is the mass density of the flow, P is gas pressure and v is the radial flow velocity expressed in unit of speed of light in vacuum. Here, a Newtonian prescription of gravity is considered. In the steady state, the equation of mass conservation reduces to

$$\dot{M} = 4\pi x^2 \rho(x) v(x). \tag{1.4}$$

Here, the $v(x)$ is negative which indicates an infall of matter and the accretion rate ($\dot{M}$) is a constant of motion. For simplicity, the accretion flow is assumed to be adiabatic, $P \propto \rho^{\gamma_a}$ where γ_a is the adiabatic index of the flow. Substituting the radial derivative of Equation

(1.4) into Equation (1.3), the well-known Bondi wind equation is derived as,

$$\frac{1}{2}\left(1-\frac{c_s^2}{v^2}\right)\frac{d}{dx}v^2 = -\frac{1}{2x^2}\left(1-4xc_s^2\right), \tag{1.5}$$

where the sound speed is defined as, $c_s = (\gamma_a \frac{P}{\rho})^{1/2}$. Equation (1.5) represents many different types of solutions (Frank et al., 1992) but here we focus only on the accretion solution. At a distance far from the central object, the right hand side of Equation (1.5) is positive as the sound speed reaches a steady value $c_{s\infty} = (\gamma_a \frac{P_\infty}{\rho_\infty})^{1/2}$ and velocity of the flow is negligible i.e., the flow is sub-sonic ($v^2 < c_s^2$). Whereas, the flow becomes supersonic ($v^2 > c_s^2$) close to the central object. Then the flow must cross the sonic point, $x = x_c$ where the velocity of the flow becomes velocity of sound ($v^2 = c_s^2$). Therefore, the accretion flow is essentially transonic in nature. In an adiabatic Bondi flow, the sonic point can uniquely be characterised by the parameters at infinity. The sound speed at sonic point is $c_s(x_c) = c_{s\infty}(\frac{2}{5-3\gamma_a})^{1/2}$ and $x_c = \frac{1}{4c_s^2(x_c)}$. Similarly, the mass accretion rate is expressed as,

$$\dot{M} = 1.4\times10^{11}\left(\frac{M}{M_\odot}\right)^2\left(\frac{\rho_\infty}{10^{-24}\,\mathrm{gm\,cm^{-3}}}\right)\left(\frac{c_{s\infty}}{10\,\mathrm{km\,s^{-1}}}\right)^{-3}\mathrm{gm\,s^{-1}}. \tag{1.6}$$

This amounts to a $10^{11}\,\mathrm{gm\,s^{-1}}$ or $10^{-7}\dot{M}_{Edd}$ of mass accretion around a $1\,\mathrm{M}_\odot$ object for typical values of interstellar medium parameters. Hence, accretion efficiency of Bondi flow is very low. Also the flow is radiatively very inefficient as the matter is having very high radial velocity. As a result, this model could not able to explain the observed luminosity of quasars and active galactic nuclei (AGNs). To address these issues Shakura and Sunyaev proposed an accretion disc model in 1973, commonly known as the standard accretion disc model, which we briefly discussed in the next section.

1.3.2 Standard Accretion Disc

In the standard scenario (Shakura & Sunyaev, 1973), the accretion of matter from the binary companion forms an accretion disc on the equatorial plane of the binary system. It is generally assumed that the angular momentum distribution of matter follow Keplerian orbits and the local viscosity transfer angular momentum outwards results in the accretion of matter to the compact object. The accretion disc is optically thick, and the local viscous dissipated energy is radiated away as a blackbody. So the accretion disc radiation spectrum will be the combination of the blackbody spectrum from each ring of the accretion disc and the total spectrum is a multicolour blackbody. The radial variation of the local emitted flux

(Shapiro & Teukolsky, 1984) of radiation in a Keplerian disc can be expressed as,

$$F(x) = 6.25 \times 10^{25} \left(\frac{M}{M_\odot}\right)^{-2} \left(\frac{\dot{M}}{10^{17}\,\mathrm{gm\,s^{-1}}}\right) \frac{\mathscr{I}}{x^3} \quad \mathrm{erg\,cm^{-2}\,s^{-1}}, \tag{1.7}$$

where $\mathscr{I} = 1 - \sqrt{\frac{3}{x}}$ and $\dot{M}$ represents the accretion rate in $\mathrm{gm\,s^{-1}}$. The associated radial distribution of the effective temperature ($T_{\rm eff}$) of the disc can be estimated as,

$$F(x) = \sigma T_{\rm eff}^4(x), \tag{1.8}$$

where σ is the Stefan-Boltzmann constant. The temperature of the accretion disc exceeds 10^6 K close to the compact object and the disc is luminous in soft X-ray (0.1 - 10 keV).

It is assumed that an optically thick disc emits locally like a blackbody where the intensity of radiation depends only on the local disc temperature. The blackbody spectrum at a frequency ν, is described by the Planck function,

$$B_\nu(T_{\rm eff}) = \frac{2h\nu^3/c^2}{\exp(h\nu/kT_{\rm eff}) - 1}, \tag{1.9}$$

where h is the Planck constant. In the low frequency regime ($h\nu << kT_{\rm eff}$) which is known as Rayleigh-Jeans limit, the intensity of radiation is given by

$$I_\nu^{RJ}(T_{\rm eff}) = \frac{2\nu^2}{c^2} kT_{\rm eff}. \tag{1.10}$$

Whereas in the high frequency regime ($h\nu >> kT_{\rm eff}$), the radiation intensity is expressed by the Wien law,

$$I_\nu^{W}(T_{\rm eff}) = \frac{2h\nu^3}{c^2} \exp\left(-h\nu/kT_{\rm eff}\right) \tag{1.11}$$

For a given temperature, the radiation spectrum has a maximum at $h\nu_{\rm max} = 2.82kT_{\rm eff}$. The temperature of the accreted matter increases as it moves closer to the compact object and the peak frequency of the blackbody radiation shifts linearly with the temperature. We have shown a representative radiation spectrum of Keplerian accretion disc around a $10\,\mathrm{M}_\odot$ BH with an accretion rate $0.1\,\dot{M}_{Edd}$ in Figure 1.3. The red line represents the contribution from the outer region of the disc and mostly dominated in the Rayleigh-Jeans part of the spectrum as the outer disc is cold. Whereas the inner region of the disc is relatively hot and behaves as Wien distribution (blue line) and the green line denotes the modified contribution of the middle region of the disc. The black line shows the overall spectrum of the accretion disc

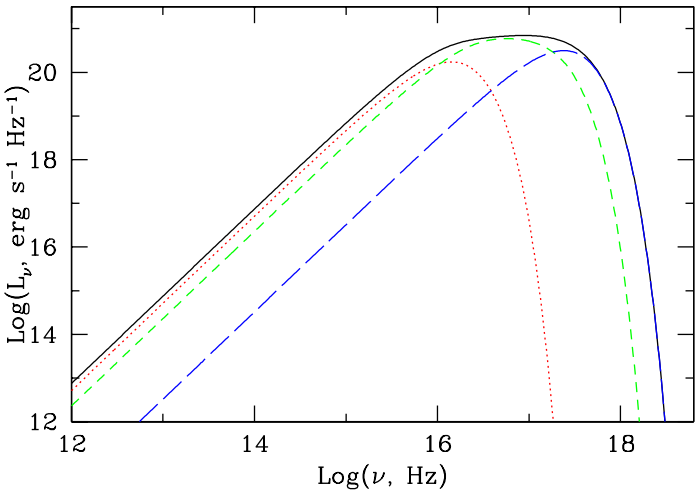

Figure 1.3: Blackbody radiation spectrum from the outer region (red), middle region (green) and inner region (blue) of the accretion disc are plotted. The black line represent the modified blackbody spectrum of the entire accretion disc.

with a modified blackbody ($I_\nu \propto \nu^{1/3}$) signature. This multi-colour blackbody spectrum is the hallmark of standard accretion disc model.

The differentially rotating matter in the accretion disc is having a very little radial infall velocity. Hence local friction between the rings of matter dissipates a significant amount of energy, making the accretion disc to be radiatively efficient. Hence, the disc is geometrically thin (disc vertical height, $H << x$) as the viscous heating is balanced by the radiative cooling locally. This disc model could successfully explain the soft X-ray bump in XRBs as well as the ultraviolet bump observed in several AGNs (Sun & Malkan, 1989). But the observed spectra of XRBs extend beyond 100 keV and similar observations for AGNs, quasars (Katz, 1976) indicate that the Keplerian disc model is unable to explain the observations in the broad energy range. On the theoretical ground, the assumption of Keplerian flow may not be always true. Also, the effect of the radial pressure gradient and advection in the flow were ignored in deriving the model solution analytically. Meanwhile, Eardley et al. (1975) showed a Keplerian disc may flare into a thick disc close to the central object. These observations and theoretical issues demand additional accretion disc models which are discussed in the subsequent sections.

1.3.3 Thick Accretion Disc

There is no single model that can be treated as a standard thick disc model. Rather a wide variety of models were proposed since the 1970s to explain the high energy part

of the observed radiation spectra. Works of Thorne & Price (1975); Lynden-Bell (1978); Stoeger (1978) indicated that in a hot disc the radiation pressure may cause instabilities and thicken ($H \approx x$) the accretion disc closer to the inner edge. At a high accretion rate ($\dot{M} >> \dot{M}_{Edd}$), the optical depth due to absorption (τ) in the accretion disc is also high. The mean travel time of photon in such a medium is proportional to τ^2 and the photon escape time exceeds the accretion time scale (Jaroszynski et al., 1980). As a result, a part of the dissipated energy produced in the disc is advected into the black hole horizon (not a hard surface). This reduces the radiative efficiency (η) of the accretion disc. The radial pressure gradient and heat flux are important in a thick disc and the flow deviates from Keplerian rotation. Stoeger (1980) showed that matter moves with supersonic speed below the marginally stable orbit and the Keplerian prescription of angular momentum is not be valid. Paczyński & Wiita (1980) assumed that a thick disc or sub-Keplerian disc can be generated from a Keplerian disc outside. Abramowicz et al. (1988) introduced a vertically average thick disc or the so called "slim disc" and global transonic solutions were found by Chen & Taam (1993).

On the other hand, if the accretion rate is very low ($\dot{M} << \dot{M}_{Edd}$), cooling processes are not significant due to very low electron density and the disc is radiatively inefficient. But the ion pressure is enough to puff up the disc (Rees et al., 1982) and the temperature of the accreted matter can reach up to $10^8 - 10^{11} K$ near to the compact object. The dissipated energy is therefore advected to the central compact object instead of being radiated away and this is known as advection dominated accretion flow (ADAF) (Narayan & Yi, 1994). ADAF model is applicable to faint objects (Done et al., 2007) due to very low radiative efficiency.

Most of these works on thick discs, the radial velocity of the flow were ignored. Meanwhile, Abramowicz & Zurek (1981) studied the transonic flow properties with sub-Keplerian angular momentum distribution. Whereas, Fukue (1987); Chakrabarti (1989) presented transonic shock solutions in a sub-Keplerian disc, keeping the advection term in the flow radial momentum conservation equation. Chakrabarti & Titarchuk (1995) considered both Keplerian as well as sub-Keplerian components and introduced a two-component accretion flow which could address both the low and high energy part of the observed spectra. In this thesis, the spectral modelling of observed data is performed using the two-component accretion flow model and we have presented an outline of the model and the radiation processes in Chapter 2.

1.4 Outflows/Jets

It is generally understood that the accretion and ejection (outflow/jet) processes are always associated. For example, a wide variety of systems such as young stellar objects, XRBs and AGNs which show strong outflows/jets, are always found to have an accretion disc. Though the basic mechanism of production of outflow/jet is still unclear but a hot accretion flow and/or presence of an open magnetic field in the disc are thought to be the possible ingredients for launching outflows/jets. In an advective accretion flow, a significant fraction of the available energy is converted into the internal energy of matter and only a small part of it is taken by the emitted radiation. Therefore, the energy density of matter is comparable with the gravitational potential energy density. A fraction of the accreting matter close to the central object can therefore escape due to the thermal and radiation pressure effect and produce a jet/outflow. The acceleration and collimation of outflows possibly need the presence of a magnetic field in the disc. Blandford & Payne (1982) suggested that the hot ionised material follow the open magnetic field lines anchored with the disc and the field lines get wound up by the rotation of the disc creating collimation.

Radio observations of black hole XRBs show the presence of steady compact as well as transient jets (Gallo, 2006; Corbel, 2011, and reference therein). The high brightness temperature, non-thermal spectra, and polarisation measurements reveal that the origin of radio emission is due to synchrotron emission from relativistic electrons in the jet. It is found that the radio and X-ray luminosity in BHXRBs are correlated (Xue & Cui, 2007; Corbel et al., 2013). Also, several studies show that the jet/outflow activity is related to the X-ray spectral states. The compact steady jets (Gallo et al., 2003; Fender et al., 2003) are always produced in the hard state (see §1.6) and jet activity is absent (Gallo et al., 2003; Fender et al., 2004, 1999) in the soft state (defined in §1.6). Whereas a transient relativistic jet is usually seen during the transition between the hard and the soft spectral state (Fender et al., 2006; Russell et al., 2013). The evidence of the wind outflow is found in the form of absorption lines (Ueda et al., 2004; Miller et al., 2006a; Ponti et al., 2014) seen along the line of sight to the central X-rays source. The disc wind can carry away large amounts of mass and energy from the accretion disc and possibly be the reason for the quenching of jet in the soft spectral state (Ponti et al., 2012). We attempt to establish this radio/X-ray correlation by studying the evolution of the radio flux with the accretion dynamics for one of the outbursting sources considered in this thesis.

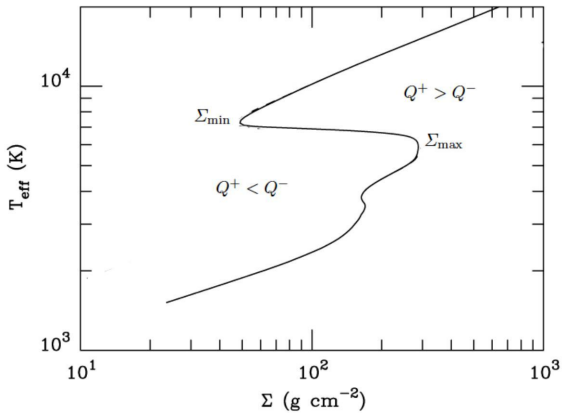

Figure 1.4: The thermal equilibria of a ring of matter in an accretion disc around a white dwarf are represented by the solid line. The minimum surface density ($\Sigma_{\rm min}$) for a hot stable equilibrium and the maximum surface density ($\Sigma_{\rm max}$) of a stable cold equilibrium are marked in the figure (credit : Lasota (2016)).

1.5 Outbursts in XRBs and the Disc Instability Model

XRBs, in particular the low mass XRBs, show occasional outbursts where the X-ray brightness of the systems increases by several order of magnitude. The system remains active for several days to several months before it returns back to the quiescent phase. The outburst mechanism in XRBs is often described by disc instability model (Osaki, 1974; Meyer & Meyer-Hofmeister, 1981; Cannizzo, 1993). Even though this model can be invoked to understand the outburst mechanism in XRBs, it was originally proposed to explain the dwarf novae outbursts (Osaki, 1974). First, we outline the disc instability model (DIM) and then discuss an extension to understand the outbursts in XRBs.

In a dwarf nova system, the accretion disc is formed around the central white dwarf due to the transfer of matter from a low mass Roche lobe filling companion star. The disc is assumed to be geometrically thin and angular momentum distribution is always Keplerian. The accretion disc is mainly made of hydrogen, and the physical properties of hydrogen may trigger an instability in the accretion disc. This is the primary assumption of DIM. The local thermal equilibrium characteristic of an accretion disc is often represented by the S-shaped curve shown in Fig 1.4. The figure represents the variation of effective disc temperature ($T_{\rm eff}$) with the surface density (Σ) at a particular radius of the accretion disc. The solid line in Figure 1.4 represents the thermal equilibrium i.e., the cooling rate per unit area (Q^-) is balanced by the heating (Q^+). On the left of the S-curve cooling dominates over heating ($Q^+ < Q^-$) and on the right heating is more than cooling ($Q^+ > Q^-$). The S-curve represents a 'limit cycle' oscillation of the accretion disc between a hot (outburst)

and a cold (quiescence) state. A stable equilibrium point is present either on the lower cold or upper hot branch of S-curve and the middle part of the S-curve represents unstable equilibrium. That means the surface density in the cold branch must be lower than the maximum value ($\Sigma_{\rm max}$) on the cold branch. Whereas the surface density in the hot branch must be larger than the minimum value on this branch. Both these critical surface densities can be expressed (Lasota, 2016) as,

$$\Sigma_{\rm min}(R) = 399\,\alpha_{\rm vis}^{-0.80} R_{10}^{1.11}\, m_{bh}^{-0.37} \quad {\rm gm\,cm^{-2}}$$

and

$$\Sigma_{\rm max}(R) = 746\,\alpha_{\rm vis}^{-0.83} R_{10}^{1.18}\, m_{bh}^{-0.40} \quad {\rm gm\,cm^{-2}},$$

where $\alpha_{\rm vis}$ is the viscosity parameter, m_{bh} is the mass of the accreting object in units of $M_\odot$ and R_{10} denote the radial distance from the central source in unit of 10^{10} cm.

During quiescence, the accretion of matter from the companion takes place at a slow, steady rate and the accreted matter accumulates at the pileup radius near the outer boundary of the disc. This produces a truncated accretion disc which remains in the cold state. A steady accretion of matter gradually increases the surface density and temperature of the disc and it continues until the disc material becomes hot (around 6000 K) enough to trigger hydrogen ionisation which increases the opacity and viscosity of the disc. Also, the surface density reaches the upper critical value ($\Sigma_{\rm max}$) leading to a thermo-viscous instability. Therefore, a hot wave propagates throughout the disc and the thermal state of the disc changes suddenly to a hot and high viscous state (upper branch in the S-curve). In the hot state, the higher value of viscosity leads to a greater rate of infall of matter and the accretion disc moves toward the white dwarf. As a result, the disc becomes luminous triggering an outburst in dwarf nova system. But the rate of accretion in the hot phase is much higher compared with the same transfer from the companion star. Therefore, the total mass of the accretion disc, as well as the surface density of matter, decreases gradually. Finally, as the surface density drops below the lower critical value ($\Sigma_{\rm min}$), hydrogen in the disc begins to recombine leading to cool wave propagation through the disc and the system returns back to the quiescent (neutral) state. This cyclic behaviour is characterized by an alternate period of outburst and quiescence observed in dwarf novae. After each outburst, the disc has to fill up with fresh matter before erupting once more.

Even though the DIM could explain the outbursts in dwarf novae fairly well, but this model can not be used directly to the outbursts in LMXBs because of the large difference in outburst duration in two systems. The dwarf nova outburst lasts for a few days and recurs

in a few weeks whereas the same for LMXB is few months and years respectively. A typical outburst luminosity in dwarf novae is $\sim 10^{32}\mathrm{erg\,s^{-1}}$, whereas the same for LMXBs becomes much more luminous ($10^{38} - 10^{39}\mathrm{erg\,s^{-1}}$). Also, the disc becomes luminous in optical - UV bands for dwarf novae but LMXBs are bright in X-ray. The outbursts in LMXBs may also be triggered by thermo-viscous disc instability and the disc reaches into a hot state. Therefore, the inner region of the accretion disc becomes X-ray luminous and these high energy photons may irradiate the outer part of the accretion disc. If the irradiation is strong enough to prevent hydrogen recombination then the disc remains in the hot branch and the outburst phase continue for the much longer time duration. van Paradijs (1996) introduced the irradiated DIM to understand the outburst in XRBs. In the hot phase, the accretion rate towards the central object is much higher than the supply of matter from the companion. Therefore, the available amount of matter in the disc gradually decreases along with the progress of the outburst and it reduces the central X-ray activity. Eventually, the irradiation by the central source becomes weak enough that the outer disc temperature goes below the hydrogen ionisation temperature and the disc makes a transition to the cold branch.

On the theoretical ground outburst may proceed `inside-out` or `outside-in` and different outburst profiles are expected depending on the nature of triggering. For an inside-out type, the outburst triggers at the inner region of the disc and then propagates outwards whereas outside-in outburst triggering occurs at the outer part of the disc and propagates inward. Outbursts are naturally expected to be outside-in type as the surface density at the outer edge may cross the critical value due to accumulation of mass from the companion. Of course, this requires relatively high mass transfer rate from the companion. Whereas, if the mass transfer rate from the secondary is low, an occasional triggering of instability may happen at the inner region of the accretion disc. The light curves of inside-out outbursts are more symmetrical in nature whereas the same for outside-in outbursts result in asymmetrical light curves, typically fast rise exponential decay. Although, the exponential decay profile modifies into a linear decay due to the irradiation effect.

Observationally, light curves of XRB outbursts show different morphological types which vary between sources and also between an individual outburst of the same source. In most of the cases, the profiles appear to be fast rise exponential decay (FRED), fast rise slow decay (FRSD), slow rise slow decay (SRSD). Nevertheless, some of them are quasi-persistent and irregular in nature with multiple peaks and complex variability. The FRED profile is considered to be the typical XRB light curve where the peak is followed by an exponential decay on a timescale of a month before the system returns to the very

low luminous quiescent state.

Generally, it is understood that the outburst profile is shaped by the nature of the angular momentum and mass transport in the accretion disc. The DIM can explain the observed properties of outbursts such as rise, decay, and recurrence time of the outbursts. The outburst rise time is generally decided by the viscous timescale in which matter diffuses through the disk over a distance x, under the effect of viscous torques and it can be expressed as (Frank et al., 1992),

$$t_{\rm vis} = \frac{x^2}{\alpha_{\rm vis} c_s H}.$$

An accretion disc having higher viscosity accretes at a faster rate, resulting in faster decay and shorter outburst duration. The local disc structure changes in dynamical timescale ($t_{\rm dyn} \sim x^{3/2}$). As a result, the outburst profiles are not expected to be smooth and may carry the signature of local dynamics. During the course of evolution, an accretion disc always maintains the thermal equilibrium ($Q^+ = Q^-$) by connecting the viscous processes with the dynamics in the thermal timescale, $t_{\rm th} \sim t_{\rm dyn}/\alpha$. These three timescales are enough to define the evolution of accretion process and generally they are related as $t_{\rm dyn} << t_{\rm th} << t_{\rm vis}$ for typical accretion parameters.

1.6 X-ray Spectral States of Outbursting BHXRBs

The X-ray emission from accreting black holes broadly consists of two components which are thought to be originated from two different regions of the accretion flow. The X-ray spectral states (Homan & Belloni, 2005; Remillard & McClintock, 2006) are defined based on the relative contributions of the two spectral components and the time variabilities. In the low/hard state (LHS), the source brightness is low and the radiation spectrum has a photon index in the range of $1.5 - 1.7$. The photon index is usually defined in the energy range above 10 keV which is mostly dominated by the high energy photons. The X-ray timing variability is maximum (Homan, 2001) in this state. The power density spectrum (PDS) is dominated by band-limited noise (in the frequency range $0.01 - 0.1$ Hz) with 20-50% rms and type-C quasi periodic oscillation (QPO) is usually observed. The centroid frequency (ν_0) of these oscillations remain in the range $0.01 - 30$ Hz with a quality factor ($\nu_0/\Delta\nu$, where $\Delta\nu$ is the full width at half maximum), $Q \geqslant 10$. Whereas in high/soft state (HSS) the source is bright and the radiation spectrum shows a steep photon index ~ 3. Therefore, the radiation spectrum shows a dominant contribution in the low-energy

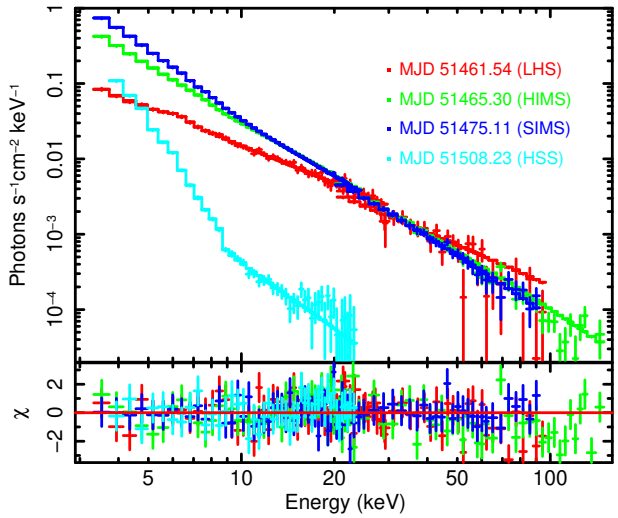

Figure 1.5: Broadband RXTE/PCA and RXTE/HEXTE energy spectra of XTE J1859+226 in different states LHS, HIMS, SIMS and HSS. Credit : Nandi et al. (2018).

X-ray band. The PDS in this state has a powerlaw signature with less than 2-3% rms, indicating the least timing variability. Also, it is quite often found that the spectral state is intermediate (hard intermediate state: HIMS and soft intermediate state: SIMS) where the soft photon contribution becomes significant and the photon index lies within $\sim 1.7 - 2.5$. The rms noise in the PDS is weaker (typically 5-20% rms). Generaly, type-C QPOs are observed in the HIMS whereas SIMS shows occasional appearance of type-A and type-B QPOs (Belloni et al., 2005). The type-B QPOs have $\nu_0 \sim 0.8 - 6.4$ Hz with $Q > 6$ whereas type-A QPOs are broad ($Q \sim 1 - 3$) and centroid frequency lies in the range $6.5 - 8$ Hz. Figure 1.5 represents typical energy spectra of BHXRBs in different spectral states.

During outbursts, transient black hole XRBs show spectral state transitions in the hardness intensity diagram (HID) (Homan & Belloni, 2005; McClintock & Remillard, 2006; Remillard & McClintock, 2006; Belloni, 2010; Nandi et al., 2012; Radhika & Nandi, 2014). At the beginning of the rising phase, the system stays in the low-hard state (LHS) with a hard spectrum. After this, the system makes a transition to intermediate states and finally, it reaches the high-soft state (HSS). The duration of state transition via intermediate state is usually very short, ranging from hours to days, and hence the accretion physics related to these states is difficult to study. During the decay phase of the outburst, the source returns back to the LHS through SIMS and HIMS. This hysteresis nature of HID was first reported by Miyamoto et al. (1995) and most of the outbursting black hole XRBs show this behaviour in HID. An outburst is classified as complete if the source makes a transition to all spectral states, else it is categorised as a failed outburst.

1.7 Motivation and Source Selection

Several galactic BHXRBs show transient X-ray brightening or outbursts. Each outburst is different from the other in terms of observable features like luminosity, outburst duration, rise and decay time as well as recurrence duration. Hence, transient XRBs are excellent laboratories to study the underlying physics responsible for similarities and differences in their observable properties. We have selected two galactic transients BHXRBs, GX 339-4 and H 1743-322, which undergo frequent outbursts. The extensive observational coverage of outbursts of these two sources by Rossi X-ray timing explorer (RXTE) provides a wonderful opportunity to study the outbursts properties. GX 339-4 has undergone four complete outbursts, whereas H 1743-322 has shown eight outbursts in the RXTE era. Outbursts of GX 339-4 have longer duration with a recurrence period of a couple of years, whereas H 1743-322 has outburst duration order of a couple of months and 6-8 months of recurrence period. The source H 1743-322 has a much shorter rise time compared with GX 339-4. Also, H 1743-322 shows both shorter and longer duration outbursts. The complexity and wide variety of the nature of these outbursts motivate us to study the physics behind the similarities/differences between the outbursts.

It is assumed that a persistent accretion activity is associated with the irradiation phase of the outburst. Therefore, the irradiation phase of a transient source is expected to exhibit the similar accretion physics that of the persistent source. We wish to compare the spectral and accretion evolution of persistent sources with the irradiated phase of the outbursting sources. Since both GX 339-4 and H 1743-322 are low-mass BHXRBs, we select two low-mass persistent BHXRBs (GRS 1758-258 and 1E 1740.7-2942) for the proposed comparative study. In this regards, Indian astronomy satellite, AstroSat, has observed these two persistent sources based on our announcement of opportunity (AO) proposal and we use broadband AstroSat observations of GRS 1758-258 and 1E 1740.7-2942 to complement our study.

Chapter 2

Two Component Accretion Flow and Radiation Processes

The general characteristics of the radiation spectrum from BHXRBs consists of a soft thermal component and a high energy non-thermal component. It is generally accepted that the soft thermal radiation originates from the standard Keplerian disc (Shakura & Sunyaev, 1973; Novikov & Thorne, 1973) and has a signature of multi-colour blackbody radiation. The non-thermal part of the radiation spectrum has a powerlaw characteristic and it is assumed to be originated from the Compton cloud/corona/hot electron cloud (Chakrabarti & Titarchuk, 1995; Narayan & Yi, 1995) by the inverse Comptonisation (Sunyaev & Titarchuk, 1980, 1985; Haardt & Maraschi, 1993; Titarchuk, 1994; Zdziarski et al., 1998) of soft photons from Keplerian disc. Alternately, Markoff et al. (2005) suggested non-thermal synchrotron photons as well as thermal and non-thermal synchrotron self-Comptonization in the jet as the source of hard photons.

These phenomenological models are used to fit the X-ray spectra and extract the spectral parameters. But they are independent and do not consistently connect the spectral parameters with the physical processes involved. For example, phenomenological models do not justify that inverse Comptonisation of soft photons with a given temperature could able to produce the observed photon index and the number of high energy photons. Therefore, it is important to search for a physical model which takes care of the flow hydrodynamics along with the radiative processes and the radiation properties are solely determined by the flow dynamics. The two-component accretion flow model is developed using the solutions of radiation-hydrodynamic equations connecting the physical parameters of the accretion flow.

In this chapter, we provide a brief description of the two-component accretion flow including the radiation properties of the flow. Also, we describe the radiation processes

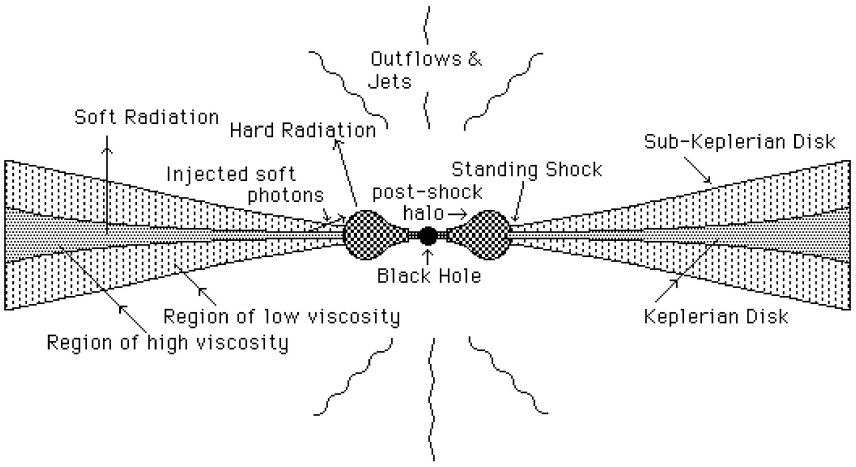

Figure 2.1: Schematic diagram of the two-component accretion process around a black hole. An optically thick, Keplerian disc in the equatorial plane produces soft photons and is surrounded by an optically thin sub-Keplerian halo. The Keplerian disk terminates at the shock/pileup region. The soft photons from the Keplerian disc get Comptonised in the post-shock region and produce hard photons. Jets/Outflows are also originated from the post-shock region (credit : Chakrabarti & Titarchuk (1995)).

which are not included in the two-component accretion flow model but are used as additional components in the spectral modelling of observed data.

2.1 Two Component Accretion Flow

The two-component accretion flow (Chakrabarti & Titarchuk, 1995) assumes a Keplerian accretion flow on the equatorial plane of the system and a sub-Keplerian flow sandwiches the Keplerian flow above and below. The co-existence of both the components of accretion flow have been studied analytically as well as through numerical simulations. Chakrabarti (1990, 1996) found that the flow becomes Keplerian for the viscosity parameter above a critical value whereas the flow remains sub-Keplerian below the critical value. Starting with a sub-Keplerian flow, Giri et al. (2015) showed using numerical simulation that a Keplerian disc can be formed at the equatorial plane by redistribution of angular momentum. Accretion happens in a Keplerian disc due to the transfer of angular momentum outward in viscous time scale. Therefore, the radial velocity of the flow in a Keplerian disc is very low and it always remains subsonic (Mach number, $\mathcal{M} = \frac{v}{c_s} < 1$, where v is the radial velocity of the flow and c_s is the sound speed). Whereas the inner boundary condition of BH accretion demands that the radial velocity of the flow has to reach the speed of light on the horizon and hence a Keplerian flow can never reach to the BH horizon. On the other hand, a

sub-Keplerian (angular momentum is less than that of Keplerian flow) flow responds close to the free-fall time scale though the infall time scale may modify significantly due to presence of strong cooling. At a far distance, the radial velocity of sub-Keplerian flow is nearly zero (subsonic flow) and the flow becomes supersonic ($\mathcal{M} > 1$) close to the BH. That means the accretion flow is transonic in nature. Also close to a black hole, the specific angular momentum of the flow is almost constant due to a shorter infall time scale. Therefore, the centrifugal force ($\propto 1/x^3$, where x is radial distance) increases faster than gravitational force ($\propto 1/x^2$) and the accreted matter slows down due to pileup. In an extreme scenario, the supersonic flow may pass through a shock transition and the flow kinetic energy is converted into thermal energy in the post-shock region (PSR). Finally, the slowed down matter pass through the horizon due to the extreme non-linear nature of the gravity very close to BH. The high energy electrons in the PSR act as Compton cloud/corona/hot electron cloud which inverse Comptonise a fraction of the locally produced soft photons as well as soft photons from the Keplerian disc. We provide a brief description of the hydrodynamics of the two-component flow as follows.

2.1.1 Hydrodynamic Equations

Let us consider an axisymmetric accretion of sub-Keplerian matter at the equatorial plane onto a Schwarzschild black hole. We describe the spacetime geometry around the black hole by a pseudo-Newtonian potential $\phi(x) = -\frac{1}{2(x-1)}$ (Paczyński & Wiita, 1980), where x is the radial distance of the flow in units of Schwarzschild radius. We express black hole mass in units of $M_\odot$. The radial momentum equation (Chakrabarti & Titarchuk, 1995) is given by

$$v\frac{dv}{dx} + \frac{1}{\rho}\frac{dP}{dx} - \frac{\lambda^2}{x^3} + \frac{1}{2(x-1)^2} = 0, \tag{2.1}$$

where P and ρ are vertically integrated pressure and mass density, respectively, λ is the specific angular momentum, v is the radial infall velocity in units of c.

This is supported by the mass conservation equation

$$\dot{M} = \Omega\rho x H v, \tag{2.2}$$

where $\dot{M}$ is called the accretion rate, Ω depends on the geometry of the disc and $H(x)$ is the vertical thickness of the disc at a radial distance x.

Integration of equation 2.1 provides specific energy of the flow,

$$\mathcal{E} = \frac{v^2}{2} + \frac{c_s^2}{(\gamma_a - 1)} + \frac{\lambda^2}{2x^2} - \frac{1}{2(x-1)}, \tag{2.3}$$

In presence of heating/cooling processes in the disc, the entropy generation equation (Chakrabarti & Titarchuk, 1995) is given by,

$$\frac{\partial}{\partial x}\left(\mathcal{E} + \frac{P}{\rho}\right) + (Q^+ - Q^-) = 0, \tag{2.4}$$

where Q^+ represents the heating contribution and Q^- corresponds to the cooling process. The PSR becomes hot and dense due to the conversion of kinetic energy of the flow into thermal energy as well as geometric compression. Also, the radiative efficiency of electrons is much higher than protons due to the difference in their rest mass. The electrons in the PSR loss energy due to bremsstrahlung, synchrotron and Comptonisation processes. Hence, the flow behaviour can be single temperature or two temperature depending on the transfer of energy from protons to electrons via Coulomb coupling. In presence of efficient radiative processes, the radial variation of temperature (T_p and T_e) can be derived from Equation (2.4) and are expressed separately for protons and electrons (Mandal & Chakrabarti, 2005) as,

$$\frac{dT_p}{dx} + \frac{T_p(3x-4)}{3x(x-1)} + \frac{2}{3}\frac{\Omega m_p}{k\dot{M}}x^2(Q_p^+ - Q_p^-) = 0 \tag{2.5}$$

$$\frac{dT_e}{dx} + \frac{3}{2}(\gamma_a - 1)\frac{T_e(3x-4)}{3x(x-1)} + (\gamma_a - 1)\frac{\Omega m_p}{k\dot{M}}x^2(Q_e^+ - Q_e^-) = 0 \tag{2.6}$$

Here, subscript "p" and "e" represents proton and electron respectively. The mass of proton is represented by m_p. Protons are assumed to be non-relativistic and γ_a varies between 5/3 - 4/3 depending on the relativistic nature of the electrons.

In presence of efficient radiative processes, electrons extract energy from protons via Coulomb coupling. Therefore, it acts as a heating process for electrons (but a cooling process for protons) and the energy exchange rate is expressed (Spitzer, 1965; Colpi et al., 1984) as,

$$Q_e^+ = 1.6 \times 10^{-13}\frac{k\sqrt{m_e}ln\Lambda_0}{m_p}n^2\frac{(T_p - T_e)}{T_e^{3/2}} \quad \mathrm{erg\,cm^{-3}\,s^{-1}}, \tag{2.7}$$

where Λ_0 is the Coulomb logarithm, n is number density and m_e is the rest masses of electron. This study did not consider any heating process for protons ($Q_p^+ = 0$). Elec-

trons undergo cooling due to bremsstrahlung (Q_b), cyclo-synchrotron (Q_{cs}) and inverse-Comptonisation (Q_{mc}) of the soft photons. The net cooling of the electron is given by

$$Q_e^- = Q_b + Q_{cs} + Q_{mc} \tag{2.8}$$

The Two-component model used for spectral modelling in this thesis did not include synchrotron cooling. Hence, Q_{mc} corresponds to the inverse-Comptonisation of soft photons from the Keplerian disc only. The net cooling of protons are due to Coulomb interaction and inverse-bremsstrahlung (Q_{ib}):

$$Q_p^- = Q_e^+ + Q_{ib} \tag{2.9}$$

The expression of different cooling terms can be found in (Mandal & Chakrabarti, 2005, and reference therein). Also, a brief discussion on the radiative processes are given in the §2.2. Equation (2.1), Equation (2.2), Equation (2.5) and Equation (2.6) are solved simultaneously including the radiative terms (Equation 2.7 - Equation 2.9) to calculate the radial variation of the flow variables (n, v, T_e, T_p). Finally, these flow variables are used to calculate the emitted spectrum corresponds to different radiation processes (§2.2).

The two-component accretion model is implemented in `Xspec`[1] as a table model (Iyer et al., 2015) using the HEASoft routines. The table model is created by generating huge number of model spectra by varying the model parameters and saving them in an array. The model input parameters are (i) the mass of the black hole m_{bh} (in units of $M_\odot$); (ii) the Keplerian accretion rate $\dot{m}_d$ (in units of $\dot{M}_{Edd} = 1.4 \times 10^{18}(M/M_\odot$ gm/sec with 10% accretion efficiency); (iii) the sub-Keplerian accretion rate $\dot{m}_h$ (in units of $\dot{M}_{Edd}$); (iv) the size of the centrifugal barrier or PSR, x_s, (in units of r_g). Also, (v) the overall normalisation of the model, $\cos i/D^2$, where D is the distance to the source in 10 kpc and i is the inclination angle of the system, is an additional free parameter. The model parameters are estimated by fitting the observed data with the table model in `Xspec`.

The `Xspec` implemented two-component accretion flow table model can explain the general properties of the BHXRBs spectra quite well. Although, we explore certain limitations of the model as well. In the two-component model, the contribution from the jet/outflow is not included and therefore, it may affect the overall normalization, particularly in LHS as well as in the case of sporadic relativistic ejections. The radiation processes related to bound-free absorption (§2.3.2), fluorescence emission (§2.3.3) are not self-consistently included in the current model. That is why, additional model components

[1] https://heasarc.gsfc.nasa.gov/xanadu/xspec/

like `smedge`, `edge` and `gauss` are occasionally required to fit the data. In the table model, the multi-colour blackbody spectrum is calculated from the local effective temperature ($T_{\rm eff}$) of the Keplerian accretion disc. But at the high accretion rate ($\dot{m}_d$), electron scattering may be important, particularly in the inner region of the disc, and it may harden the spectrum. Therefore, the spectrum calculations should be modified by colour temperature $T_c = \xi\, T_{\rm eff}$ (Shimura & Takahara, 1995), where ξ is the hardening factor. We have incorporated the colour temperature in the two-component model and have done a custom implementation of the source code under `Xspec` environment. We have applied this modification to fit a few selected data sets of the very luminous 2003 outburst of H 1743-322.

2.2 Radiation Processes

The accretion disc around a black hole is generally very hot and dense due to geometrical compression and release of gravitational potential energy. The hot accreting material is mostly ionized and emits in X-ray due to different radiation processes which have been included in the hydrodynamics (§2.1). We have already discussed the multi-colour blackbody nature of the Keplerian disc in §1.3.2. Here, we discuss the radiation processes relevant to the sub-Keplerian flow only.

2.2.1 Thermal Bremsstrahlung

Bremsstrahlung radiation is produced when an electron passes near an ion, the electron gets accelerated due to Coulomb interaction, and it emits electromagnetic radiation. This is also referred as free-free emission since the electron is unbound to ion before and after the interaction. The collision of like particles (electron-electron, proton-proton) can not produce bremsstrahlung radiation in the dipole approximation because dipole moment $\sum_i e_i r_i$ is proportional to the center of mass $\sum_i m_i r_i$ which is a constant of the motion. In electron-ion bremsstrahlung, the primary radiator is an electron, since the relative acceleration is inversely proportional to the mass. The free-free emissivity from a medium with ion number density n_i, electron number density n_e and for a fixed electron speed v is given as (Rybicki & Lightman, 1979),

$$j^b_\nu(v) = \frac{32\pi^2 e^6}{3\sqrt{3}c^3 m_e^2 v} n_e n_i Z^2 g_{\rm ff}(v,\nu), \tag{2.10}$$

where ν is the frequency of emitted radiation, Z is the atomic number of ion, e is charge of electron, m_e is mass of electron and $g_{\rm ff}$ is the Gaunt factor which depends on the maximum and minimum value of the impact parameters. In general the accreting plasma is in thermal equilibrium and follows Maxwell-Boltzmann distribution with temperature T_e. The total emission can be estimated by averaging $j^b_\nu(v)$ over thermal distribution as,

$$j^b_\nu(T) = \frac{\int_{v_{\rm min}}^{\infty} j^b_\nu(v)\, v^2 e^{-\frac{m_e v^2}{2kT_e}}\, dv}{\int_0^{\infty} v^2 e^{-\frac{m_e v^2}{2kT_e}}\, dv}, \tag{2.11}$$

where $v_{\rm min} = (2h\nu/m_e)^{1/2}$. Radiation emissivity from a non-relativistic optically thin medium (Rybicki & Lightman, 1979) is,

$$j^b_\nu = \frac{2^5\pi e^6}{3m_e c^3}\sqrt{\frac{2\pi}{3km_e}} Z^2 n_e n_i T_e^{-\frac{1}{2}} e^{-h\nu/kT_e} \bar{g}_{\rm ff}, \tag{2.12}$$

where $\bar{g}_{\rm ff}$ is the velocity averaged Gaunt factor. The integration of Equation (2.12) over frequency provides the total power per unit volume emitted due to electron-proton ($Z = 1$) thermal bremsstrahlung as

$$Q_b = \frac{2^5\pi e^6}{3hm_e c^3}\sqrt{\frac{2\pi kT_e}{3m_e}} Z^2 n^2 \bar{g}_B, \tag{2.13}$$

where $n_e = n_i = n$ and $\bar{g}_B$ is the frequency average of the velocity averaged Gaunt factor. In thermal plasma like electrons, protons also emit radiation (inverse bremsstrahlung) due to Coulomb interaction with electrons. Inverse bremsstrahlung is less efficient since protons are more massive compared to electrons. The temperature of electrons and protons in plasma can be different depending on the radiative efficiency. In a two-temperature plasma, the expression for inverse bremsstrahlung emission can be expressed as,

$$Q_{ib} = Q_b\sqrt{\frac{m_e T_p}{m_p T_e}}. \tag{2.14}$$

2.2.2 Compton Scattering

The non-thermal nature of the high energy radiation spectra of BHXRBs is assumed to be originated due to inverse-Compton scattering. In Compton scattering process a photon interacts with a free electron and gets scattered with an exchange of energy. High energy photons lose its energy to electrons in this process. Whereas if the electron has more

kinetic energy, the energy transfer results from electron to photon and the process is called inverse Comptonisation. In the non-relativistic range ($kT_e << m_e c^2$), the fractional energy exchange per scattering in a thermal plasma is given by (Rybicki & Lightman, 1979),

$$\frac{\Delta\nu}{\nu} = \frac{4kT_e - h\nu}{m_e c^2}. \tag{2.15}$$

Photons gain energy from thermal electrons if $h\nu << kT_e$ whereas photons lose energy in the reverse scenario. The significance of Compton scattering is determined by the Compton y parameter which is defined as a product of average fractional energy change per scattering and the mean number of scattering. In the case of non-relativistic thermal distribution of electrons the Compton y parameter is given as (Rybicki & Lightman, 1979),

$$y_{NR} = \frac{4kT_e}{m_e c^2} \max(\tau, \tau^2). \tag{2.16}$$

Whereas the same for relativistic thermal electrons,

$$y_R = 16\left(\frac{kT_e}{m_e c^2}\right)^2 \max(\tau, \tau^2). \tag{2.17}$$

Here τ is the electron scattering optical depth of the scattering medium and is defined as,

$$\tau = \int \sigma_T \, n_e dx. \tag{2.18}$$

Here, the integration is performed over the dimension of the scattering medium. In an optically thin medium, τ is the mean number of scattering and as optical depth increases the mean number of scattering becomes τ^2. For $y \geq 1$, Compton scattering is important and photon energy, as well as the spectrum, will be altered significantly. In an optically thin medium, the inverse Comptonised photon spectrum follows a powerlaw distribution due to repeated scattering with electrons. It can be seen as follows: Consider an initial photon distribution of mean photon energy E_0 and intensity $I(E_0)$. Let A be the mean amplification factor of photon energy per scattering. After l number of scattering, the photon becomes $E_l \sim E_0 A^l$. If the medium is of small scattering optical depth, the probability of a photon undergoing l scattering before escaping the medium is $p_l(\tau) \sim \tau^l$. The intensity of emergent radiation at energy E_l is proportional to $p_l(\tau)$ and thus the emitted intensity is,

$$I(E_l) \sim I(E_0)\tau^l \sim I(E_0)\left(\frac{E_l}{E_0}\right)^{-\alpha} \tag{2.19}$$

where the energy spectral index $\alpha = -\frac{ln\,\tau}{ln\,A}$, which depends on the density as well as temperature of the medium. The probability of repeated scattering decreases whereas the corresponding gain in energy increases with the number of scattering, producing a powerlaw distribution for the inverse Comptonise spectrum.

In the two-component flow, the soft photons generated from the Keplerian disc are intercepted by the hot PSR where they get inverse Comptonised and produce a powerlaw spectrum (Equation 2.19). The spectral index (α) is a function of the average electron temperature ($T_{\rm av}$) and the electron scattering optical depth of PSR which is calculated by integrating Equation (2.18) between x_{in} (inner edge of the disc) and size of PSR (x_s). The energy density of intercept soft photons (u_{bb}) at PSR is calculated from each annulus of the Keplerian disc and it depends on the geometry of the PSR. Then u_{bb} is modified by an enhancement factor A_{comp} (Chakrabarti & Titarchuk, 1995) due to inverse Comptonization at PSR. Hence, the total Compton cooling can be written as,

$$Q_{mc} = u_{bb}\, A_{comp}. \tag{2.20}$$

Here, A_{comp} is calculated from the overall effective temperature (T_r) of the Keplerian disc, average electron temperature and spectral index. The inverse Compton radiation spectrum has a Rayleigh-Jeans characteristic in the low energy ($h\nu < 2.8kT_r$) and it shows a powerlaw nature beyond this whereas at very high energy ($h\nu \sim 3kT_{\rm av}$) it decays exponentially due to the recoil effect.

2.3 Additional Radiation Processes

2.3.1 Synchrotron Radiation

X-ray binaries show jet/outflow activities, and the radiations coming out of the jet are mainly produced by synchrotron. The synchrotron radiation is particularly important due to the motion of relativistic non-thermal particles in presence of a magnetic field. The `Xspec` implemented two-component table model did not include synchrotron radiation. We have considered this as an additional component required to model the X-ray contribution from the jet/outflow. For the sake of completeness, we provide below a brief description of the synchrotron emission due to the powerlaw distribution of electrons.

Charged particles in the presence of a magnetic field get accelerated and emit radiation. The characteristics of emitted radiation depend upon the velocity of charged particles and

the strength of the magnetic field. For charged particles having non-relativistic speed, the emitted radiation is called cyclotron radiation with the characteristic frequency of emission, $\nu_B = eB/2\pi mc$. Here e is the charge of the particle, B is the magnetic field, and m is the mass of the charged particle. In the relativistic scenario, the radiation is called synchrotron radiation and the power per unit frequency emitted by a charge particle is (Rybicki & Lightman, 1979),

$$\mathcal{P}_\nu = \frac{\sqrt{3}}{4\pi^2}\frac{e^3 B\,\sin\theta_0}{mc^2}\,\mathcal{F}\Big(\frac{\nu}{\nu_c}\Big), \tag{2.21}$$

where $\mathcal{F}$ is a dimensionless function, θ_0 is the pitch angle, critical emission frequency $\nu_c = 3\gamma^2\,\frac{eB\sin\theta_0}{4\pi mc}$ and γ is the Lorentz factor of the particle. We can calculate the radiation spectrum for a powerlaw distribution of particle energies. The number density of particles with energies between γ and $\gamma + d\gamma$ can be expressed as,

$$n(\gamma)d\gamma = C\gamma^{-p}d\gamma, \qquad\qquad \gamma_1 < \gamma < \gamma_2 \tag{2.22}$$

where p is the slope of the particle distribution, γ_1 and γ_2 are minimum and maximum Lorentz factor respectively. The total emissivity for the given distribution of particles can be found by the integrating Equation (2.21) over the particle energy distribution and can be written as,

$$j^s_\nu = C\int_{\gamma_1}^{\gamma_2}\mathcal{P}_\nu\gamma^{-p}d\gamma \propto \int_{\gamma_1}^{\gamma_2}\mathcal{F}\Big(\frac{\nu}{\nu_c}\Big)\,\gamma^{-p}d\gamma \tag{2.23}$$

Substituting $\chi = \nu/\nu_c$ and the above integral becomes,

$$j^s_\nu \propto \nu^{-(p-1)/2}\int_{\chi_1}^{\chi_2}\mathcal{F}(\chi)\,\chi^{(p-3)/2}\,d\chi. \tag{2.24}$$

For a wide range of energy we can approximate $\chi_1 \approx 0$, $\chi_2 \approx \infty$ and the integral becomes approximately constant. Therefore, the synchrotron emissivity (Rybicki & Lightman, 1979) for a powerlaw distribution of electrons is given by,

$$j^s_\nu = \frac{e^2 C}{2\sqrt{3}\pi c(p+1)}\,\Gamma\Big(\frac{p}{4}+\frac{19}{12}\Big)\Gamma\Big(\frac{p}{4}-\frac{1}{12}\Big)\left(\frac{3eB\sin\theta_0}{mc}\right)^{(p+1)/2}\nu^{-\alpha}, \tag{2.25}$$

where the spectral index $\alpha = \frac{p-1}{2}$. The synchrotron spectrum due to a powerlaw distribution of particles becomes a powerlaw and spectral index depends on p only.

2.3.2 Photoelectric Absorption

When X-ray photons interact with the material in the interstellar medium, the electron in the material makes a transition to different energy levels by absorbing X-ray photon. The radiation spectra of cosmic sources in the 0.1-10 keV are mostly affected by interstellar photoelectric absorption. The absorption processes are classified based on the final state of electron transition.

- Bound - bound transition: The electron makes a transition from one bound energy level to a higher bound energy level by absorbing an X-ray photon whose energy is equal to the difference in energy between the two energy levels. This transition results in an absorption line.

- Bound - free transition: Here, the electron makes a transition from a bound energy level to a continuum by absorbing photon energy equal or greater than the photoionisation energy. This transition results in an absorption edge.

In many BHXRBs, the residual of the continuum fitting of the observed X-ray spectrum represents a narrow-deep or broad-shallow absorption feature. This absorption feature represents an absorption edge and can be modelled with `edge`/`smedge` component in `Xspec`. The absorption feature at 7-8 keV indicates Fe K-edge absorption. The superposition of the continuum model with a reprocessed component from the optically thick accretion disc can explain the broad and shallow absorption feature (Ebisawa, 1991) around 7-10 keV.

The spectra of X-ray sources show turn over $\sim$ 1 keV due to interstellar photoelectric absorption. To account this feature in spectral modelling, we have used interstellar absorption models in `Xspec` namely `phabs` and `tbabs`. These models use different interstellar abundance table and photoelectric cross-section.

2.3.3 Line Emission

The radiation spectra of many X-ray binaries show the characteristic Fe K-shell emission line around 6-7 keV. This emission line is strongest due to the abundance and fluorescence yield of Fe K-shell electron, possibly in the accretion disc. The electrons in the accretion disc make bound-free absorption when hard X-ray photons irradiate the weakly ionised disc. The absorption is followed by X-ray fluorescence, which is seen as an emission line in the X-ray spectrum and is often modelled by a Gaussian profile (`gauss`).

Chapter 3

X-ray Observatories, Data Reduction and Spectral Analysis

The study of astronomical objects in X-ray and gamma-ray bands started in the 1960s. In 1962, Riccardo Giacconi and his group launched an X-ray detecting payload to study the X-ray created by cosmic rays reflected from the moon. But this experiment ended up in detecting the X-ray emission from Scorpius X-1, the brightest X-ray object in the sky. In 1970, the first X-ray astronomy satellite, Uhuru (Giacconi et al., 1971), was launched and it discovered hundreds of X-ray sources. The Einstein observatory (de Korte et al., 1981) was sent to space in 1978 for a detailed study of X-ray sources. Since then many X-ray astronomy missions have been sent to space and few popular ones are EXOSAT (launched by the European Space Agency in 1983), Roentgen Satellite (Truemper, 1982), RXTE (Jahoda et al., 1996), XMM-Newton (Jansen et al., 2001), Chandra X-ray Observatory (Weisskopf et al., 2000), INTEGRAL (Schanne et al., 2003), Swift Observatory (Burrows et al., 2005), the Japanese mission Suzaku (Mitsuda et al., 2007), MAXI (Matsuoka et al., 2009), NuSTAR (Harrison et al., 2010) and AstroSat (Agrawal, 2017).

In this thesis, we have used data from RXTE, Swift, XMM-Newton, and AstroSat. We provide a brief description of these instruments followed by data reduction methods. We highlight the steps involved in extracting different products (image, spectrum, lightcurve) from the reduced data and outline the spectral analysis as well. Also, we have used MAXI one day averaged light curve[1] of H 1743-322 to present the longterm outbursts profile of the source.

[1] http://maxi.riken.jp/mxondem/

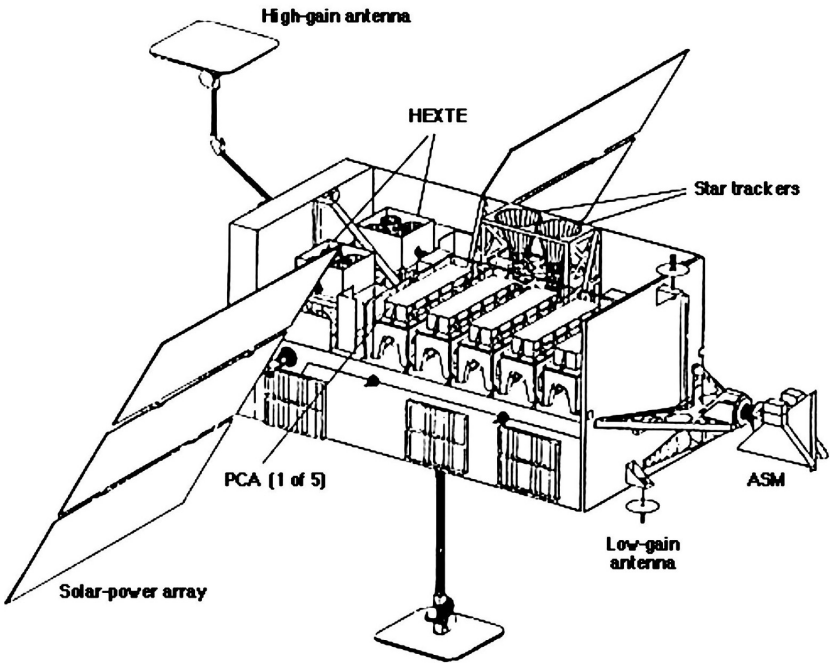

Figure 3.1: Schematic representation of Rossi X-ray timing explorer with five PCA units, two clusters (A & B) of HEXTE and ASM (credit : NASA).

3.1 X-ray Observatories

3.1.1 Rossi X-ray Timing Explorer (RXTE)

The Rossi X-ray timing Explorer was launched by NASA on December 30, 1995 and operated around 16 years. It was placed into a low earth orbit at an altitude of 580 km and 23° inclination with an orbital period of 96 minutes. The main objective of the mission was temporal ($\sim \mu$s) and broadband ($2 - 200\,\mathrm{keV}$) spectral studies of compact X-ray sources. The large area of RXTE provides opportunities to study thousands of X-ray sources. As shown in Figure 3.1, this observatory consists of two pointed instruments: Proportional Counter Array (PCA) and High Energy X-ray Timing Explorer (HEXTE) along with a sky scanning instrument: All Sky Monitor (ASM).

The Proportional Counter Array (PCA, Jahoda et al. (2006)) observes the sources in the energy band 3-60 keV with microsecond time resolution and in 256 energy channels. It comprises of five Proportional Counter Units (PCUs) with effective area $\sim 5000\,\mathrm{cm}^2$ which is described as the product of geometric area with the fractional losses arise due to detection efficiency, shielding, misalignment etc. Each PCU includes an X-ray collimator and three layers of xenon gas sandwiched between two layers of propane gas, which serve

as veto layers to exclude non-X-ray events. The collected data are recorded in different modes with varying time and energy resolution. There are two standard modes which are generally used for observations, whereas other modes are chosen according to the selected science goals. The first standard mode (standard 1) has a time resolution of 0.125 s without energy information, whereas the second standard mode (standard 2) has a time resolution of 16 s and 129 energy channels covering the full energy range of PCA. The average spectral/energy resolution of PCA is $\Delta E/E = 18\,\%\,\mathrm{at}\,6\,\mathrm{keV}$, where ΔE is the width at half the peak height at energy E.

The High Energy X-ray Timing Experiment (HEXTE, Rothschild et al. (1998)), which consists of two clusters (A and B), each carries four NaI/CsI phoswich scintillation detectors. These phoswich detectors are sensitive in the energy range 15-250 keV. Each cluster has a detector with a collecting area of 800 cm^2 and rocks independently in the orthogonal directions between source and background regions i.e., when one of the clusters is observing the source, the other will observe the background and vice versa. HEXTE collects the photons with a time resolution of $8\,\mu\mathrm{s}$.

ASM (Levine et al., 1996) scans the sky in the energy range 1.5-12 keV (with three energy channels 1.5-3.0, 3.0-5.0, and 5.0-12.0 keV) and has a spatial resolution $3' \times 15'$. It has three scanning shadow camera, each with $6^\circ \times 90^\circ$ field of view. ASM data are made public in NASA's High Energy Astrophysics Science Archive Research Centre (HEASARC) website. We have used one day averaged ASM light curves[2] to present the multiple outbursts.

3.1.2 X-ray Multi-Mirror Mission (XMM-Newton)

Figure 3.2: An artistic representation of XMM-Newton telescope. The different mirror assembly is marked on the figure. (credit : ESA)

The X-ray Multi-Mirror Mission (see Figure 3.2) was launched on 10 December 1999 in a 48-hour highly elliptical orbit around the earth. This telescope is equipped with focusing optics and houses six co-aligned instruments, namely three European Photon Imaging

[2] https://heasarc.gsfc.nasa.gov/docs/xte/SOF/asmlc.html

Cameras (EPIC), the two Reflection Grating Spectrometers (RGS) and a 30 cm Optical Monitor (OM). The simultaneous observations in X-ray and optical provide a unique opportunity to study the sources in a wide energy band. The large collecting area and unobstructed long period exposure make this instrument suitable for sensitive observations. We have used EPIC data in this thesis and therefore confine our discussion towards EPIC instruments only.

The EPIC (Jansen et al., 2001) system is comprised of two MOS (Metal Oxide Semiconductor) and a pn camera (Strüder et al., 2001; Turner et al., 2001) with a total field of view (FoV) of $30'$. Each MOS camera has an array of seven MOS-CCDs, and the pn camera has an array of 12 pn-CCDs. The EPIC cameras provide the opportunity of observation in the energy range 0.3-12 keV and have a moderate resolving power ($E/\Delta E \sim 20 - 50$). The pn camera has a very good time resolution of 0.03 ms in the timing mode and 7 μs in the burst mode. The angular or spatial resolution of the instrument is described by point spread function (PSF). The size of the PSF is quantified by the half power diameter (HPD), which is the diameter of the circle containing half of the detected source power. Also, sometimes the PSF is represented with its full width at half maximum (FWHM) and the pn camera has an angular resolution of $6''$.

3.1.3 Neil Gehrels Swift Observatory

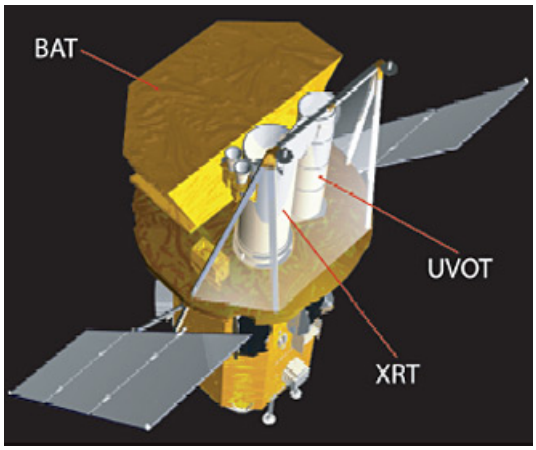

Figure 3.3: Swift telescope equipped with UVOT, XRT and BAT (credit : NASA).

Swift is a NASA's mission launched on 20th November 2004 and it comprises of three instruments: A wide field of view Gamma-Ray Burst Alert Telescope (BAT), narrow field X-ray Telescope (XRT) and an Ultraviolet/Optical Telescope (UVOT). Thus enabling multi-wavelength (gamma-ray, X-ray, ultraviolet and optical) study of compact sources,

though the main objective of the Swift mission is to discover gamma-ray bursts and perform a hard X-ray survey of the sky. A schematic picture of the telescope is shown in Figure 3.3. In our study, we use XRT data and therefore we limit our discussion on XRT only.

The XRT (Burrows et al., 2005) is a Wolter-I type telescope with 3.5 m focal length. It uses grazing incidence to focuses X-rays onto a thermo-electrically cooled CCD having 600×600 pixels. XRT has an effective area of 110 cm^2 and sensitive in the energy range 0.3-10 keV. It has a total FoV of $23'$ with $18''$ HPD angular resolution and 1.8 ms time resolution. The detection sensitivity of XRT is $2 \times 10^{-4}\,\mathrm{erg\,cm^{-2}\,s^{-1}}$ for an exposure of 10^4 s. The XRT has four readout modes, which are image mode (IM), PhotoDiode mode (PD), Windowed Timing mode (WT), and Photon-counting (PC) mode. We have used WT mode data as the sources are bright.

3.1.4 AstroSat Mission

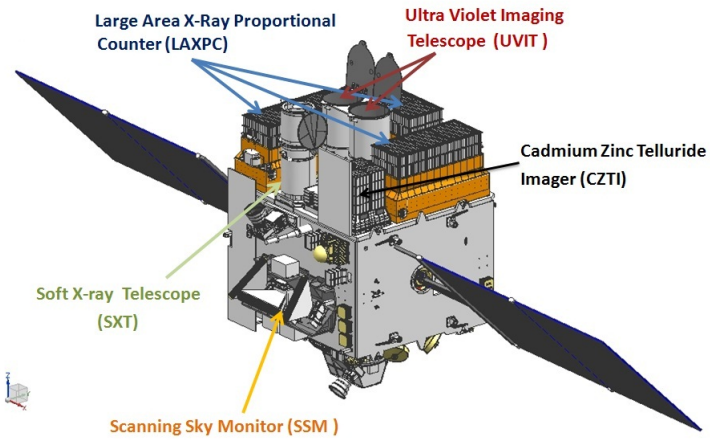

Figure 3.4: A schematic picture of AstroSat. All the scientific instruments, UVIT, SXT, LAXPC, CZTI and SSM are marked on the figure (credit : ISRO).

AstroSat (Agrawal, 2017) is the first dedicated Indian astronomy mission aimed to study celestial sources in broadband simultaneously. This satellite was launched on 28 September 2015 by Indian Space Research Organization (ISRO). The satellite was placed into an orbit of altitude 650 km at an inclination angle 6° to the equator. AstroSat is equipped with five payloads namely Ultraviolet Imaging Telescope (UVIT), Soft X-ray Telescope (SXT), Large Area X-ray Proportional Counter (LAXPC), Cadmium-Zinc-Telluride Imager (CZTI) and a Scanning Sky Monitor (SSM) as shown in Figure 3.4. Different payloads onboard AstroSat cover the energy bands of ultraviolet, X-ray regime (0.5 - 100 keV)

Table 3.1: X-ray instruments and characteristics

Observatory	Instrument	Energy band (keV)	Spatial resolution (FWHM/HPD)	Energy resolution at 6 keV	Time resolution	Effective area (cm^2) at 6 keV
RXTE	PCA HEXTE	2 - 60 15 - 250	1° (collimator) 1° (collimator)	18% 15% @60 keV	1μs 8 μs	5000 890 @33 keV
XMM-Newton	PN	0.3 - 12	6″	2.0%	7 μs	900
Swift	XRT	0.3 - 10	18″ (HPD)	2.3%	2.2 ms	60
AstroSat	SXT LAXPC	0.5 - 8 3.0 - 80	2′ 1° (collimator)	2.5% 12% @22 keV	100 ms 10 μs	60 @0.5 keV, 50 @6 keV 6000 @5-30 keV

with limited optical band. We have used simultaneous SXT and LAXPC data for our study on 1E 1740.7-2942 and GRS 1758-258.

SXT (Singh et al., 2017) works on the principle of grazing incidence in the Wolter-I geometry with a focal length of 2 meters and a geometric area of $\sim 250\,\mathrm{cm}^2$. The X-rays are focused on a 600×600 pixels CCD placed in the focal plane camera assembly. The estimated PSF of the SXT comes around 2 arc minutes. SXT operates in various modes such as Photon Counting (PC), Fast Windowed (FW), Bias Map (BM) and Calibration (Cal). It is capable of doing imaging, spatially resolved spectroscopy and variability observations of cosmic sources in the energy band of 0.3 - 8.0 keV. The SXT has an effective area about 200 cm^2 at 2 keV and it drops to 25 cm^2 at 6 keV.

The LAXPC (Yadav et al., 2016; Antia et al., 2017) consists of three identical proportional counter units having multi-layer geometry, with a detection volume of $100 \times 36 \times 15\,\mathrm{cm}^3$ each. Two LAXPC units are filled with xenon-methane mixture and the third one is filled with xenon-argon-methane mixture. These units are labeled as LAXPC10, LAXPC20, and LAXPC30 respectively. Each LAXPC unit has five anode layers and each layer consists of 12 anode cells of size $100 \times 3 \times 3\,\mathrm{cm}^3$. The LAXPC10 and LAXPC30 have 512 energy channels, while for LAXPC20 goes down to 256 channels. The energy resolution of the detector is $\sim 12\%$ (FWHM) at 22 keV and $\sim 2.5\%$ (FWHM) at 6 keV. The effective area comes around $\sim 6000\,\mathrm{cm}^2$ in 3-15 keV and $\sim 5000\,\mathrm{cm}^2$ in 33-60 keV. The time resolution of the detectors is 10μs and a dead time of about 42μs.

Finally, we summaries the basic properties of all the instruments discussed in Table 3.1.

3.2 Data Reduction and Analysis

All X-ray instruments detect individual photons. It usually measures the energy of the photon, position of energy deposition on the detector and the time of arrival. These basic informations are stored as an event list. In addition, the good events can be discriminated

from the background using grade (or pattern) in the CCD and these are also included in event lists. An event file mainly consists of a binary table extension with the event list and additional informations regarding the status of the instrument. The raw event data are processed to create scientific attributes. This processing differs between instruments and we discuss below the data reduction methods and extraction of scientific outputs of individual instruments used in this thesis.

3.2.1 Data Reduction of RXTE/PCA

We have performed the RXTE/PCA data reduction of GX 339-4 and H 1743-322 using `HEASOFT`[3] package version 6.19 or higher following the tasks given in the RXTE `cookbook`[4]. We decided to work on PCU-2 data only, since it was switched on during the entire period of observations. The standard 2 data of PCA (FS4a*.gz) are used for our study. The good time interval (gti) file is generated for PCU-2, using standard `FTOOLS`[5] task `maketime`. We choose the screening criteria for the data reduction with an elevation angle $> 10\,\mathrm{deg}$ and offset $< 0.02\,\mathrm{deg}$. We run the task `pcabackest` to generate the background data by using the latest bright background model[6] (as the sources are bright). To take care of the satellite crossing the South Atlantic Anomaly (SAA) region, we also include *pca_saa_history* file while creating the background data. Source spectra and background spectra are extracted using the task `saextrct`. Then the response file is created by the task `pcarsp`. The PCA spectrum is generated in the energy range 3-45 keV without any grouping/binning.

3.2.2 Data Reduction of RXTE/HEXTE

HEXTE data of GX 339-4 are reduced by following standard procedures given in the RXTE `cookbook`. We use cluster A archive data (FS52*.gz), cluster B archive data (FS58*.gz), and event mode data (FS50*.gz) for our study. The raw FITS data files contain both source as well as background information. The source and background details can be separated by running the script `hxtback`. To generate source and background spectra the task `saextrct` or `seextrct` are used depending upon whether the observation data is in archive mode or event mode respectively. Since the clusters undergo rocking motion, the

[3] https://heasarc.gsfc.nasa.gov/docs/software/heasoft/
[4] https://heasarc.gsfc.nasa.gov/docs/xte/recipes/cook_book.html
[5] https://heasarc.gsfc.nasa.gov/ftools/
[6] https://heasarc.gsfc.nasa.gov/docs/xte/pca_bkg_epoch.html

off-source time duration is considered as dead time. The dead time correction is done running `hxtdead` and it calculates the true exposure time of the observation. And finally, the detector response is generated using the task `hxtrsp`. HEXTE spectrum is generated in the energy range 15.0-200.0 keV without any grouping or binning.

The cluster A is always observing the source from 20 October 2006 and cluster B is looking at the background from 14 December 2009 because of the failure of rocking motion. So, the HEXTE data reduction procedure is slightly different from December 2009 than discussed earlier. The cluster A background is estimated from the correlation between cluster A and cluster B observed counts on a PHA channel-to-channel basis using the observations when both clusters were undergoing rocking motion. We run the task `hextebackest` on cluster B background FITS file to generate cluster A background file.

3.2.3 Data Reduction of XMM-Newton/pn

The XMM-Newton EPIC archival data are used in our study on GX 339-4. The MOS data are highly piled up and we could not get any useful results. The Observation Data Files (ODF) for pn-CCD are reduced using Science Analysis System (`SAS`) package version 5.22.2 following the procedures given in the `cookbook`[7]. The calibrated photon event files are extracted using the tasks `EPPROC` and `EMPROC` for the pn and MOS detectors, respectively. The events are filtered to reject bad pixels and events close to chip edges by specifying `FLAG=0`. We use `PATTERN`$\leq$`4` to select a single pixel and double pixel event. The source events are extracted over 10 pixels on either side of the brightest part of the image using `eveselect`. The SAS task `EPATPLOT` provides an extent of pile up in the observations. The pile up leads to either a harder spectrum or underestimation of count rates. The pile up correction is done iteratively by removing the central few pixels and generate the spectrum. Then check with `EPATPLOT` until the model and observed pattern match. The source and background extraction area is estimated using the task `backscale`, which also takes care of the chip gaps or bad pixel, and it writes the results into the BACKSCAL keyword of the spectral file. The background extraction is not possible because there is no source free region due to the high brightness of the source. The ancillary response file (ARF) is generated using `arfgen`, and the response file (RMF) is created by the task `rmfgen`. Finally, the spectrum is generated in the energy range 0.5-8.0 keV with a grouping of 20 counts per bin without adding any systematic.

[7] https://heasarc.gsfc.nasa.gov/docs/xmm/abc/

3.2.4 Data Reduction of Swift/XRT

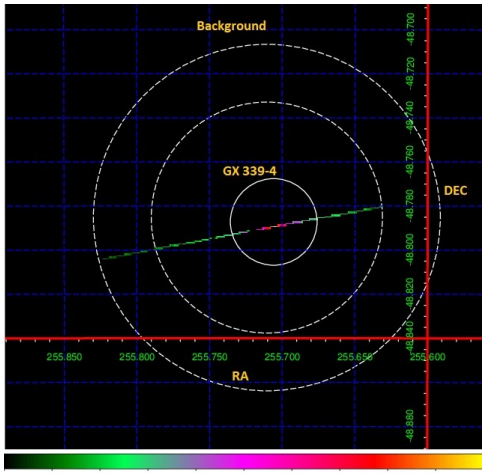

Figure 3.5: Image of GX 339-4 using Swift/XRT is displayed in logarithmic scale. The solid white circular source region has a radius of 30 pixels and the background is selected by the annular region (dotted) with inner radius 70 pixels and outer radius 130 pixels. Both regions are centred at the RA and DEC of the source.

We use Swift/XRT data for our study on GX 339-4. This source is very bright and observations are made in windowed timing (WT) mode which produces a one-dimensional image of the source. The level 2 cleaned event list is produced by running `xrtpipeline`[8] on the Level 1 data and grade 0-2 events are selected. The source and background spectra are generated from the event list using the interface `xselect`. In WT mode, the source is considered to have pile up if the count rate is greater than $100\,\mathrm{counts\,s^{-1}}$. We extract the source contribution from a circular region of radius 30 pixels (Figure 3.5) and we choose an annular region between 70 and 130 pixels to estimate the background if the source is not piled up. In case of pile up, we extract source photons from an annular region having an outer circle of radius 30 pixels, and the inner radius varies with the degree of pile up. Then we edit the BACKSCAL keyword in the source and background spectrum for appropriate background subtraction. We use the required RMF file for the response matrix as prescribed by the instrument team and we generate an ancillary response file using the task `xrtmkarf` for each observation. The spectrum is generated in the energy range 0.3-10 keV with a group of 20 photons per bin without adding systematic.

[8] http://www.swift.ac.uk/analysis/xrt/xrtpipeline.php

3.2.5 Data Reduction of AstroSat/SXT

We have used SXT data in photon counting mode. We generate the cleaned event file using the task `sxtpipeline`[9]. We choose continuous data segments in every orbit excluding the SAA and the earth occultation duration. Then cleaned event files from the individual orbits are merged with executing the task `sxtevtmerger`. The source image is extracted using `xselect` from the merged event file. In the image, we select a circular region of $10'$, centre at the coordinate of the object as the source region. The spectrum and light curve is generated for each of these segments from the selected source region. We use of the sky background spectrum and response (RMF) provided by the SXT team[10]. We generate the ARF file is for individual segments considering the selected region and source position with the task `sxtmkarf`. As suggested by the instrument team, we use `gain fit` command in `Xspec` to flatten the residual at 1.8 keV and 2.2 keV in the spectral modelling.

3.2.6 Data Reduction of AstroSat/LAXPC

We reduce LAXPC data using the software (`laxpcsoft`[11]) provided by the AstroSat instrument team. This is a single routine to extract source spectra, background spectra, and light curves. It mainly contains two Fortran routines. The first Fortran program (`laxpcl1.f`) processes the Level 1 data and generates event file, light curve, source and background spectrum and the GTI file. It takes the attitude file and event data files as inputs along with other interactive options such as LAXPC unit, energy range and bin size. A good time interval is chosen for the elevation angle $> 3.5°$ above earth limb and satellite passing through the SAA region with a longitude greater than $251°$. The data from each orbit is extracted separately from LAXPC10 considering only double events. The second Fortran program (`backshiftv3.f`) applies the gain shift to align the background spectrum with the source spectrum and also it identifies the required response file. We note that during March 2018 LAXPC10 had undergone issues with gas leakage and subsequently the high voltage to the unit was reduced. Hence for the observations during May 2018, we consider only LAXPC20 data.

[9] http://www.tifr.res.in/astrosat_sxt/sxtpipeline.html
[10] http://www.tifr.res.in/astrosat_sxt/dataanalysis.html
[11] http://www.tifr.res.in/~astrosat_laxpc/LaxpcSoft.html

3.3 X-ray Spectral Analysis

The extracted spectrum in §3.2 represents the observed counts in certain energy channels or pulse height bins. This observed spectrum is related to the source spectrum as,

$$C(I) = t_{expo} \int R(I, E) A(E) f_p(E) dE + B(I), \tag{3.1}$$

where $C(I)$ represents the observed counts in channel I and $B(I)$ is the corresponding background counts in the same channel. The source photon flux density at energy E is represented by $f_p(E)$ and t_{expo} is the effective exposure time of the observation. $R(I, E)$ is the instrumental response which is the probability of detecting a photon of energy E in a channel I and $A(E)$ is the effective area of the instrument. In the data reduction process, $R(I, E)$ is encoded in the RMF and the information regarding $A(E)$ is stored in the ARF. To estimate $f_p(E)$, Equation (3.1) needs to be inverted after subtracting the background from the source counts but this is a non-trivial process. Hence, the spectral modelling of the observed data is performed with an assumed model spectrum, $M(E)$. Model counts $C_M(I)$ is estimated by replacing $f_p(E)$ in Equation (3.1) by $M(E)$ and the result is compared with $C(I)$ using a fit statistic. As an example, this can be expressed using χ^2 statistic as,

$$\chi^2 = \sum \frac{[C(I) - C_M(I)]^2}{\sigma_I^2} \tag{3.2}$$

where σ_I is the uncertainty in the counts $C(I)$. We have used `Xspec`[12] version 12.9.1 or higher for spectral modelling. Several additive as well multiplicative spectral models are available in `Xspec`. Users can choose the combination of models based on the underlying physics and the model parameters are estimated minimising the fit statistic. We have performed both phenomenological as well as two-component spectral modelling of the sources considered in this thesis.

[12] https://heasarc.gsfc.nasa.gov/xanadu/xspec

Chapter 4

Spectral and Accretion Evolution of H 1743-322

There have been several spectral studies of the individual outbursts of H 1743-322 in the literature, but a comprehensive study of all of the outbursts in the RXTE era has not been done before. In this chapter, we present a systematic spectral analysis of all eight outbursts during the RXTE era. We have performed spectral modelling of all the RXTE/PCA observations using phenomenological models as well as two-component accretion flow model and estimated the accretion parameters. We study the evolution of accretion dynamics of the source and connect the spectral properties with the accretion parameters. We attempt to understand the evolution of outbursts using irradiated DIM in the presence of both Keplerian and sub-Keplerian component accretion flow. This work is based on our published paper (Aneesha & Mandal, 2020).

4.1 Properties of H 1743-322

H 1743-322 (IGR J17464-3213 or XTE J17464-3213), a low-mass X-ray binary, is categorised as a classical X-ray nova (Lutovinov et al., 2005) with a black hole as a primary. This source is located at RA=$17^h46^m15^s.596$ and Dec=$-32^\circ14'00''.860$. This source shows a two-sided X-ray and radio jet during the 2003 outburst (Corbel et al., 2005). Applying a kinematic model to the trajectories of the jet, the distance to this source is found to be 8.5 ± 0.8 kpc, and the inclination angle of the jet is $75^\circ \pm 3^\circ$. The proper motion of the jet (Corbel et al., 2005) places the source at a maximum distance of 10.4 ± 2.9 kpc. The source has shown both high-frequency as well as low-frequency quasi-periodic oscillations (QPOs) (Homan et al., 2005; Remillard et al., 2006). The presence of a high-frequency QPO gives a strong indication of a high inclination system. The spin of the black hole is

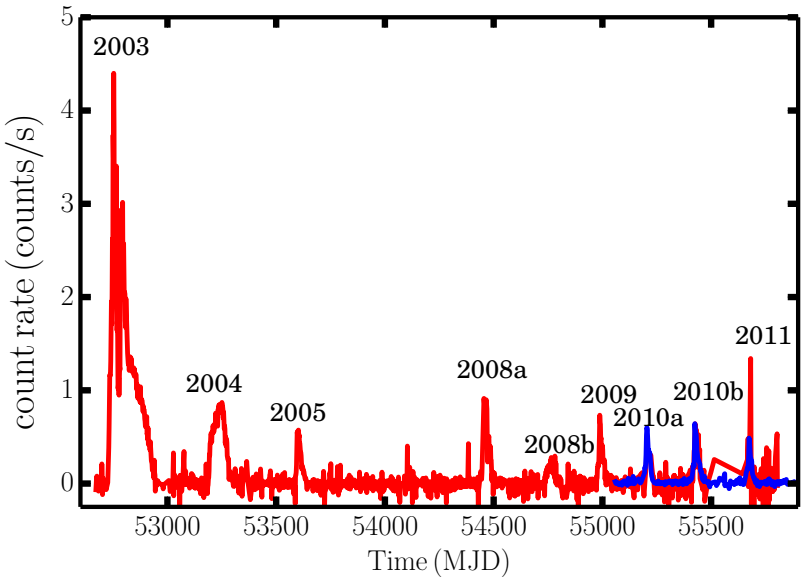

Figure 4.1: RXTE/ASM (2-10 keV) in red colour and MAXI/GSC (2-6 keV) in blue colour represent lightcurves of H 1743-322 in the period 2003-2011. The RXTE/ASM lightcurve is rescaled by a factor of 1/25.

constrained in the range of $-0.3 < a < 0.7$ (Steiner et al., 2012) from X-ray spectral modelling. Even though not much information is available about the nature of the companion star, Chaty et al. (2015) propose that the companion star is a late-type main-sequence star. The mass of the primary has not been dynamically confirmed. However, both timing, as well as spectral studies, reveal the black hole as a primary. Tursunov & Kološ (2018) found the mass to be $11.2M_{\odot}$ and spin to be 0.4 from the magnetic relativistic precession model to explain the twin high-frequency QPOs and low-frequency QPO. By fitting the spectrum using the two-component accretion flow model and the spectral index versus QPO correlation, Molla et al. (2017) estimated the mass of the compact object to be $11.21^{+1.65}_{-1.96}M_{\odot}$. Whereas Bhattacharjee et al. (2017) constrained the mass of the black hole in the range of $10.31M_{\odot} - 14.07M_{\odot}$ from spectral modelling and the evolution of the QPO frequency. Also, Pétri (2008) found $9M_{\odot} \leq M \leq 13M_{\odot}$ using the orbital resonance model to explain high frequency QPOs.

4.1.1 Outburst History of H 1743-322

The first X-ray activity of H 1743-322 was detected by Ariel 5 in 1977 (Kaluzienski & Holt, 1977) and after that, the source was nearly inactive for 25 years. Though the source was detected by EXOSAT in 1984 (Reynolds et al., 1999) and by the TTM/COMIS tele-

Table 4.1: RXTE/PCA observation summary

Outburst	Start date (MJD)	End date (MJD)	Duration (day)
2003	2003 March 28 (52726.8)	2003 November 20 (52963.4)	236.6
2004	2004 July 15 (53201.4)	2004 November 13 (53322)	140
2008a	2008 January 16 (54481.9)	2008 February 08 (54504.9)	58.9
2008b	2008 October 3 (54742.9)	2008 November 19 (54789.5)	46.6
2009	2009 May 29 (54980.4)	2009 July 27 (55039.1)	58.7
2010a	2010 January 17 (55213.2)	2010 February 13 (55240.6)	60
2010b	2010 August 9 (55417.2)	2010 October 09 (55478.2)	60
2011	2011 April 12 (55663.7)	2011 June 11 (55723.9)	60

Note: The RXTE/PCA did not observe the source in the rising phase of the outbursts 2004, 2008a, or 2010a. The triggering time of each outbursts were calculated from Tetarenko et al. (2016) as well as RXTE/ASM and MAXI/GSC light curves (Figure 4.1). The calculated starting times are 2004 June 26 (MJD 53182), 2007 December 12 (MJD 54446.01), and 2009 December 15 (MJD 55180) for 2004, 2008a, and 2010a outbursts, respectively. The outburst durations in the table were calculated from these starting dates for 2004, 2008a, and 2010a.

scope onboard the Mir-Kvant observatory in 1996 (Emelyanov et al., 2000). INTEGRAL detected a major outburst in March 2003, and many space-based, as well as ground-based observatories, carried out the follow-up observations. Using these data, extensive studies on the 2003 outburst have been carried out (Steeghs et al., 2003; Baba et al., 2003; Steiner et al., 2012; Homan et al., 2005; Remillard et al., 2006; Kalemci et al., 2006; Li et al., 2013; McClintock et al., 2009). The source has undergone multiple outbursts with a recurrence period of 0.5 to 1 year after the 2003 outburst. But the 2003 outburst was the brightest and longest outburst of H 1743-322. During the RXTE era, the 2003 outburst was then followed by the 2004 (Rupen et al., 2004; Swank, 2004; Bhattacharjee et al., 2017), 2005 (Swank et al., 2005; Rupen et al., 2005; Coriat et al., 2011), 2008a (Kalemci et al., 2008; Jonker et al., 2010), 2008b (Prat et al., 2009; Motta et al., 2010), 2009 (Motta et al., 2010; Chen et al., 2010; Miller-Jones et al., 2012), 2010a (Zhou et al., 2013), 2010b (Zhou et al., 2013), and 2011 (Zhou et al., 2013) outburst. Multiple outbursts are named by adding *a, b* after the year 2008 and 2010. The RXTE/ASM (red line) and MAXI (blue line) lightcurves of these outbursts are shown in Figure 4.1 between 2003-2011.

4.2 Observations

All RXTE/PCA observations of the source between the 2003 March 28 to 2011 June 22 are summarized in Table 4.1. Since RXTE/PCA did not observe the rising phase of the 2004, 2008a, and 2010a outbursts, we calculate the duration of these outbursts following RXTE/ASM and MAXI/GSC light curves as well as Tetarenko et al. (2016). The start times of these outbursts are 2004 June 26 (MJD 53182), 2007 December 12 (MJD 54446.01), and

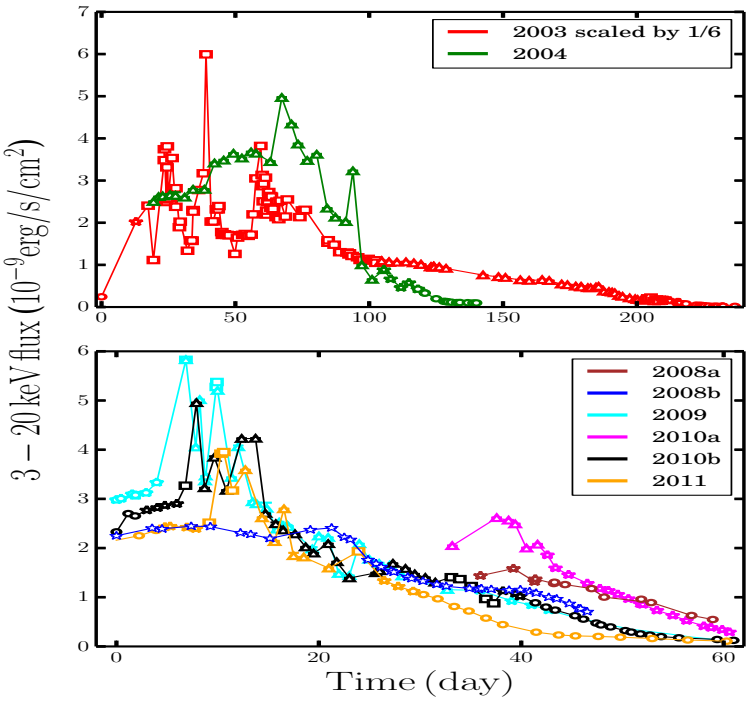

Figure 4.2: RXTE/PCA 3.0-20.0 keV lightcurves of H 1743-322 outbursts during the time period 2003-2011 are drawn. The different colours show different outbursts: 2003 (red); 2004 (green); 2008a (brown); 2008b (blue); 2009 (cyan); 2010a (magenta); 2010b (black); and 2011 (orange). The different symbols represent different spectral states as follows: LHS (circles); HIMS (star); SIMS (square); and HSS (triangle).

2009 December 15 (MJD 55180) for the 2004, 2008a, and 2010a outbursts, respectively. We do not consider the 2005 outburst in our study as very few RXTE/PCA observations are available. Also, we look for simultaneous observations of the source by the other X-ray instruments but did not find any such observation.

4.3 Spectral Modelling : Phenomenology

In this work, we analyse all publicly available RXTE/PCA archival data between the 2003 March 28 to 2011 June 22. The PCA data reduction method is described in §3.2.1. To account for the residual uncertainties in the instrument calibration, a systematic error of 0.5% is added in spectral modelling.

We used phenomenological models, such as `powerlaw`, and/or multi-colour disc blackbody (`diskbb`) (Mitsuda et al., 1984; Makishima et al., 1986) models along with ISM absorption component (`tbabs`) to fit the data. Also, we used additional components, such as the absorption edge (`edge`) and/or the smeared absorption edge (`smedge`) (Ebi-

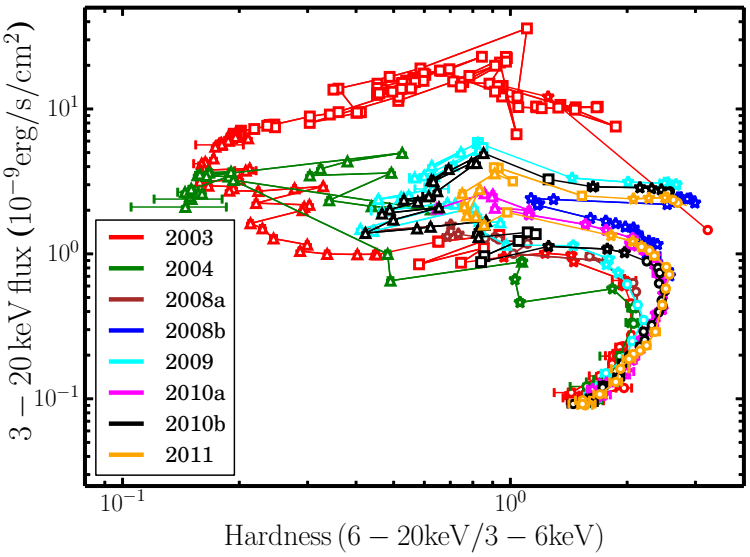

Figure 4.3: HID of eight outbursts of H 1743-322 during 2003-2011 from the PCA spectral data. Each curve begins from the upper right corner (LHS) and moves in an anti-clockwise direction, making a hysteresis pattern. Different colours and symbols have the same meaning as in Figure 4.2.

sawa et al., 1994), a Gaussian profile (`gauss`) in the energy range of 6-7 keV, and a high-energy cut-off (`highecut`) whenever required. These additional models were particularly required to fit the 2003 outburst data, whereas these additional components were only used occasionally to model the other outbursts. For a few observations in 2003, a broken powerlaw (`bknpower`) model was used in place of the `powerlaw` model. The photoelectric absorption with the abundance `wilm` (Wilms et al., 2000) and absorption cross section `vern` (Verner et al., 1996) were used for the spectral fitting. The hydrogen column density (n_H) along the line of sight are quoted in the literature as 1.6×10^{22} cm^{-2} (Capitanio et al., 2009), $1.8 \pm 0.2 \times 10^{22}$ cm^{-2} (Prat et al., 2009), 2.2×10^{22} cm^{-2} (McClintock et al., 2009), and 2.3×10^{22} cm^{-2} (Miller et al., 2006b). We fixed the n_H to 1.8×10^{22} cm^{-2} (Prat et al., 2009) for spectral fitting. We used χ^2 statistics, and the model parameters were estimated within a 90% confidence level using the `migrad` method. The reduced χ^2 of the model fitting comes in the range of 0.7- 1.4. The Gaussian line energy varies between 6.2 to 6.9 keV and the line width is in the range of 0.4 to 1.2 keV.

4.3.1 Outburst Profile and Hardness Intensity Diagram

We have calculated the total flux in the energy range of 3.0-20.0 keV for each PCA observation of H 1743-322 during the period from 2003 to 2011 and created 3.0-20.0 keV PCA lightcurves for all the outbursts, which are shown in Figure 4.2. The day zero of

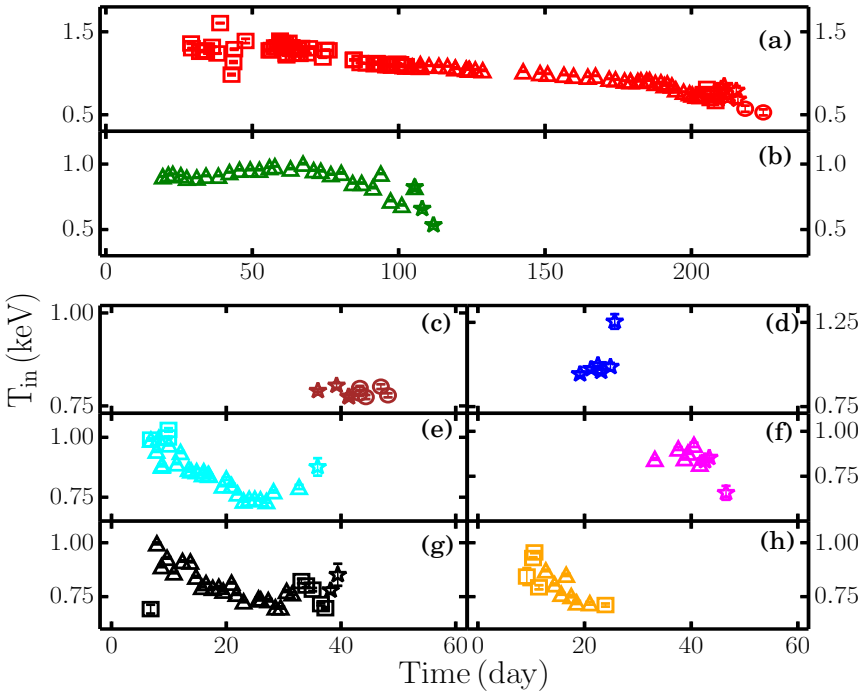

Figure 4.4: Inner disc temperature (T_{in}) evolution for the outbursts (a) 2003, (b) 2004, (c) 2008a, (d) 2008b, (e) 2009, (f) 2010a, (g) 2010b, and (h) 2011 of H 1743-322. Different colours and symbols are the same as in Figure 4.2. The calculated uncertainties (marked within the symbol) are within a 90% confidence range.

each outburst is given in Table 4.1, except for the 2004, 2008a, and 2010a outbursts (see caption of Table 4.1). The spectral state classification of outbursts are discussed in the literature (Chakrabarti et al., 2019; Bhattacharjee et al., 2017; Mondal et al., 2014; Debnath et al., 2013; Zhou et al., 2013; Motta et al., 2010). Here onwards, we use the same colour-coding and symbols as in Figure 4.2 to represent different outbursts and their spectral states throughout this chapter. Since the 2003 outburst is very bright, we have rescaled the flux value by 1/6 in Figure 4.2 for comparison purposes with the other outbursts. RXTE/PCA does not have coverage in the rising part of the 2004, 2008a, and 2010a outbursts, and hence we include the results from the decline part of the outbursts. The 2003 and 2004 outbursts are long-duration outbursts, whereas others have approximately a 60-day duration.

Also, we have calculated the 3-6 keV and 6-20 keV flux from spectral modelling. The ratio of the 6-20 keV flux to the 3-6 keV flux is defined as hardness. The global evolution of spectral states (§1.6) during outburst can be understood from different branches of the hardness-intensity diagram (HID) (Homan & Belloni, 2005; McClintock & Remillard, 2006; Remillard & McClintock, 2006; Belloni, 2010; Nandi et al., 2012; Radhika & Nandi, 2014).

In Figure 4.3, we plot the HID to provide a comparison of different outbursts. As mentioned earlier, RXTE/PCA has full coverage of the 2003, 2008b, 2009, 2010b, and 2011 outbursts, and the HID shows the complete evolution of all the spectral states, aside from 2008b. The HID of all these outbursts (other than 2008b) shows a horizontal branch where a hard to soft state transition occurs at a high flux value in the rising phase, whereas a soft to hard state transition occurs at a lower flux in the declining phase. The system shows a hysteresis pattern, similar to other transient black hole X-ray binaries (Nandi et al., 2018; Belloni et al., 2005; Muñoz-Darias et al., 2013). Whereas for the 2004, 2008a, and 2010a outbursts, the rising part in HID is missing. The 2008b outburst also shows a hysteresis nature, but it has never made a transition to HSS. Thus 2008b outburst is categorised as a failed outburst (Capitanio et al., 2009). All of the other outbursts can be classified as complete outbursts since the source has shown a transition to HSS and then back to the hard state.

4.3.2 Evolution of Spectral Parameters

We have estimated different spectral parameters with their uncertainties from the phenomenological spectral modelling. In Figure 4.4, the evolution of the inner disc temperature (T_{in}) of the `diskbb` model is shown for the (a) 2003, (b) 2004, (c) 2008a, (d) 2008b, (e) 2009, (f) 2010a, (g) 2010b, and (h) 2011 outbursts of H 1743-322. In the rising and declining part of the outbursts, the accretion disc contribution to the flux is very low and hence T_{in} is either small or the disc does not exist in LHS. As the outburst progresses, materials in the accretion disc get accreted to the central black hole and the disc moves inwards. Thus T_{in} increases and maintains roughly a constant value (either HSS or the intermediate state) for long-duration outbursts (the 2003 and 2004 outbursts) of H 1743-322. Generally, T_{in} is higher for the 2003 outburst and reaches a maximum value of 1.6 keV on MJD 52765.836. Finally, T_{in} starts to decrease towards the decline part as there is not much contribution from the accretion disc. The duration of all of the other outbursts is much smaller, typically around 60 days, and the T_{in} evolution is quite fast. We see from Figure 4.4c,d,f that the `diskbb` component is only required for a few observations for the 2008a, 2008b, and 2010a outbursts, respectively. The evolution of the `diskbb` normalisation for all of the outbursts are plotted in Figure 4.5 for the (a) 2003, (b) 2004, (c) 2008a, (d) 2008b, (e) 2009, (f) 2010a (g) 2010b, and (h) 2011 outbursts. The disc norm has higher values for the 2003 and 2004 outbursts (Figure 4.5a,b) and approximately remains constant with high values during the SIMS/HSS over a period of 100 days. Whereas for other outbursts, a

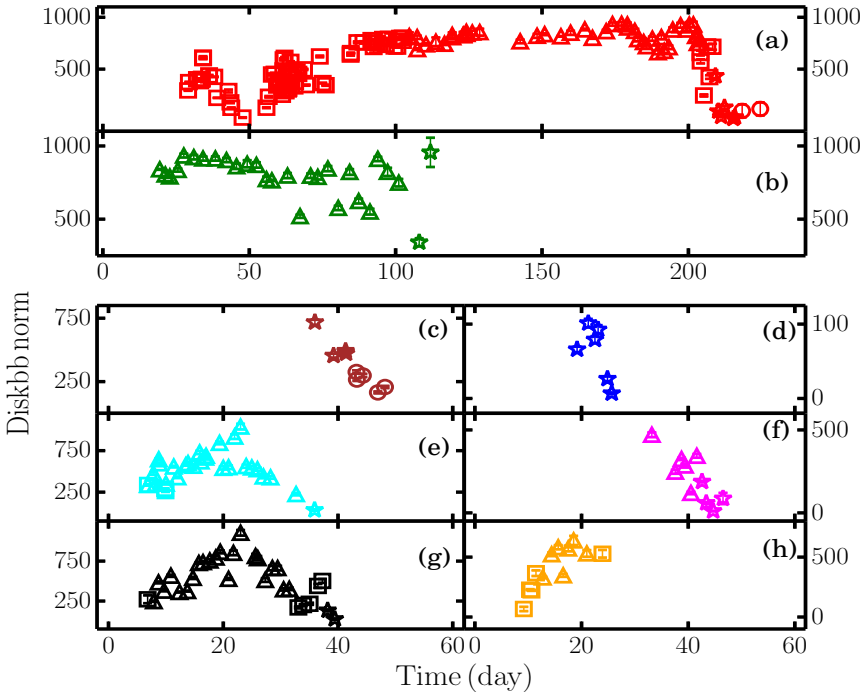

Figure 4.5: Evolution of `diskbb` normalisation for the outbursts (a) 2003, (b) 2004, (c) 2008a, (d) 2008b, (e) 2009, (f) 2010a, (g) 2010b, and (h) 2011 of H 1743-322. Different colours and symbols are same as in Figure 4.2. The calculation of uncertainties are within a 90% confidence range and marked within the symbol.

significant change in the disc norm is observed within HSS.

The evolution of the photon index is shown in Figure 4.6 for the (a) 2003, (b) 2004, (c) 2008a, (d) 2008b, (e) 2009, (f) 2010a, (g) 2010b, and (h) 2011 outbursts. The powerlaw component is required to model the data almost throughout the outbursts. At the beginning of the outburst, the spectrum is hard (LHS), and the photon index is ~ 1.5. As the outburst progresses, the spectrum becomes softer with a photon index, $\Gamma_p \sim 3$ in HSS, and again it decreases towards the decline part of the outbursts. In the 2003 and 2004 outbursts, the photon index reaches close to 3, whereas for other outbursts the highest photon index is close to 2.25. Even though the rising part is missing for the 2004, 2008a, and 2010a outbursts (Figure 4.6b,c,f), these outbursts still confirm the general trend of evolution. The powerlaw normalisation is plotted in Figure 4.7 in the following sequence: the (a) 2003, (b) 2004, (c) 2008a, (d) 2008b, (e) 2009, (f) 2010a (g) 2010b, and (h) 2011 outbursts. The power-law normalisation is defined as photons/keV/cm^2/s at 1 keV. For shorter duration outbursts (Figure 4.7c-h), the powerlaw normalisation shows a sharp increase towards the intermediate state and HSS and then it decreases towards the decline part of the outburst. Whereas the powerlaw normalisation shows a random variation in the rising part of the

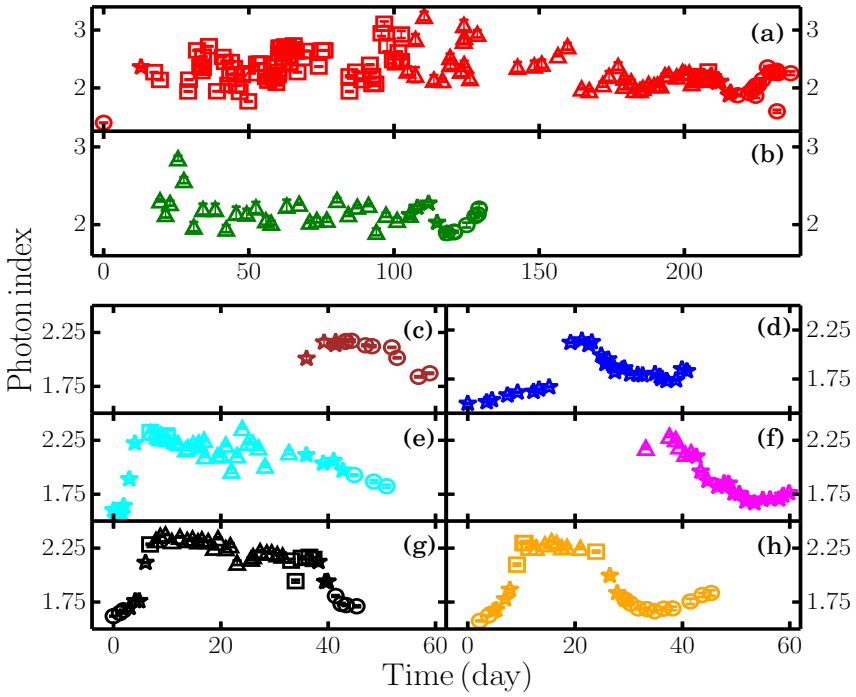

Figure 4.6: Evolution of photon index for (a) 2003, (b) 2004, (c) 2008a, (d) 2008b, (e) 2009, (f) 2010a, (g) 2010b, and (h) 2011 outbursts of H 1743-322. Different colours and symbols have their usual meaning as in Figure 4.2. The calculated uncertainties (marked within the symbol) are within a 90% confidence range.

2003 outburst and stays at a constant low value after 80 days until the end of the outburst. The 2003 outburst is distinctly different from other outbursts due to the presence of a very strong powerlaw component; the highest powerlaw norm is $\sim$ 16 in comparison with $\sim$ 2 for other outbursts.

4.4 Dynamical Spectral Modelling of the Outbursts

We have carried out the spectral modelling of the background subtracted RXTE/PCA data with the two-component model. The rising phase of the 2003 outburst is an order of magnitude brighter than the other outbursts of the source, and we do not able to model this outburst with the two-component accretion flow model. This particular issue is addressed in Section 4.5. Also, we occasionally have used additional model components, such as `gauss`, `edge`, or `smedge`, whenever required since the physical processes responsible for these model components are not included in the two-component model. We have used `tbabs` for the absorption model with the `wilms` abundance table and `vern` (Verner et al., 1996) photoelectric absorption cross-sections. We freeze the line of sight n_H at

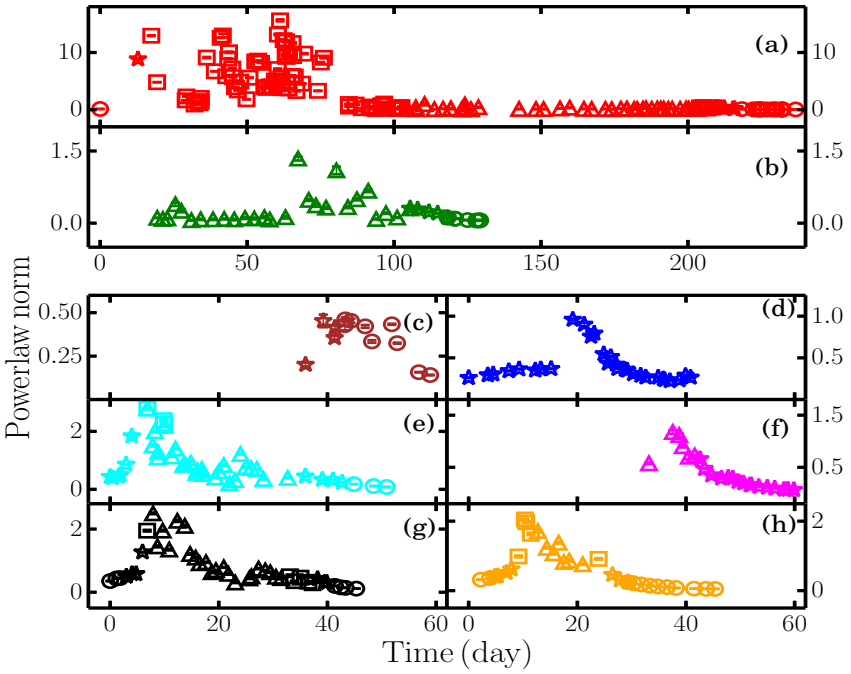

Figure 4.7: Evolution of powerlaw normalisation for the (a) 2003, (b) 2004, (c) 2008a, (d) 2008b, (e) 2009, (f) 2010a, (g) 2010b, and (h) 2011 outbursts of H 1743-322. Different colours and symbols have the same meaning as in Figure 4.2. The 90% uncertainty of the parameter is marked within the symbol.

$1.8 \times 10^{22}\,\mathrm{cm}^{-2}$ (Prat et al., 2009). The χ^2 statistics are used for the spectral fitting. It is found that the value of reduced-χ^2 varies between 0.6 to 1.4. The uncertainty in each parameter is calculated within a 90% confidence level using the `migrad` method. The Gaussian line energy varies between 6.2 - 6.9 keV and line width is in the range of 0.4 keV to 1.2 keV. We have estimated the model parameters from the spectral fitting of each observation data.

4.4.1 Estimation of Accretion Parameters

Even though the dynamical measurement of the mass of the compact object is not present, the spectral fitting with the two-component model provides an opportunity to estimate the mass. We estimated the mass of the source from spectral fitting and is plotted in Figure 4.8 with a 90% confidence error. Since the 2004 outburst has a much longer duration than the other outbursts, and hence the time axis of the 2004 observations are indicated on the top axis. We find that the estimated mass varies between $8.58 - 10.98\,M_{\odot}$ for 90% of the observations. Also, a simple average mass of all the estimates with a standard deviation comes around $9.95 \pm 0.69\,M_{\odot}$. The scattering in the mass estimate may be due

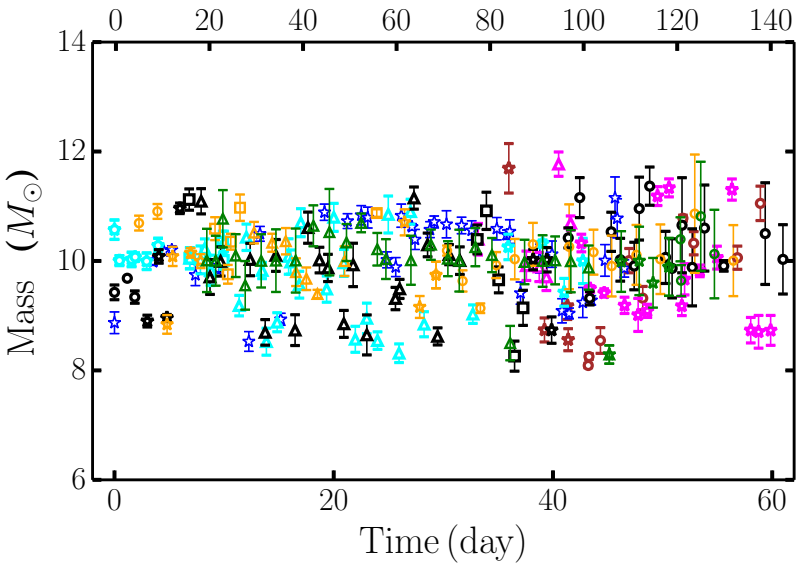

Figure 4.8: The mass estimation of the source from the two-component flow model for different outbursts is drawn here. Different colours and symbols have the same meaning as in Figure 4.2. The uncertainty in mass estimation is quoted within the 90% confidence range and is marked within the symbols. The time axis on top is applicable to only the 2004 outburst (green points).

to the presence of an outflow or jet in LHS which is not the part of the model. Also, the additional model components (`smedge/edge, gauss`) are not consistently calculated from the two-component flow paradigm and hence this may affect the mass estimates. The other accretion parameters such as ($\dot{m}_d$, $\dot{m}_h$, x_s are also estimated with 90% confidence uncertainty for every PCA observations and the time evolution of these parameters are plotted in Figure 4.9 ($\dot{m}_d$), Figure 4.10 ($\dot{m}_h$), and Figure 4.11 (x_s), respectively.

4.4.2 Modelling the Evolution of Accretion Parameters

We attempt to understand the evolution of accretion dynamics using a simple toy model. In a previous study, Mandal & Chakrabarti (2010) used a powerlaw variation of accretion rates to model the HID of GRO J1655-40, but they did not model the observed spectra to extract the flow parameters. Whereas Lipunova (2015) showed that a powerlaw variation of the Keplerian accretion rate could produce a `FRED` profile of outburst.

Here, we use a powerlaw model to study the evolution of accretion parameters since the outbursts of H 1743-322 have a shorter ($\sim$ 10 days) rise time. We assume that the accretion rates ($\dot{m}_d$ and $\dot{m}_h$) vary with time as a powerlaw, whereas x_s moves at a constant speed. We define the following four characteristic time scales: two timescales (t_h, t_s) are associated with $\dot{m}_h$ in the rising and declining phase, respectively; the other two timescales (t_r, t_d)

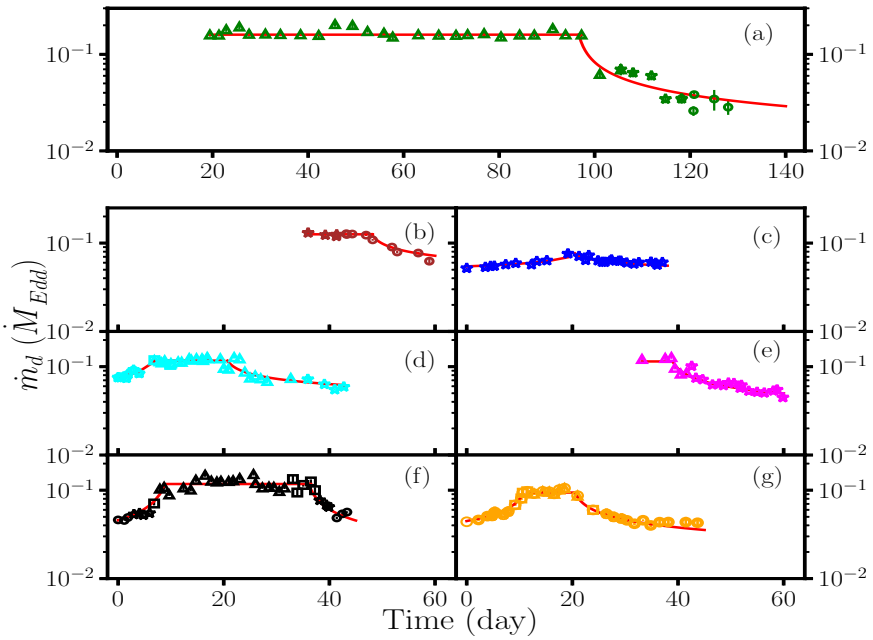

Figure 4.9: Evolution of Keplerian disc accretion rate for the (a) 2004, (b) 2008a, (c) 2008b, (d) 2009, (e) 2010a, (f) 2010b, and (g) 2011 outbursts of H 1743-322. The red solid line represents model fitting using Equation (4.1). Different colours and symbols have the same meaning as in Figure 4.2. The calculated uncertainties (marked within the symbol) are in the 90% confidence range.

are linked with $\dot{m}_d$ in the rising and declining phase, respectively. Since shock can only be present in sub-Keplerian flow, the variation of x_s corresponds to the same time scale as in $\dot{m}_h$. The general behaviour of the time-dependent accretion rates and the shock locations are assumed as follows.

The Keplerian accretion rate evolves with time as

$$\dot{m}_d = \begin{cases} A[(t_r+1)-t]^{\alpha_d}, & t < t_r \\ A, & t_r < t < t_d \\ A[t-(t_d-1)]^{\alpha_d}, & t > t_d \end{cases} \tag{4.1}$$

where A is an average value of the Keplerian accretion rate in the unit of Eddington rate during a highly active phase, t is time in days, and α_d is a free parameter which defines the steepness of the evolution.

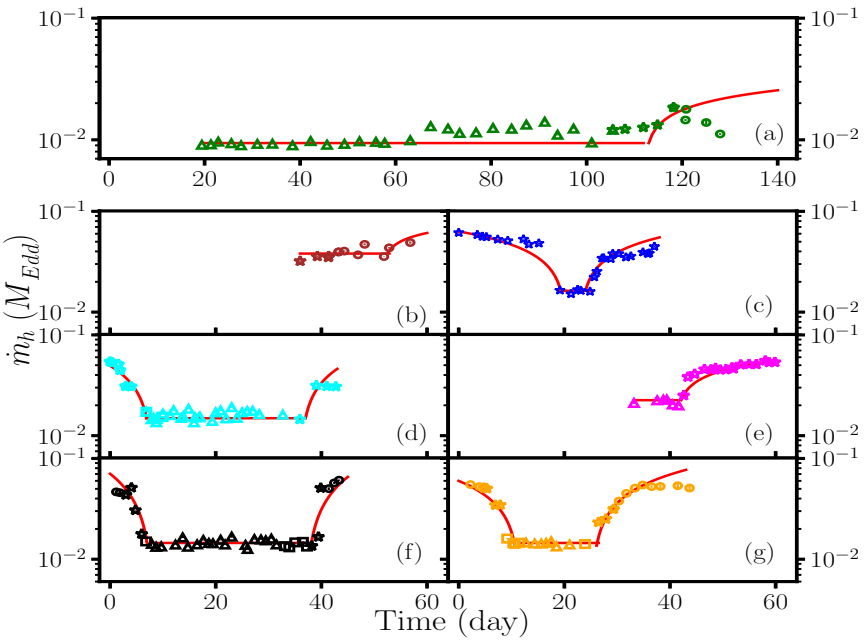

Figure 4.10: Sub-Keplerian accretion rate evolution for the (a) 2004, (b) 2008a, (c) 2008b, (d) 2009, (e) 2010a, (f) 2010b, and (g) 2011 outbursts of H 1743-322. The red solid line represents model fitting using Equation (4.2). Different colours and symbols have the same meaning as in Figure 4.2. We marked the 90% uncertainty of the parameter within the symbol.

The sub-Keplerian accretion rate varies as

$$\dot{m}_h = \begin{cases} B[t_h - (t-1)]^{\beta}, & t < t_h \\ B, & t_h < t < t_s \\ B[t - (t_s - 1)]^{\beta}, & t > t_s \end{cases} \tag{4.2}$$

where B is an average minimum value of $\dot{m}_h$ in the Eddington rate, β is a free parameter, and t is time in days.

The time variation of the shock location is assumed to be

$$x_s = \begin{cases} X_{s_0} - v_0 t, & t < t_h \\ X_{s_i}, & t_h < t < t_s \\ X_{s_i} + v_0(t - t_s), & t > t_s \end{cases} \tag{4.3}$$

where X_{s_0} is the outer most value of shock location at the triggering of the outburst, v_0 is the constant velocity of shock front per day, and X_{s_i} is the inner most location of the shock.

The red solid line in Figure 4.9, Figure 4.10 and Figure 4.11 represents fitting the gen-

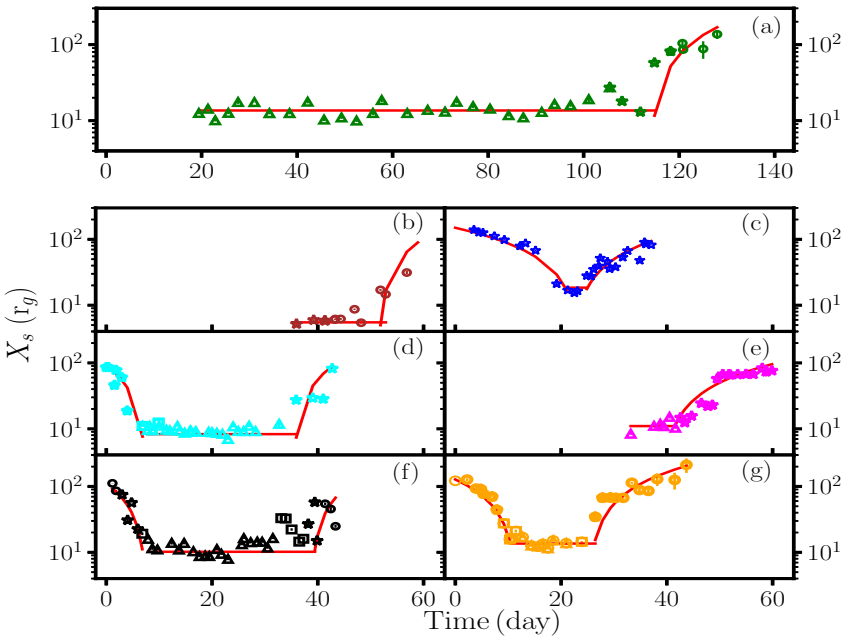

Figure 4.11: Evolution of shock location for the (a) 2004, (b) 2008a, (c) 2008b, (d) 2009, (e) 2010a, (f) 2010b, and (g) 2011 outbursts of H 1743-322. The red solid line represents model fitting using Equation (4.3). Different colours and symbols have the same meaning as in Figure 4.2. The 90% confidence uncertainties are marked within the symbol.

eral trend of $\dot{m}_d$, $\dot{m}_h$ and x_s using Equation (4.1), Equation (4.2), and Equation (4.3) respectively. The best fit parameters in Equations (4.1 - 4.3) are listed in Table 4.2.

In the two-component model, $\dot{m}_d$ directly regulates the soft flux, whereas $\dot{m}_h$ responds to the hard flux (Chakrabarti & Mandal, 2006). Hence, the four time scales should be related to the change in soft and hard flux during the rising and decline phase. In principle, these time scales should not be free parameters; rather, they must be estimated from the soft and hard lightcurves, given a continuous monitoring of the outburst events. We have marked these four times scales during the 2009 outburst as an example in Figure 4.12. The rising time t_r is associated with the first peak in the 3-6 keV lightcurve, whereas t_d is the time scale beyond which there is no more activity at the outer part of the Keplerian disc and the low energy flux smoothly declines. Similarly, t_h represents the first peak in the rising part of 6-20 keV lightcurve, and after time t_s, 6-20 keV flux always remains above the 3-6 keV flux. The crossing over of the soft and hard flux takes place between t_d and t_s. After t_s, the outburst continues to decay to the quiescent state. These features in the lightcurve are very generic to all of the outbursts from the source. The best-fit values of these four-time scales (Table 4.2) for all outbursts closely match with the features marked in Figure 4.12. We were not able to estimate t_r and t_h for the 2004, 2008a, and 2010a outbursts

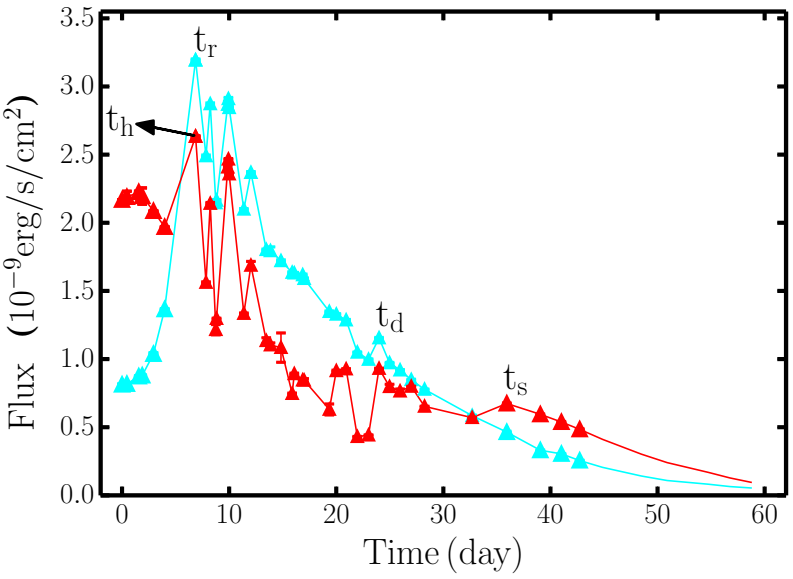

Figure 4.12: 3-6 keV (cyan line) and 6-20 keV (red line) lightcurves of the 2009 outburst are plotted. Different accretion time scales are marked in the represented lightcurves.

since the PCA observations are not available during the rising phase of these outbursts. It is also important to note that a time-lag between t_h and t_r is expected, and the same has been observed (Yu et al., 2004; Aneesha et al., 2019) in many outbursting sources. But it is difficult to detect this time-lag for H 1743-322 as the outbursts rising time is short ($\sim$ 10 days), and the closest interval between successive PCA observations are of the order of a day.

In Table 4.2, the parameter α_d relates to the stiffness of the rise and declination of the soft photons and A is the average value of $\dot{m}_d$ during the active phase. Whereas the parameters β and B represent the same for $\dot{m}_h$. In general, β is higher than α_d as the former corresponds to the radiative cooling time scale whereas the later is related to the viscous time scale. Also the higher the value of A, the brighter the outburst and B remains very low during the active phase. The 2004 outburst is brighter than the other outbursts with a higher value of A and having the smallest value of B. The values of these parameters for other outbursts are similar, except for 2008b which is identified as a failed outburst.

The shock location (x_s) controls the relative ratio of the soft and hard photons (Mandal & Chakrabarti, 2005; Chakrabarti & Mandal, 2006) and hence the spectral index. The location of the shock and hence the size of the PSR changes due to the inverse Compton cooling by the soft photons from the Keplerian disc. Thus the shock moves inwards as $\dot{m}_d$ increases and simultaneously $\dot{m}_h$ also decreases, transiting the source into a spectrally soft state. The initial value, X_{s_0}, can be thought of as the inner edge of the Keplerian disc at

Table 4.2: Model parameters for the evolution of $\dot{m}_d$, $\dot{m}_h$, and x_s

Outbursts	Time (day)				α_d	A	B	β	X_{s_0}	X_{s_i}	v_0
	t_r	t_h	t_d	t_s					(r_g)	(r_g)	(r_g/day)
2004	-	-	96.7	113.0	-0.45	0.16	0.009	0.3	-	13.6	12.0
2008a	-	-	48.0	52.5	-0.17	0.115	0.038	0.22	-	5.5	12.0
2008b	20.6	19.3	20.6	24.0	-0.11	0.076	0.016	0.45	150.0	18.5	6.3
2009	6.9	6.9	20.7	37.0	-0.29	0.135	0.015	0.58	90.0	8.3	12.0
2010a	-	-	39	42.1	-0.28	0.116	0.023	0.31	-	11.0	4.6
2010b	8.8	7.0	36.1	38.0	-0.27	0.091	0.015	0.76	109.4	10.2	14.5
2011	10.7	10.5	20.5	26.2	-0.26	0.087	0.015	0.58	127.8	13.6	11.0

the beginning of the outburst. We were not able to quote its value for the 2004, 2008a, and 2010a outburst as the rising phase data are not available. The closest value of the shock location generally remains $\sim 10\, r_g$ during HSS but it can reach close to $\sim 5 r_g$ as well. We assumed a constant shock speed, which is sufficient for the present work but in general it may be in accelerating motion (Chatterjee et al., 2016; Nandi et al., 2018) as well. The values of the parameters in Table 4.2 fit the general profile of the accretion parameters (Figure 4.9, 4.10, and 4.11) and the quoted values were estimated manually by minimising χ^2. Since this is a manual fitting, we were not able to estimate the error in the parameters and this is one of the caveats in the present work.

4.4.3 Irradiated DIM in the Two-Component Flow Scenario

We attempt to understand the general behaviour of the evolution of accretion parameters in light of the irradiated DIM (§1.5) under the two-component flow scenario. In the two-component flow model, the accretion activity, if any, during the quiescent state is purely sub-Keplerian in nature, and the source remains faint as the sub-Keplerain flow is generally radiatively inefficient. The outburst is triggered due to the thermo-viscous instability in the Keplerian disc, and it enters into a hot state with the enhancement of viscosity, which allows matter to accrete. This increases the supply of soft photons and hence hard photons as well due to inverse Comptonisation at the PSR. Also, the Keplerian disc moves inward (x_s decreases in Figure 4.11). The enhanced luminosity of the central region irradiates the outer part of the disc, and the entire Keplerian disc transfers into a hot phase. Since the sub-Keplerian disc sandwiches the Keplerian disc from top to bottom, the effect of irradiation at the outer part of the disc converts the sub-Keplerian matter into Keplerian matter (Giri & Chakrabarti, 2013) due to enhancement of viscosity. This reduces $\dot{m}_h$ and it remains at a very low value (Figure 4.10) as long as irradiation is active. During the irradiation phase,

$\dot{m}_d$ remains high (Figure 4.9) above a critical disc accretion rate ($\dot{m}_{dc}$), which makes the system persistent. The effect of irradiation, as well as outburst activity, reduces when a significant fraction of matter in the Keplerian disc is being accreted by the central source. Hence, the Keplerian disc recedes outwards (x_s increases in Figure 4.11), and reduction of viscosity switches the Keplerian disc to a cold state. This allows the sub-Keplerain flow to rebuild. The evolution of accretion parameters (§4.4.2) are consistent with this picture. The approximately constant level in Figure 4.9, 4.10 represent the irradiation phase and a brighter outburst is associated with a higher the value of A, and a lower B.

The 2008b outburst has the least value of $A = 0.076$ and $\alpha_d = -0.11$ (Table 4.2). Also, the hard flux always dominates over the soft flux for the 2008b outburst with a very different value for t_h and t_r than the other outbursts. In this case, the outburst never progresses to an irradiation phase (Figure 4.9c), and $\dot{m}_d$ does not cross the critical accretion rate ($\dot{m}_{dc}$) required to switch to an active phase. Also, Table 4.2 shows that $A = 0.087$ leads to a full outburst in 2011. Therefore, the 2008b outburst (marked with blue in Figure 4.3) marginally failed to produce a full outburst and these outbursts (2008b and 2011) provide a constrain on $\dot{m}_{dc}$ of the system within a narrow range of $0.076 < \dot{m}_{dc} < 0.086$.

Since the 2003 outburst was triggered after a very long quiescent, the system had enough time to accumulate matter and build an extended Keplerian disc. The outburst must have been triggered at the outer part of the Keplerian disc. The high viscosity during the hot phase (Cannizzo et al., 1995; Lipunova, 2015) may possibly result a longer irradiation phase which allows the outburst to continue over 200 days. The 2004 outburst was possibly produced from the unused matter of 2003 (Chakrabarti et al., 2019) and could continue to produce another long outburst (Figure 4.9a), but one that is much weaker than the 2003 outburst. Whereas, the outbursts between 2008 - 2011 are more frequent, fainter outbursts with a duration of $\sim$ 60 days. This may indicate that the strong irradiation in 2003 has affected the secondary in addition to push the pileup radius inside.

The three prompt peaks (red points in Figure 4.2), which are separated by 10-15 days, in the 2003 lightcurve reveal this interesting observation. We understand that the first peak indicates the triggering of the outburst, whereas the second and third peaks are associated with irradiation of the outer disc and secondary, respectively. The illumination due to irradiation may result in additional mass loss from the secondary (Augusteijn et al., 1993; Chen et al., 1993) and generates this kind of flickering in the lightcurve. We also see flickering, with the time scale of 3-5 days, in the lightcurves of the 2009, 2010b, and 2011 outbursts. But this cannot be due to the irradiation effect on the secondary as the time scale is too short. Rather it may be due to the local instability that generated inside the disc by

the competition between different radiative cooling time scales, which disturb the energy balance. Whereas Janiuk & Czerny (2011) have proposed that this small scale flickering may originate since the magnetic field works in the local dynamical scale but the magnetic cell size is of the order of the disc height.

4.4.4 Expected Orbital Parameters

The orbital parameters for H 1743-322 are not known and we predict some of these values using the estimated $\dot{m}_{dc}$ and m_{bh} values. We assume $m_{bh} = 10.0$ (§4.4.1) and $\dot{m}_{dc} = 0.085$ based on the constrain put by 2008b and 2011 outbursts. We can calculate the outer radius (King & Ritter, 1998) of the Keplerian disc or the location of triggering an outburst as,

$$R_0 = 2.7 \times 10^{11} (m_{bh}\, \dot{m}_{dc})^{1/2} \quad \mathrm{cm}, \tag{4.4}$$

which becomes $R_0 = 2.5 \times 10^{11}\,\mathrm{cm}$. Similarly, the orbital period (P_{orb}) of the system can be calculate as (Frank et al., 1992),

$$\dot{m} = 5 \times 10^{-2}\, m_{bh}^{-1/3} P_{orb}^{4/3}. \tag{4.5}$$

Again assuming, $m_{bh} = 10.0$ and $\dot{m} = \dot{m}_{dc}$, we estimate $P_{orb} = 15.07\,\mathrm{hr}$. The secondary is a late-type main-sequence star (Chaty et al., 2015) and the mass of the secondary can be estimated (Frank et al., 1992) as $0.11\ P_{orb} = 1.65$ and hence the mass ratio of the system is $q = 0.13$. Also, we can estimate the accretion disc temperature (Equation 1.8) and hence the sound speed at R_0 using $\dot{m}_{dc}$, m_{bh} and an assumed the viscosity parameter $\alpha_{vis} = 0.1$ in the hot state as $c_s = 1.2 \times 10^6\,\mathrm{cm\,s^{-1}}$. The rising time (Frank et al., 1992) of the outburst $t_r = R_0/\alpha_{vis}\, c_s \sim 25\,\mathrm{days}$ matches well with the rising time of the 2003 outburst. Whereas all of the other complete outbursts are having $7-10$ day rise time and hence these outbursts may have triggered at a distance half of R_0.

4.5 Modelling the 2003 Outburst

The 2003 outburst of H 1743-322 is very bright and has a long duration, which differs from the other outbursts of the source. We have tried to fit the outburst spectra using the `Xspec` implemented two-component flow model and understood that it is not possible to model the entire outburst using an accretion disc model alone. To illustrate the situation better, we have used the phenomenological model fitting results described in §4.3.2 of the outbursts

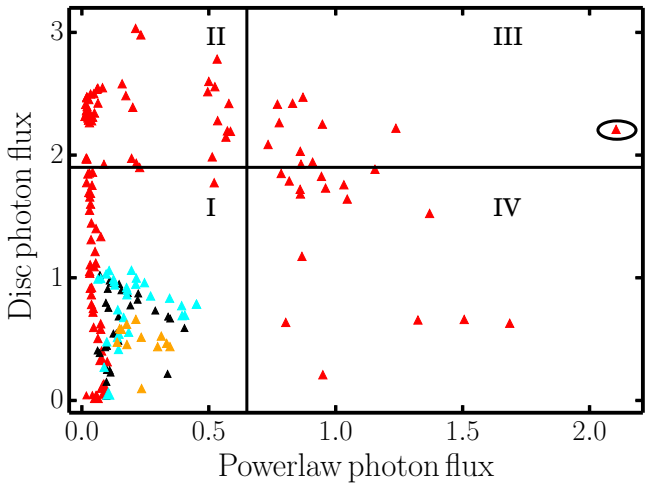

Figure 4.13: Plot shows blackbody photon flux and the powerlaw photon flux required to model the data when both components are present. The outburst data with full PCA coverage are plotted as: 2003 (red), 2009 (cyan), 2010b (black), and 2011(orange). The different regions (I - IV) represent the validity of the current model and possible modifications (see text for details). The data point marked by a small ellipse corresponds to the highest peak of the 2003 outburst and was modelled by the modified two-component model (see Figure 4.14).

having full PCA coverage. We would like to understand the relative contribution of the blackbody and powerlaw component. Therefore, we use only those observations which can be modelled by `diskbb+powerlaw`. The powerlaw photon flux between energy E_1 and E_2 can be calculated as $\frac{N_p}{\Gamma_p - 1}(E_1^{1-\Gamma_p} - E_2^{1-\Gamma_p})$, where N_p is the powerlaw normalisation and Γ_p is the photon index. Similarly, the total blackbody photon flux can be estimated as $2.4 \times 10^{-3} N_d \, T_{in}^3$, where N_d and T_{in} represent the `diskbb` norm and inner disc temperature of the Keplerian disc. In Figure 4.13, we plot the 3-20 keV blackbody photon flux versus the powerlaw photon flux for the 2003 (red), 2009 (cyan), 2010b (black), and 2011 (orange) outbursts. We divide the entire plot into four regions (I, II, III, and IV). All of the observations in the region I can be modelled using the existing version of the two-component flow model, and hence we could model all of the outbursts except for the 2003 outburst. In the two-component model, the blackbody spectrum is calculated using the effective temperature, $T_{\rm eff}$ (Equation 1.8), of the accretion disc. But at a higher accretion rate $\dot{m}_d$, the spectrum calculation needs to be modified by the colour temperature $T_c = \xi \, T_{\rm eff}$ (Shimura & Takahara, 1995), where ξ is the hardening factor. The high value of disc flux in region II corresponds to high accretion rate and therefore, the disc blackbody spectrum needs to be calculated using T_c to model the observations in region II. If the high energy photons are solely produced by the inverse Comptonisation of the blackbody photons, then the ob-

servations in region IV require inverse Comptonisation of more than 50% of the blackbody photons. This is very much unlikely that such a high fraction of blackbody photons are going to intercept the PSR. Also, there are more number of non-thermal photons than the disc blackbody photons for a few observations in region IV. This indicates the requirement of an additional source of non-thermal photons to explain the observations in region IV along with the two-component model. In fact, this should be true for any physical model, and it shows the difference between a phenomenological model and a physical model. In the phenomenological model, all of the components are independent, and hence it does not justify that given a blackbody temperature, the observed spectral index and number of high energy photons can be created or not. In region III, the two-component model needs to be modified using the colour temperature as well as an additional source of non-thermal photons, are required to model the data. Hence, we are not able to model the observations in regions II-IV. To illustrate the above picture, we have modelled the observation on MJD 52765.836, which corresponds to the highest flux in the 2003 outburst and is marked by an ellipse in Figure 4.13. We have modified the two-component model source code to incorporate the colour temperature and we have fitted the data by running the source code manually. Also, we use an additional `powerlaw` component as a source of non-thermal photons and the fitted result is shown in Figure 4.14. The model fitted parameters are $m_{bh} = 10.0 \pm 0.13$, $\dot{m}_d = 1.698 \pm 0.034$, $\dot{m}_h = 0.152 \pm 0.014$, $x_s = 6.58 \pm 0.03$, $\xi = 2.96 \pm 0.01$, and the photon index is $\Gamma_p = 2.28 \pm 0.01$ with reduced $\chi^2 = 0.89$. The estimated X-ray flux under the powerlaw component is $2.5 \times 10^{-8} \mathrm{erg/cm^2/sec}$. The 2003 outburst showed continuous radio activity (McClintock et al., 2009) throughout the outburst even in SIMS and HSS, meaning that there is a significant non-thermal contribution in the X-ray spectrum. We propose that the additional powerlaw component, required to explain the X-ray observation, is originated from the jet.

4.5.1 X-ray Flux and Jet Kinetic Power

Jets are known to harbour non-thermal particles due to acceleration across the shock front. We assume that presence of standing shocks close to base of the jet (Vyas & Chattopadhyay, 2017) may produce non-thermal electrons. We attempt to estimate the X-ray flux due to non-thermal synchrotron emission at the base of the jet using typical jet parameters. We assume that 10% (Kumar & Chattopadhyay, 2013) of the accreted matter is being ejected as jet. We calculate the density of material in the jet as $\rho = \dot{m}_j / \Omega v x^2$, where $\dot{m}_j$ is the mass outflow rate, $\Omega = 2\pi(1 - cos\,\theta)$, θ is the opening angle of the jet, and $v = x^{-1/2}$. Here the

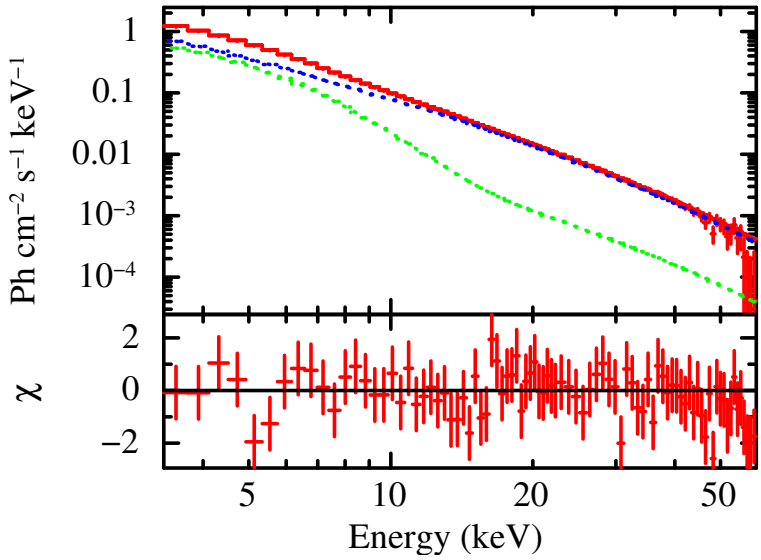

Figure 4.14: Modelling of the 2003 outburst data (red) on MJD 52765.836 using the two-component model (green) with an additional powerlaw (blue).

radial distance (x) and flow speed (v) are expressed in the unit of r_g and the speed of light (c). Using the mass and accretion rate from X-ray spectral modelling, assuming $\theta = 30^o$, $x = 20$, we calculate the number density of electrons as $7.5 \times 10^{16}\mathrm{cm}^{-3}$ and an equipartition magnetic field 7.5×10^6 Gauss. The photon index from X-ray spectral modelling ($\Gamma_p = 2.28$) corresponds to a non-thermal electron distribution of the index $p = 3.56$. The emitted luminosity in 3-20 keV is $7.9 \times 10^{38}\mathrm{erg/sec}$ (Equation 2.25). Assuming a distance of $8.5\,\mathrm{kpc}$ and an inclination angle of 75^o, the estimated flux is $2.4 \times 10^{-8}\mathrm{erg/cm^2/sec}$, which is close to the observed X-ray flux under `powerlaw` component. Also, we find radio observations (McClintock et al., 2009) at 4.86 GHz and 8.46 GHz, which are 10 hr before and 1.7 days after the PCA observation. The reported radio fluxes are 13.78 mJy and 11.12 mJy before the PCA observation, respectively, whereas the radio fluxes are 25.62 mJy and 23.02 mJy after the PCA observation, respectively. Using the observed radio flux S_ν at the frequency ν, we estimate the observed kinetic jet power (Longair, 2011; Nandi et al., 2018) to be

$$L_j \sim 3 \times 10^{33} f(\gamma, i) \times \left(\frac{\Delta t}{sec}\right)^{2/7} \left(\frac{\nu}{GHz}\right)^{2/7} \left(\frac{S_\nu}{mJy}\right)^{4/7} \left(\frac{D}{kpc}\right)^{8/7} \mathrm{erg/sec}, \tag{4.6}$$

where $f(\gamma, i)$ (Fender, 2001) represents the Doppler boosting factor for the bulk Lorentz factor γ and the inclination angle (i). The other factors Δt and D are the rise time of jet

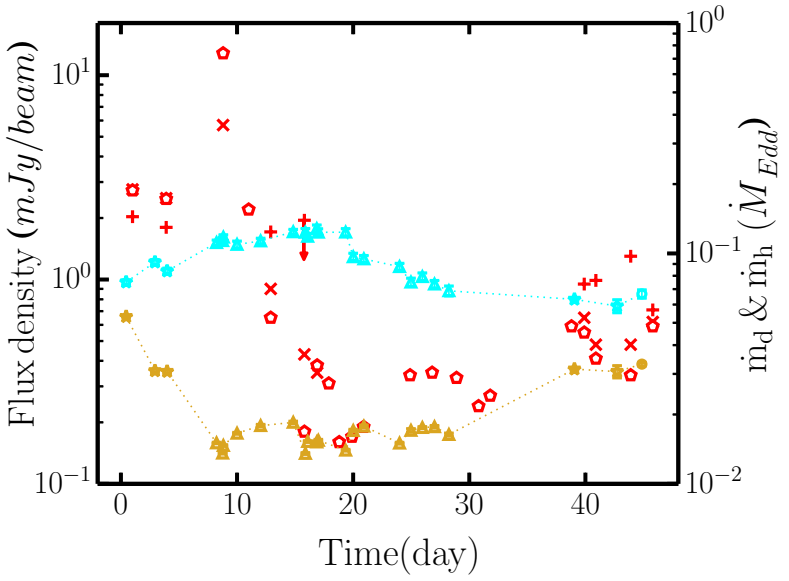

Figure 4.15: Evolution of radio flux density (red) along with the Keplerian disc accretion rate (cyan) and sub-Keplerian accretion rate (gold) are shown for the 2009 outburst. The symbols in red represent the radio flux density at 1.4 GHz (plus), 4.9 GHz (cross), and 8.4 GHz (pentagon), respectively. The 3σ upper limit of the 1.4 GHz radio data on MJD 54996.2 is indicated by a downward arrow. The accretion rates in different spectral states are marked by the same symbols (triangle for HSS and star for HIMS). The left vertical axis represents the radio flux density, whereas the right vertical axis shows the accretion rates.

and the distance to the source, respectively. For an assumed $\gamma = 2$ (mildly relativistic jet) and $i = 75^o$, we calculate $f(\gamma, i) = 7.47$. We take $\Delta t = 24\,\mathrm{hrs}$ and $D = 8.5\,\mathrm{kpc}$, and by using the observed radio flux (25.62 mJy at 4.86 GHz) we estimate the jet kinetic power as $6.5 \times 10^{37}\mathrm{erg/sec}$. This can easily be produced by the available jet energy budget $\eta_j \dot{m}_j\, c^2 = 6.9 \times 10^{37}\,\mathrm{erg/sec}$ with $\eta_j = 3\%$. The consistency of the X-ray and radio observations with typical values of outflow parameters support the jet origin of the non-thermal contribution. Hence, a combined accretion disc-jet model applied to both X-ray and radio observations are required to better understand the 2003 outburst, which we aim to attempt in the future.

4.6 Connecting Jet Activity with the Accretion Dynamics

We have tried to connect the accretion dynamics to the ejection of a jet using radio observations of outbursts other than the 2003 outburst. We find good radio coverage for the 2009 outburst (Miller-Jones et al., 2012). To understand the radio and X-ray connection, in Figure 4.15, we plot the radio lightcurve along with the model fitted $\dot{m}_d$ and $\dot{m}_h$ for

the X-ray observations within a day before the radio observation. The radio observations are available only in HIMS (star) and HSS (triangle). In the rising phase of the outburst, a steady radio flux is observed in HIMS with low $\dot{m}_d$ and a significant hard X-ray flux. The steady radio flux is possibly associated with a compact jet and indicates the coupling of the accretion disc, PSR with the compact jet. In fact, the Very Large Baseline Array (VLBA) images (Miller-Jones et al., 2012) of the source at 8.4 GHz clearly shown the presence of an unresolved compact jet during this period (MJD 54979.35, 54981.35, and 54984.35). Whereas a transient jet is observed in the VLBA images on MJD 54987.33 and MJD 54988.33. This corresponds to the highest radio flux in Figure 4.15 at the beginning of the HSS, which is a characteristic of a spectral state transition from HIMS/SIMS to HSS observed in many outbursting sources (Corbel et al., 2004; Brocksopp et al., 2005; Radhika & Nandi, 2014). This transient radio activity is associated with an increase of $\dot{m}_d$ and a sharp decrease of $\dot{m}_h$. The radio flux density decreases sharply in the HSS and remains at a very low level. This is due to the quenching of a jet since a high $\dot{m}_d$ can completely cool the PSR with a very small $\dot{m}_h$. Towards the end of HSS state, the radio flux starts increasing, which represents the reappearance of a compact jet due to an increase of $\dot{m}_h$ in the presence of PSR, and it reaches a steady value towards the decline part of the outburst.

4.7 Discussion

In this chapter, we have attempted to understand both the spectral as well as dynamical evolution of outbursts shown by H 1743-322 using RXTE/PCA data. The 2003 and 2004 outburst lightcurves (Figure 4.2) have a long duration whereas others have a duration of ~ 60 days with a regular recurrence period of $7-9$ months (Table 4.1). Like other outbursting XRBs, this source also shows a canonical HID pattern (Figure 4.3) and spectral state transitions during outbursts. The 2003 and 2004 outbursts are more luminous and have reached a much softer state (hardness ratio ~ 0.15) in comparison to other outbursts (hardness ratio ~ 0.4). We see from the spectral fitting (Figures 4.4 and 4.5) that in the LHS (both beginning and end) of outbursts, the `diskbb` component is not present (or very weak), whereas the powerlaw component (Figure 4.6) is hard ($\Gamma_p \sim 1.5$). This can be understood from the combined role of accretion parameters. During LHS, $\dot{m}_d$ is low (Figure 4.9), the inner edge of the disc x_s (Figure 4.11) is further apart, and hence there are not as many soft photons. Whereas $\dot{m}_h$ is high, and hence electrons in the PSR are hot. The net result is a hard spectrum due to strong inverse-Comptonisation by PSR. As the outburst progress towards intermediate states, T_{in} increases, and `diskbb norm` (Figure 4.5) is at

its maximum in the HSS, except for 2008b where the diskbb norm is much lower and the outburst never progresses to HSS. The source luminosity increases, and the spectrum becomes softer as Γ_p increases along with the increase of powerlaw norm (Figure 4.7). This is supported by the increase of $\dot{m}_d$ (Figure 4.9) and decrease of x_s (Figure 4.11), which increase the supply of soft photons, whereas decreases in $\dot{m}_h$ (Figure 4.9) and the size of PSR (x_s) reduce the supply of hot electrons. This enhances the cooling of PSR, producing a softer spectrum. In HSS of the 2003 and 2004 outbursts, the photon index reaches ~ 3, whereas other outburst spectra are relatively harder. During the decline phase, the behaviour of the accretion parameters are the reverse.

The mass of the central object is one of the parameters in the hydrodynamic model, and we estimate the mass of the source (Figure 4.8) for all of the observations which remain within $8.58 - 10.98\, M_\odot$ for 90% of the observations. We use a powerlaw variation of accretion rates (Equation 4.1,4.2) with constant motion of x_s to understand the evolution of the accretion parameters. We have fitted the observed data (red line in Figures 4.9, 4.10, and 4.11) by the proposed toy model and listed the parameters in Table 4.2. We identify the rise and decline timescale of $\dot{m}_d$ (t_r, t_d) and $\dot{m}_h$ (t_h, t_s) in the $3 - 6$ keV and $6 - 20$ keV lightcurves (Figure 4.12) of the outbursts. In principle, these time scales can be determined from the lightcurves, given continuous monitoring of the outburst events. We see from Table 4.2 that the parameter β is higher than α_d as the sub-Keplerian flow responds faster than the Keplerian flow. Also, the higher the value of A, the brighter the outburst is. During irradiation, $\dot{m}_d$ is high and there are changes around A, whereas $\dot{m}_h$ remains at a low value. Also a closer Keplerian disc (x_{si}) makes the central region luminous. After the end of the irradiation phase, the Keplerian disc recedes, and the sub-Keplerain flow starts to build. The 2008b outburst has the least $A = 0.076$ and $\alpha_d = -0.11$; additionally, a high energy flux always dominates the soft flux. This outburst never reaches HSS, and this is classified as a failed outburst. But the 2011 outburst has $A = 0.086$, and it is a full outburst. Hence the 2008b and 2011 outbursts offer an excellent opportunity to constrain the critical accretion rate $0.076 < \dot{m}_{dc} < 0.086$ of the system. Using the estimated mass and critical accretion rate, we have commented on the orbital parameters of the system. Also, we have calculated the rise time of the outburst for this system as $t_r \sim 25$ days, which is the rise time of the 2003 outburst, whereas other outbursts have an approximate 10-day rise time. This indicates that the strong irradiation phase of the 2003 outburst may have pushed the pileup radius. All of the outbursts from 2008 onwards have a similar rise time, duration, and recurrence period, which indicate the fixed location of the pileup radius with a regular mass supply from the secondary. We associate the three distinct peaks in the 2003 outburst

lightcurve to be due to the triggering of the outburst, irradiation of the cold outer disc, and irradiation of the secondary, respectively.

We have discussed the issues related to modelling the 2003 outburst using the two-component model in Section 4.5. We plot the powerlaw versus the blackbody contribution (Figure 4.13) required to model the data. It was difficult to model the spectra in regions III and IV by an accretion disc alone due to the presence of large non-thermal components even in SIMS/HSS state. We have argued that region (II) needs a modification of effective disc temperature by colour temperature, and region IV needs an additional non-thermal contribution, whereas region III needs both of the modifications. As an example, we fitted the observation with the highest flux (in SIMS) in the 2003 outburst with these modifications, which are presented in Figure 4.14. We have shown that the additional non-thermal component requires fitting data, which can be produced from the base of the jet with reasonable parameters. Also, the non-thermal X-ray flux is consistent with the radio flux observed after this observation. So, a dynamical model coupling the disc-jet is required to fit the 2003 outburst data, which we aim to attempt in the future. Finally, we could connect the evolution of accretion dynamics with the jet launching by using radio observations in 2009 with the X-ray data. In Figure 4.15, we see steady jet and radio emission at the beginning and end of the outburst due to the high contribution of $\dot{m}_h$ and the absence (or very small contribution) of jet in the HSS due to the cooling of PSR by the high rate of accretion of Keplerian matter.

Chapter 5

Study of Long Term Evolution of Accretion Dynamics of GX 339-4

We study the dynamical behaviour of the galactic black hole source GX 339-4 during 2002-2011 outbursts using RXTE, Swift/XRT, XMM-Newton/pn archival data. We have performed spectral modelling of all the available outburst data and try to understand the spectral evolution as well as the dynamical evolution of accretion disc parameters of the source. We discuss the similarities/differences between outbursts and propose a possible physical picture to unify the outbursts. A generic toy model has been proposed to understand the evolution of accretion parameters for sources like GX 339-4 having a long rise time. This chapter is based on our published work (Aneesha et al., 2019).

5.1 About the Source GX 339-4 and Related Studies

The source GX 339-4 was discovered in 1973 by satellite OSO-7 (Markert et al., 1973). The absorption lines in NIR (Heida et al., 2017) reveals a giant K-type companion and this confirms the earlier finding (Hynes et al., 2004; Muñoz-Darias et al., 2008). The distance to GX 339-4 is found to be $6\,\mathrm{kpc} \leq d \leq 15\,\mathrm{kpc}$ (Hynes et al., 2004) from studies based on Na D lines whereas Zdziarski et al. (2004) has estimated $d \gtrapprox 7\,\mathrm{kpc}$ from optical and infrared observations. Also, Parker et al. (2016) have fitted the X-ray spectra with $d = 8.4 \pm 0.9\,\mathrm{kpc}$. Since the system did not show any eclipse in X-ray or optical data, Cowley et al. (2002) restricted the upper limit of the inclination angle $i \leq 60^\circ$ and Zdziarski et al. (2004) suggested a lower limit of $i \geq 45^\circ$ from the secondary mass function estimation. From the reflection modelling of X-ray spectra Fürst et al. (2015); García et al. (2015) have found inclination angle in the range $40^\circ - 60^\circ$ and Parker et al. (2016) have estimated $i = 30^\circ \pm 1^\circ$. Whereas Heida et al. (2017) have quoted $37^\circ < i < 78^\circ$ from the NIR absorption lines of

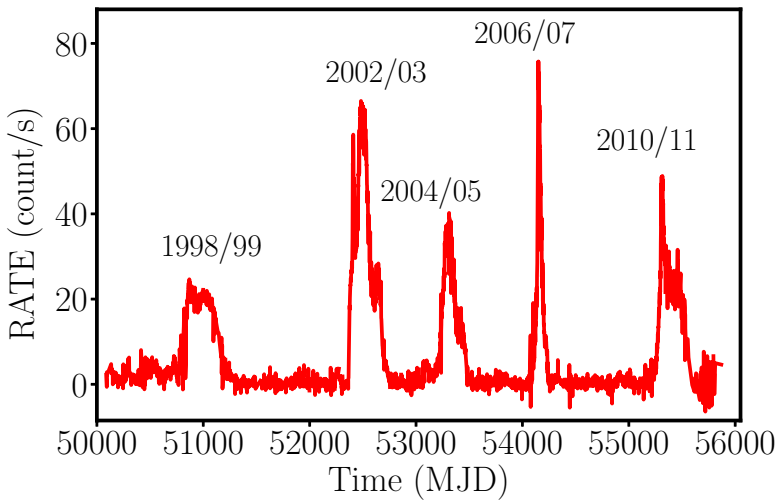

Figure 5.1: RXTE/ASM (2-10 keV) one day average lightcurve of GX 339-4 over the period 1998-2011.

the donor star. The optical spectroscopy of Bowenblend and HeII provide a mass function of the system to be $f(M) = 5.8 \pm 0.5\,\mathrm{M}_{\odot}$ with a binary period of 1.7557 days (Hynes et al., 2003). Parker et al. (2016) have constrained the mass to be $9.0^{+1.6}_{-1.2}$ $\mathrm{M}_{\odot}$ whereas Heida et al. (2017) have quoted $2.3\,\mathrm{M}_{\odot} < \mathrm{M} < 9.5\,\mathrm{M}_{\odot}$. Recently, Sreehari et al. (2019) have estimated the mass of the source in the range $8.28-11.89\,\mathrm{M}_{\odot}$ from spectral modelling using two-component flow, evolution of QPO frequency and saturation of spectral index. Modelling the reflection component of the X-ray spectra, spin of the system is found to be $a = 0.93 \pm 0.01$ (Miller et al., 2008) whereas Ludlam et al. (2015) have estimated $a > 0.97$ and Parker et al. (2016) have determined $a = 0.95^{+0.02}_{-0.08}$ using relxill model for reflection fitting.

Over past four decades, the source has shown many successful outbursts as well as many failed outbursts where the source always remain in the LHS during outburst. The outbursts profile of the source during RXTE era is shown in Figure 5.1. There are several early reports of state transitions (Méndez & van der Klis, 1997; Belloni et al., 1999) and time variability (Maejima et al., 1984; Miyamoto et al., 1991; Nowak, 2000) of the source. Detailed timing and spectral studies (Belloni et al., 2005; Debnath et al., 2010; Nandi et al., 2012) show a complete evolution of spectral state during outburst. Several attempts have been made to understand the spectral behaviour of the source using physically motivated models. Corbel et al. (2003), Connors et al. (2019) used synchrotron emission from the jet and the inverse Comptonization of both the thermal disc photons as well as synchrotron photons to explain radio, IR and X-ray emissions in GX 339-4. Zdziarski et al. (2004) has

Table 5.1: RXTE observation summary

Outburst	Start date (MJD)	Stop date (MJD)	Duration (day)
2003/04	02-04-2002 (52366)	27-04-2003 (52756)	389
2004/05	13-05-2004 (53138)	20-04-2005 (53480)	343
2006/07	14-11-2006 (54053)	05-06-2007 (54256)	204
2010/11	12-01-2010 (55208)	28-02-2011 (55620)	412

developed an accretion flow model comprises of a cold optically thick outer disc and a hot inner optically thin disc. The RXTE-ASM data during 1998/99 and 2002/03 outburst of GX 339-4 is studied with this model. Marcel et al. (2018) have used a unified accretion-ejection model to understand the X-ray and Radio emissions of 2010/11 outburst of GX 339-4. But none of these models address the dynamics of the system self-consistently i.e., given the flow parameters like, accretion rate, angular momentum etc, the flow hydrodynamics should decide the rest. Also sometimes models are not fully self-consistent. For example, in unified accretion-ejection model (Marcel et al., 2018), the transition radius between accretion disc and central corona is a parameter and it is independent of the accretion rate which may not be physically correct. Also if the hot central corona is created from the accretion disc, it would not be able to explain the soft time lag (Smith et al., 2001, 2002a, 2007). Also, not much attention has been paid to understand the accretion dynamics quantitatively by physically modelling the observed spectrum or outburst profiles.

5.2 Observations

During the life span of RXTE (1995 to 2012), it has observed GX 339-4 to undergo outbursts quite frequently. Since RXTE did not have the full coverage of 1998/99 outburst, we did not consider this outburst in our study. The four outbursts considered in our study are 2002/03, 2004/05, 2006/07 and 2010/11. We have analysed a total of 129 observations span over 389 days in 2002-03, 115 observations over 343 days in 2004-05, 139 observations ranging over 204 days in 2006-07 and 288 observations during 412 days in 2010-11 from RXTE archive (see Table 5.1 for details). Also, we look for simultaneous observations with other X-ray instruments. We find simultaneous RXTE and Swift/XRT observations for 2006/07 (10 observations) and 2010/11 (18 observations) outbursts which are listed in Table A1. Also, there are four XMM-Newton observations simultaneous with the RXTE observations for 2002/03 outburst. But MOS data are highly piled up and we could not get any useful results from two observations on 24-08-2002 and 19-09-2002. Therefore, we list two XMM-Newton/pn observations in Table A1.

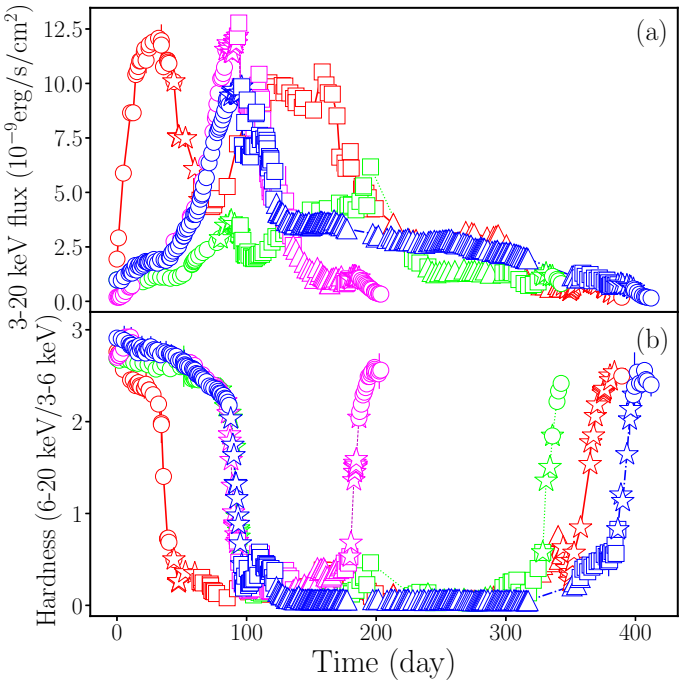

Figure 5.2: (a) 3.0-20.0 keV PCA light curves and (b) hardness ratio (6.0-20.0 keV flux / 3.0-6.0 keV flux) as a function of time of all outbursts of GX 339-4 during 2002-2011 period are plotted. The lines with different colours (red-solid: 2002/03; green-dot: 2004/05; magenta-dash: 2006/07 and blue-dash dot: 2010/2011) represent individual outbursts. The different symbols: circles mark LHS; star marks HIMS; squares mark SIMS and triangles mark HSS.

5.3 Outburst Profile and HID

We have analysed all the RXTE/PCA data available in RXTE era. The data reduction method is summarized in §3.2.1. We consider RXTE/PCA spectrum in the energy range 3.0 - 45.0 keV without any grouping or binning. A systematic error of 0.5% is added to the spectrum in 2006/07 and 2010/11 outbursts considering the uncertainties in the instrumental calibration. We have used a combination of phenomenological models consisting of an absorption component (`phabs`) with a `powerlaw` and/or a multi-colour disc blackbody (`diskbb`), whenever required. Occasionally an emission line represented by `gauss` in energy range (6-7) keV, a smeared absorption edge (`smedge`) (Ebisawa et al., 1994) and high energy cutoff (`highecut`) are required to fit the data. We have used photoelectric absorption cross sections from Verner et al. (1996) and elemental abundance Wilms et al. (2000) for the absorption model. The χ^2 statistic is used for model fitting. In the spectral modelling of all the data set, the best fit model have reduced χ^2 between 0.8 to 1.3 and the uncertainities are calculated within 90% confidence limit using `migrad` method. Includ-

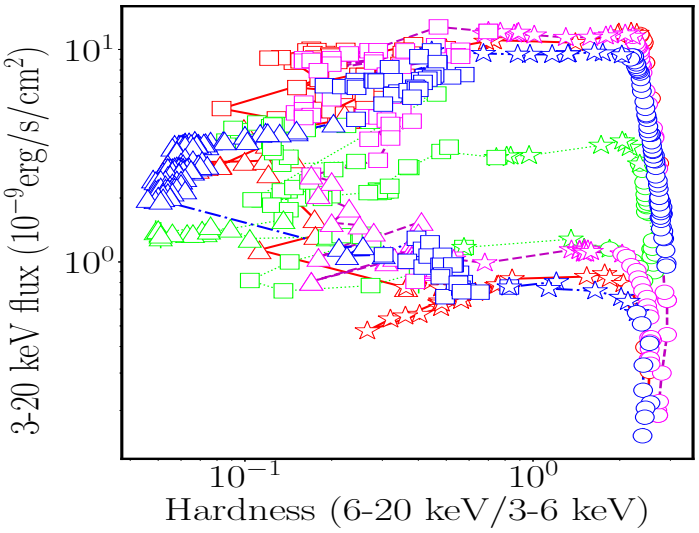

Figure 5.3: PCA HID of all outbursts of GX 339-4 during 2002-2011 period. The lines of different colours/styles and symbols follow the same meaning as in Figure 5.2.

ing all the spectral fitting, the `smedge` width varies between 1 to 30keV and the `smedge` maximum absorption factor varies between 0.1 to 7 whereas the gaussian line width varies between 0.6 to 1.0.

We have calculated the flux in 3.0-20.0 keV energy band to generate the light curve. Also, we have separately estimated the flux in 3.0-6.0 keV and 6.0-20.0 keV energy band and the hardness is defined as the ratio of fluxes in 6.0-20.0 keV and 3.0-6.0 keV. The lightcurves of different outbursts and the corresponding hardness evolution are shown in the top (a) and bottom (b) panels of Figure 5.2 respectively. Here, time of evolution is expressed in day and day zero of individual outbursts in MJD are given in Table 5.1. The general evolution of outbursts can understand from HID which have been plotted in Figure 5.3. Here and rest of this work, we have used lines with different colours (red-solid: 2002/03; green-dot: 2004/05; magenta-dash: 2006/07 and blue-dash dot: 2010/2011) to represent individual outbursts. We follow Belloni et al. (2005); Motta et al. (2011, 2009); Stiele et al. (2011); Nandi et al. (2012) for spectral classifications and different symbols (circles mark LHS; stars mark HIMS; squares mark SIMS and triangles mark HSS) are used to represent the spectral states.

Generally, in the rising phase of the outburst the flux increases gradually with very small variation in hardness in the low hard state and suffers a sudden drop in hardness in HIMS. The flux reaches maximum value in SIMS where the spectrum becomes softer. The source continues to evolve with low hardness and a decreasing trend of flux in HSS until it

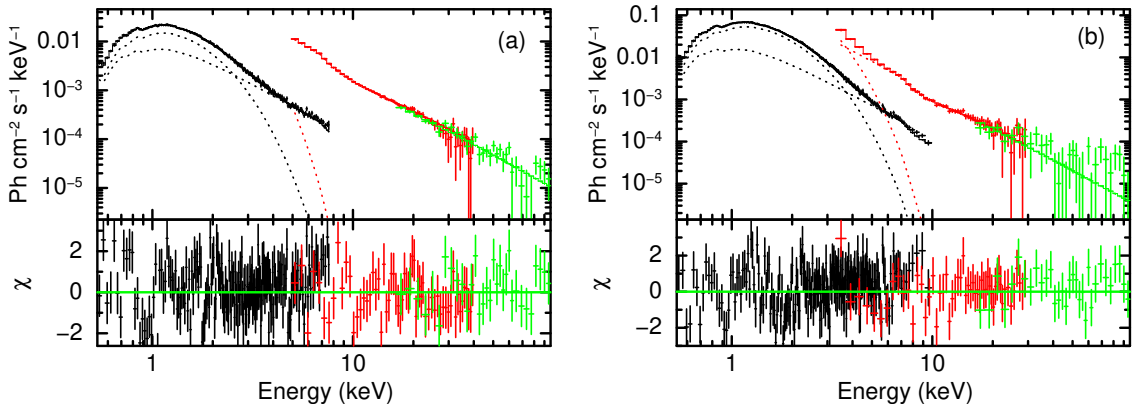

Figure 5.4: Broadband spectral modeling of XMM-Newton/pn (black), PCA (red) and HEXTE (green) observations on (a) 08-03-2003 and (b) 20-03-2003 by `phabs×smedge(diskbb+powerlaw)×constant` model with $\chi^2/dof = 1071.56/1000$ and $\chi^2/dof = 1114.67/1066$ respectively. The XMM-Newton/pn spectrum are binned by a factor of 5 for better clarity.

reaches HIMS in decline phase. The hardness evolution shows a very similar trend for all these outbursts even though the duration of outbursts and flux levels are quite different. The hysteresis nature of the HID is ensured by the hard-soft transition at high flux level in the rising phase whereas a soft-hard transition at low flux level in the decline phase. All HIDs (Figure 5.3) have very similar characteristics except 2004/05 outburst being low luminous.

5.4 Broadband Spectral Modelling : Phenomenology

We find simultaneous observations of XMM-Newton and Swift with RXTE during these outbursts. These observations are not strictly simultaneous but still we could generate broadband spectra as the source did not show significant change in count rate as well as hardness during the period of observations. The details of these observations are given in Table A1 and the data reduction procedure of these instruments are summerised in §3.2. The simultaneous broadband spectra (0.3 - 100.0 keV) are modeled using a `powerlaw` and a multi-colour disc blackbody (`diskbb`). Also, additional components like emission line (`gauss`) in energy range (6-7) keV, smeared absorption edge (`smedge`) (Ebisawa et al., 1994) are occasionally used to fit the data. The broadband spectra are required to constrain the blackbody component (particularly in LHS) and a better estimation of powerlaw component as well. The interstellar absorption n_H is frozen at $5 \times 10^{21}\,\mathrm{cm}^{-2}$ (Ilovaisky et al., 1986; Méndez & van der Klis, 1997; Kong et al., 2000). Otherwise n_H varies between $(4-7) \times 10^{21}\,\mathrm{cm}^{-2}$ for broadband spectra using XRT, PCA and HEXTE.

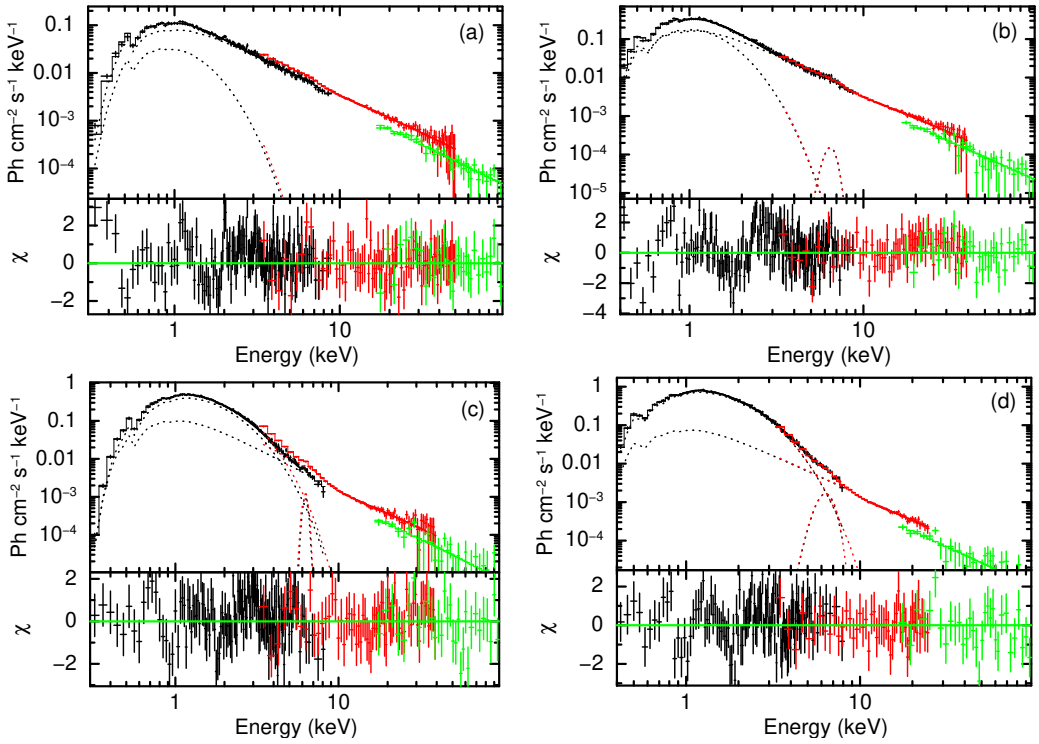

Figure 5.5: Broadband spectral fitting of Swift/XRT (black), PCA (red) and HEXTE (green) data in (a) LHS (MJD 54240.884), (b) HIMS (MJD 54237.331), (c) SIMS (MJD 54231.913) and (d) HSS (MJD 54213.031) during 2006/07 outburst. The spectra are fitted with `phabs×smedge(diskbb+ga+po)×constant` model whereas Gaussian component is not required for (a). The fitting statistics χ^2/dof are $549.80/604$, $536.81/583$, $523.86/534$ and $729.44/679$ respectively. The Swift/XRT spectrum is binned by a factor of 4 for better clarity.

We could find only two simultaneous observations of XMM-Newton/pn along with RXTE for 2002/03 outburst and the broadband spectra are presented in Figure 5.4. Both observations are in the HIMS state during the decline phase of the outburst. Here black, red and green colours represent the XMM-Newton, PCA and HEXTE data respectively along with unfolded models of `diskbb` and `powerlaw`. No simultaneous observation exists for 2004/05 outburst. Simultaneous observations of Swift/XRT and RXTE exist during 2006/07 decline phase and rising phase of 2010/11 outbursts. We have fitted all of them but for representation, we show only one spectrum from each spectral state (a) LHS; (b) HIMS; (c) SIMS; (d) HSS for both the outbursts in Figure 5.5 and Figure 5.6 respectively. In both figures, black, red and green colour represent XRT, PCA and HEXTE data respectively along with unfolded models.

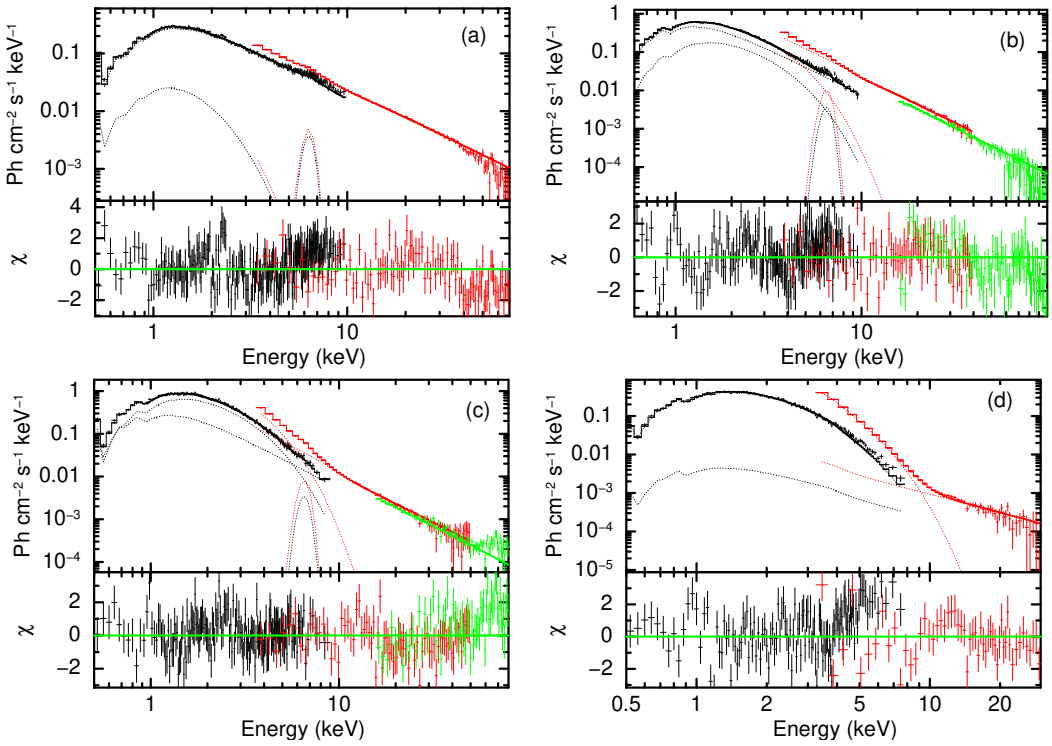

Figure 5.6: Broadband spectral modeling of Swift/XRT (black), PCA (red) and HEXTE (green) data in (a) LHS (MJD 55281.744), (b) HIMS (MJD 55302.411), (c) SIMS (MJD 55316.986) and (d) HSS (MJD 55334.061) during 2010/11 outburst. The model `phabs×edge×smedge(diskbb+gaussian+po)×constant` are used to fit the data whereas gaussian is not required for (d). The corresponding statistics for spectral modelling are χ^2/dof = 854.68/819, 857.36/803, 727.25/690 and 643.92/530 respectively. The Swift/XRT Spectrum is binned by a factor of 4 for better clarity.

5.4.1 Evolution of Spectral Parameters

We study the time evolution of spectral fitting parameters using PCA data as well as simultaneous observations (Table A1). The evolution of inner disc temperature T_{in} of `diskbb` model for (a) 2002/03, (b) 2004/05, (c) 2006/07 and (d) 2010/11 outbursts are plotted in Figure 5.7. The parameters from PCA data only are shown in green-solid symbols whereas the same from pn-PCA-HEXTE broadband spectra of 2002/03 outburst are shown in blue-dot symbols. Parameters from XRT-PCA-HEXTE spectra for 2006/07 and 2010/11 outbursts are presented by red-dash symbols. We have used the same symbols for spectral classes as in Figure 5.2. The uncertainities (marked inside the symbols) are within 90% confidence range. In the LHS, fitting only PCA data require unusually high disc temperature $T_{in} \geq 2keV$ (Plant et al., 2014) and hence only PCA data cannot constrain T_{in} in LHS. In fact, we fit the LHS PCA data with `powerlaw`, `smedge`. Simultaneous observations

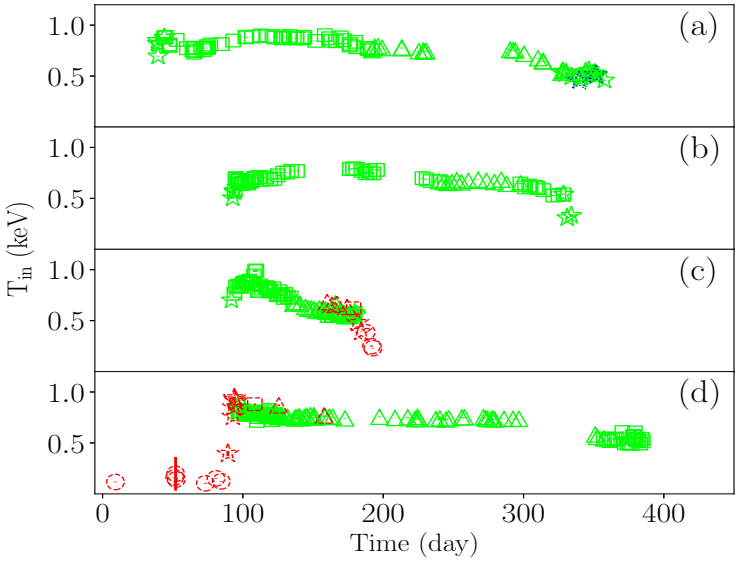

Figure 5.7: Evolution of inner accretion disc temperature (T_{in}) of the source for (a) 2002/03 (b) 2004/05 (c) 2006/07 and (d) 2010/11 outbursts spectral fitting. The green-solid symbols represent only PCA data, blue-dot symbols are for simultaneous XMM-Newton-PCA-HEXTE data and red-dash symbols mark simultaneous XRT-PCA-HEXTE data. The different symbols: circles mark LHS; star marks HIMS; squares mark SIMS and triangles mark HSS. The uncertainities (marked inside the symbols) are within 90% confidence range.

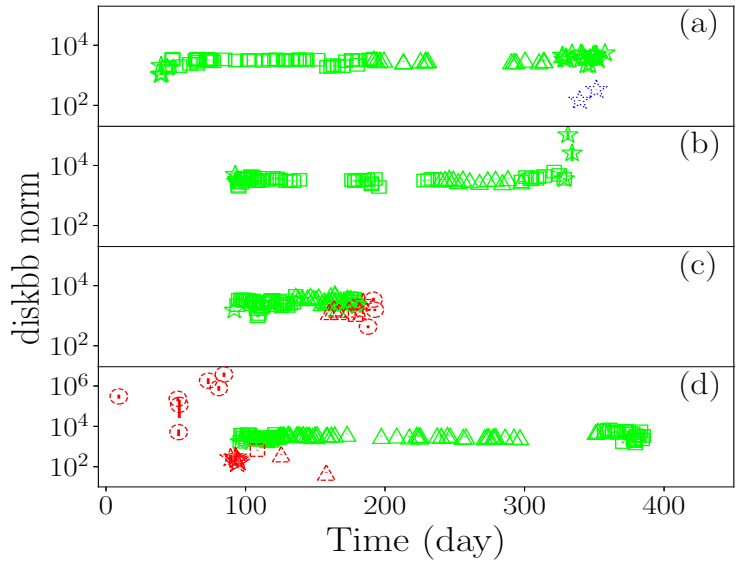

Figure 5.8: Evolution of `diskbb` normalizations for (a) 2002/03 (b) 2004/05 (c) 2006/07 and (d) 2010/11 outbursts. The different colours and symbols have same meaning as in Figure 5.7. The uncertainities (marked inside symbols) are within 90% confidence range.

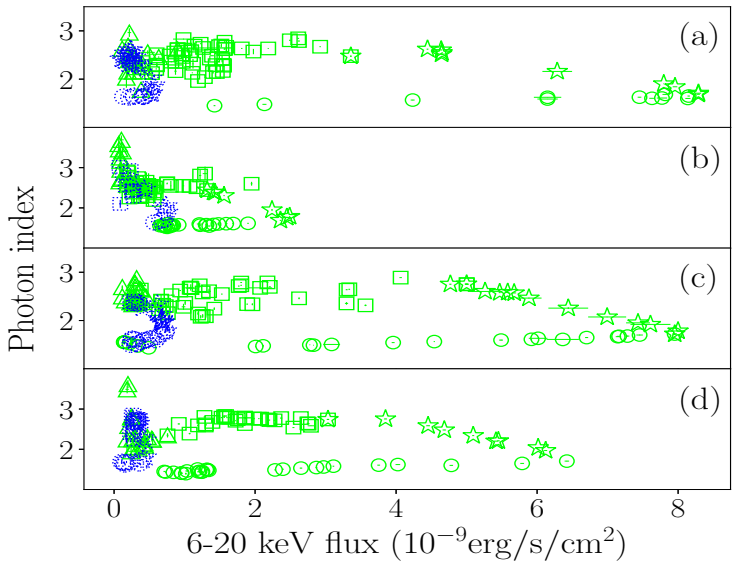

Figure 5.9: Photon index vs 6.0-20.0 keV flux for (a) 2002/03 (b) 2004/05 (c) 2006/07 and (d) 2010/11 outbursts. The different symbols have same meaning as in Figure 5.7. The green-solid symbols represent the rising phase and blue-dot symbols denote the decline phase of the outbursts. The uncertainities are within 90% confidence range.

with XRT-PCA (red-dash points in Figure 5.7c and Figure 5.7d) could able to estimate T_{in} in LHS. Whereas the simultaneous fitting with PN-PCA data in 2002/03 (blue-dot points in Figure 5.7a) are in HIMS and show similar T_{in} as in PCA. This figure shows that in the starting and ending part of the outburst, there may be a small contribution of photons from the accretion disc and hence one expects a low T_{in}. As the source approaches to rising-intermediate state, the disc moves inward and T_{in} increase. It remains almost constant in SIMS to HSS and towards the end of declining phase disc starts disappearing with a decreasing T_{in}. Also, 2006/07 outburst shows a faster evolution of T_{in} in compared with other outbursts. The evolution of diskbb normalizations are shown in Figure 5.8. The broadband fitting (red-dash points in Figure 5.8) show that disc norm start with a high value in LHS as the disc is far apart and decreases towards intermediate states.

The variation of photon index (Γ_p) with the hard flux (6.0-20.0 keV) is presented in Figure 5.9. Here, green-solid symbol represents the rising phase whereas blue-dotted symbol denotes the decline phase of the outbursts. All the outbursts show a hysteresis (anti-clock wise) with almost constant photon index (~ 1.5) in the rising LHS. The value of photon index increases ($2 < \Gamma_p < 3$) with a decrease of hard flux as the source moves towards softer states. In the decline part of the outburst photon index decreases and the 6.0-20.0 keV flux does not show much variation. Zdziarski et al. (2004), showed a similar behaviour between

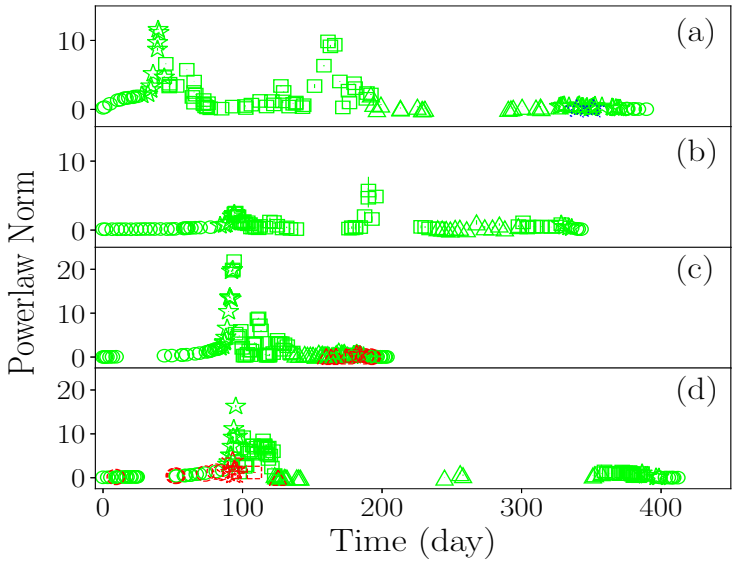

Figure 5.10: Evolution of powerlaw normalizations for (a) 2002/03 (b) 2004/05 (c) 2006/07 and (d) 2010/11 outbursts. The different colours and symbols have same meaning as in Figure 5.7. The uncertainities are within 90% confidence range.

photon index and flux in different energy range for the same source. Whereas García et al. (2015), found nearly constant photon index in hard state of different outburst of GX 339-4 with very different luminosities. The Figure 5.10 represents evolution of powerlaw normalization and it shows that the powerlaw normalisation sharply increases towards HIMS of the rising phase where powerlaw dominates the spectra and after that almost remain at constant low values in the softer states. In all outbursts, we see a hard flare in SIMS (parameter t_{6-20} in Table 5.3) indicated by a sudden rise of powerlaw normalization. We find that a powerlaw component is always required to model data over the entire outburst whereas in 2010/11 outburst (Figure 5.10d) the spectral modeling in HSS can be done using `diskbb` only.

Past several studies suggested that Fe line flux can be used as a tracer of Compton reflection signature. The process of bound-free absorption in the reflecting medium is followed by emission of a fluorescent Fe Kα line. The equivalent width of the Fe Kα line is a measure of the extend of reflection. Petrucci et al. (2001) discussed how Comptonization process affects the measurement of the equivalent width of Fe line and showed that the unscattered equivalent width of Fe line is anti-correlated with the corona temperature. In the same sense, Zdziarski et al. (2003) found Compton reflection strength is correlated with photon index for many outbursting sources and is strongest in the soft state whereas Gilfanov & Merloni (2014) showed a correlation between photon index and

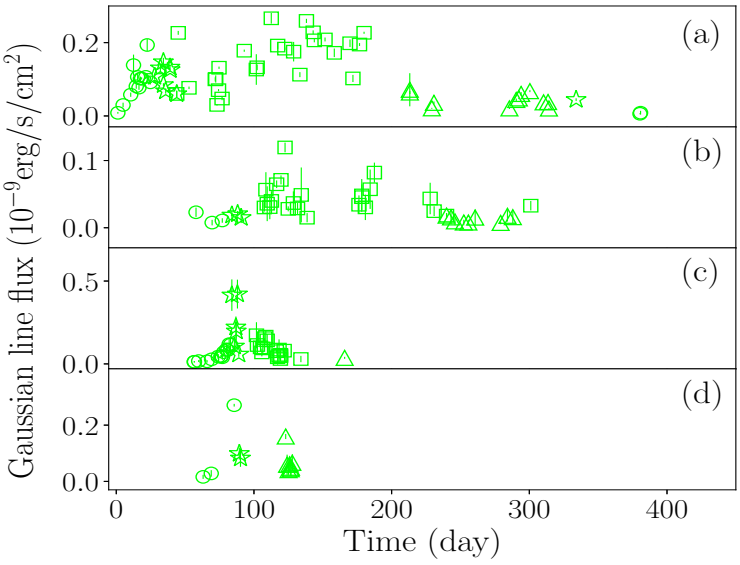

Figure 5.11: Evolution of gaussian line flux during (a) 2002/03 (b) 2004/05 (c) 2006/07 and (d) 2010/11 outbursts. We follow the same representations as in Figure 5.7. The uncertainities are within 90% confidence range.

the relative strength of the Comptonized radiation. Steiner et al. (2016) presented strong anti-correlation between Fe line equivalent width with powerlaw normalization. We have used Fe line represented by `gauss` to fit the data whenever required. In Figure 5.11, we have plotted the evolution of Gaussian line flux and it shows a very interesting trend. We observe that the Compton reflection signature is week in LHS and has an increasing trend of reflection strength towards softer states. Finally, becomes strongest in the SIMS for all outbursts except 2010 outburst. Also, if the existence of Fe Kα line is a signature of reflection, we observe a decreasing trend of reflection signature required to model the successive outbursts after 2002. To strengthen this findings, in Figure 5.12, we have plotted the evolution Gaussian line normalization over time with its uncertainty. We hardly could see the presence of Gaussian line in LHS except 2002/03 outburst. In LHS, we could able to fit the data reasonably well with reduced χ^2 in the range 0.8-1.1. Also, we see from Figure 5.12 that in 2002/03 outburst the minimum value of line normalization is as low as 10^{-4} and it increases in successive outbursts. For 2010/11 outburst the minimum normalization is above 10^{-3}. Possibly, this increasing trend of minimum normalization of Gaussian line is an indication of the degradation of PCA energy response over time. Though this decreasing trend of the requirement of Gaussian line may be due to the physical differences between the outbursts as well. In fact the reason that we observe outbursts of different durations, peak luminosities etc are the reflection of physical differences between outbursts. But in

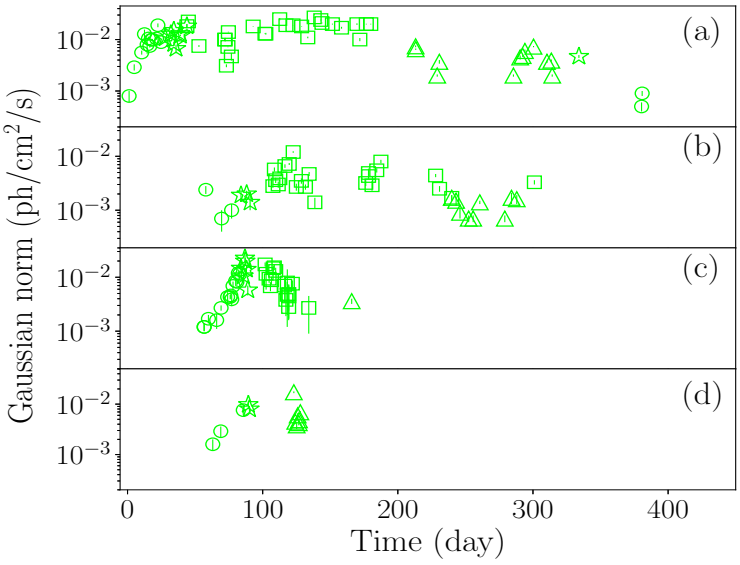

Figure 5.12: Evolution of normalisation of gaussian line during (a) 2002/03 (b) 2004/05 (c) 2006/07 and (d) 2010/11 outbursts. We have used the same symbols and colour references (Figure 5.7). The uncertainities are within 90% confidence range.

that case one should not expect any particular trend between outbursts.

5.5 Two-Component Spectral Modelling

In §5.4.1, we have studied the evolution of spectral parameters by fitting the data with phenomenological models where the spectral parameters are not directly connected to the hydrodynamics and radiation processes of the system. Hence, it is not possible to understand the behaviour of dynamical parameters from phenomenological spectral parameters. We intend to study the evolution of the dynamical parameters by fitting the spectral data two-component accretion flow model. We fit all the PCA data during 2002-2011. Here we assume the mass of the source as $9 M_{\odot}$ (Parker et al., 2016) and we have fixed $n_H = 5 \times 10^{21}\,\mathrm{cm}^{-2}$ (Ilovaisky et al., 1986; Méndez & van der Klis, 1997; Kong et al., 2000) for the entire spectral modeling. Also we see occasional requirement of additional components like `gauss` and `smedge` along with two-component model as those physics are yet to be included into the model. We have used photoelectric absorption cross sections (Verner et al., 1996) and elemental abundance (Wilms et al., 2000) for absorption model. We have used chi-square statistic to represent the goodness of fit. We have modelled all the four outbursts data and the best fit reduced χ^2 varies between 0.8 to 1.3. The uncertainities are calculated within 90% confidence range using method `migrad`. We

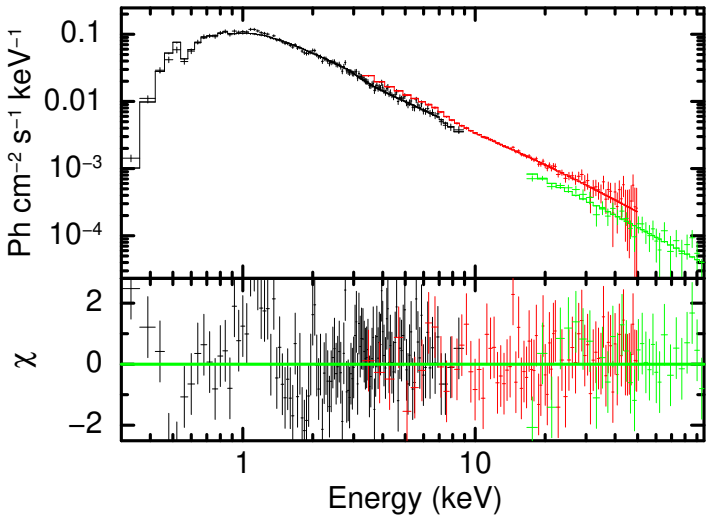

Figure 5.13: A representation of broadband spectral fitting of Swift/XRT (black), PCA (red) and HEXTE (green) data in LHS (MJD 54240.884) using two-component model with additional `smedge` component. The XRT/Swift spectrum is binned by a factor of 4 for better clarity. The statistics of the fitting is $\chi^2/dof = 574.18/601$.

find that the smearing width varies between 2-25 keV, the `smedge` maximum absorption factor varies between 0.1 to 5 whereas the gaussian line width varies between 0.4 to 1.0. As a representation, in Figure 5.13 we have shown the broadband spectral fitting of Swift/XRT (black), PCA (red) and HEXTE (green) data in LHS (MJD 54240.884) using two-component model with additional `smedge` component. The two-component model parameters are $\dot{m}_h = 0.016 \pm 0.002$, $\dot{m}_d = 0.009 \pm 0.002$, $x_s = 68 \pm 5.6$ with $\chi^2/dof = 574.28/601$.

5.5.1 Connecting Spectral States with Accretion Parameters

We estimate the accretion parameters $(x_s, \dot{m}_h, \dot{m}_d)$ from spectral fitting of individual observation and the time evolution of the same are presented in Figure 5.14, Figure 5.15 and Figure 5.16 respectively. Here red points are parameters values from spectral modeling of individual data set using two-component flow. The day zero of each outburst corresponds to MJD given in Table 5.1 and panels (a, b, c and d) represent the 2002/03, 2004/05, 2006/07 and 2010/11 outburst respectively. The general behaviour of parameters ($x_s, \dot{m}_h$ and $\dot{m}_d$) are very similar (except $\dot{m}_h$ in Figure 5.15a,b and is discussed in §5.5.2) in all four outbursts and we can understand the spectral evolutions by the relative values of these parameters.

At the beginning of the outburst $\dot{m}_h$ is high (Figure 5.15) and the shock location (Figure 5.14) is far away from the central object. Hence, PSR contains a large number of high

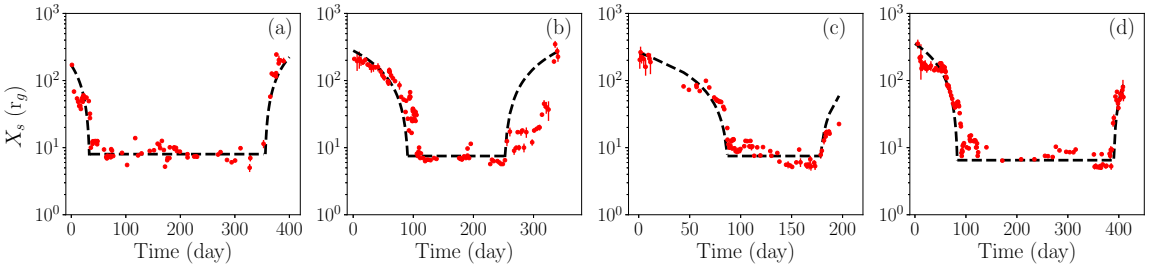

Figure 5.14: Evolution of shock location (red points) for (a) 2002/03, (b) 2004/05, (c) 2006/07 and (d) 2010/11 outbursts. The black dashed line represents the fitting of the general behaviour of x_s using Equation (4.3).

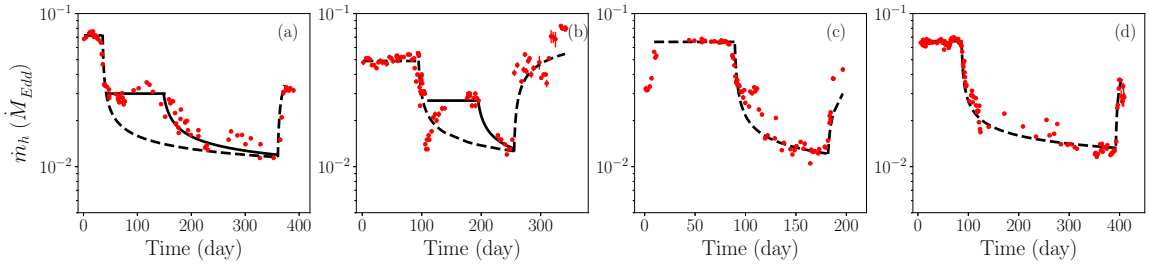

Figure 5.15: Evolution of sub-Keplerian halo rates (red points) for (a) 2002/03, (b) 2004/05, (c) 2006/07 and (d) 2010/11 outbursts. The black dashed line represents the fitting of the general behaviour of $\dot{m}_h$ using Equation (5.2). The solid lines in (a) and (b) appear to be a second triggering of outburst (see 5.6 for details).

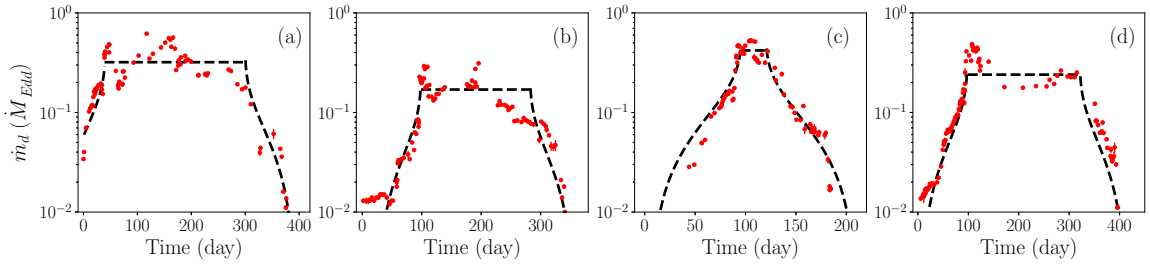

Figure 5.16: Evolution of Keplerian disc rates (red points) for (a) 2002/03, (b) 2004/05, (c) 2006/07 and (d) 2010/11 outbursts. The black dashed line represents the fitting of the general behaviour of $\dot{m}_d$ using Equation (5.1).

energy electrons but does not have sufficient soft photons to cool the PSR as the Keplerian disc rate (Figure 5.16) is very low. Hence, the source is in LHS. As the source proceeds towards the peak of the rising phase, x_s moves inward, $\dot{m}_h$ starts decreasing sharply (indicates no more fresh matter supply at the outer edge), $\dot{m}_d$ increases. This enhances the supply of soft photons and PSR becomes smaller and the source makes a transition to intermediate states. This increases the overall luminosity. The shock location remains closer to the central object, almost at constant value, during SIMS to HSS and $\dot{m}_h$ keep on decreasing whereas $\dot{m}_d$ remains around a constant high value. In HSS state, $\dot{m}_d$ starts decreasing and $\dot{m}_h$ has a very low value which makes hardness to a lower value. At the end shock location starts moving outwards, $\dot{m}_h$ starts increasing again, $\dot{m}_d$ continue to decrease to a low value and the source moves back to hard state in the declining phase. This explains the hysteresis behaviour of HID (Figure 5.3) as well.

5.5.2 Modelling Evolution of Accretion Parameters

The general behaviour of the evolution of accretion parameters (Figure 5.14, Figure 5.15 and Figure 5.16) can be understood using a toy model. We define four time scales (as in §4.4.2): t_r represents the rising time of the soft flux (related to $\dot{m}_d$), t_h is the rising time of hard flux (related to m_h), t_d is the time scale after which $\dot{m}_d$ starts decreasing in the decline phase and t_s is the time scale that both $\dot{m}_h$ and x_s begin to increase in the decline phase of the outburst.

We assume the time evolution of the Keplerian accretion rate as,

$$\dot{m}_d = \begin{cases} A - \alpha_d \, log(t_r - t), & t < t_r \\ A, & t_r < t < t_d \\ A - \alpha_d \, log(t - t_d), & t > t_d \end{cases} \tag{5.1}$$

here A is the highest average value of the Keplerian rate in unit of Eddington rate, t is time in days and α_d is a free parameter defines the steepness of the evolution.

The sub-Keplerian accretion rate can be modeled as,

$$\dot{m}_h = \begin{cases} B, & t < t_h \\ \dfrac{B}{\beta} \times \dfrac{1}{log(t - t_h)}, & t_h < t < t_s \\ \dfrac{B}{\beta} \times log(t - t_s), & t > t_s \end{cases} \tag{5.2}$$

Table 5.2: Model parameters for the evolution of $\dot{m}_d$, $\dot{m}_h$ and x_s

Outbursts	Time (day)				α_d	A	B	β	X_{s_0}	X_{s_i}	v_0
	t_r	t_h	t_d	t_s					(r_g)	(r_g)	(r_g/day)
2002/03	41.0	33.0	299.6	357.0	1.63	0.32	0.072	2.4	169	8.0	4.89
2004/05	99.0	91.0	282.0	252.5	0.91	0.17	0.049	1.75	279	7.5	3.00
2006/07	96.0	87.0	120.0	178.6	2.15	0.42	0.065	2.7	259	7.5	2.89
2010/11	98.0	83.0	321.0	390.1	1.22	0.24	0.066	2.0	355	6.5	4.20

where B is the maximum value of $\dot{m}_h$ in Eddington rate, β is a free parameter and t is time in days. We consider a linear variation of the shock location between X_{s_0} and X_{s_i} as given in Equation (4.3).

The data (red points) in Figure 5.14, Figure 5.15 and Figure 5.16 are fitted by Equation (4.3), Equation (5.2) and Equation (5.1) respectively without giving much attention on the local variations. The general fitted profiles are plotted by black dashed lines in Figures 5.14, 5.15, 5.16 respectively and the corresponding fitting parameters values are listed in Table 5.2.

The overall luminosity depends on the Keplerian accretion rate and 2006/07 outburst is the brightest with highest values of A. The maximum average values $\dot{m}_h$ (B) are very similar in all outburst though little lower for 2004/05 outburst whereas the same for $\dot{m}_d$ (A) are very different between outbursts. Hence, the viscous characteristics of the Keplerian disc is very different between outbursts and produce different peak luminosities. In fact, overall durations of outbursts are very different and it depends on the amount of time the source spends in SIMS and HSS. This in turn depends on the maximum Keplerian accretion rate and the efficiency of viscous dissipation converting it into radiation. Thus in 2006/07 outburst $\dot{m}_d$ has the highest value with maximum overall flux among all four outbursts and hence a shorter duration of outburst with short SIMS and HSS. This is possibly due to faster consumption of the Keplerian disc mass in comparison with other outbursts.

The value of α_d and β depend on how accretion rates need to be increased with time to fit the spectra. In the case of GX 339-4, they are found to be the same in both the rising and decay profile of the accretion rates. This is because the rise and decay duration of accretion rates are approximately the same in all the outbursts. But this may not be a general conclusion valid for all outbursts of similar types. Also, a larger value of β indicates a sharp rise and decline of $\dot{m}_h$ than $\dot{m}_d$. This is expected because β depends on the infall time scale (via radiative cooling time scale) whereas α_d depends on the viscous time scale. In general the shock may propagate in constant speed or accelerated motion due to the inverse Compton cooling of PSR by the soft photons from the Keplerian disc. Mondal & Chakrabarti

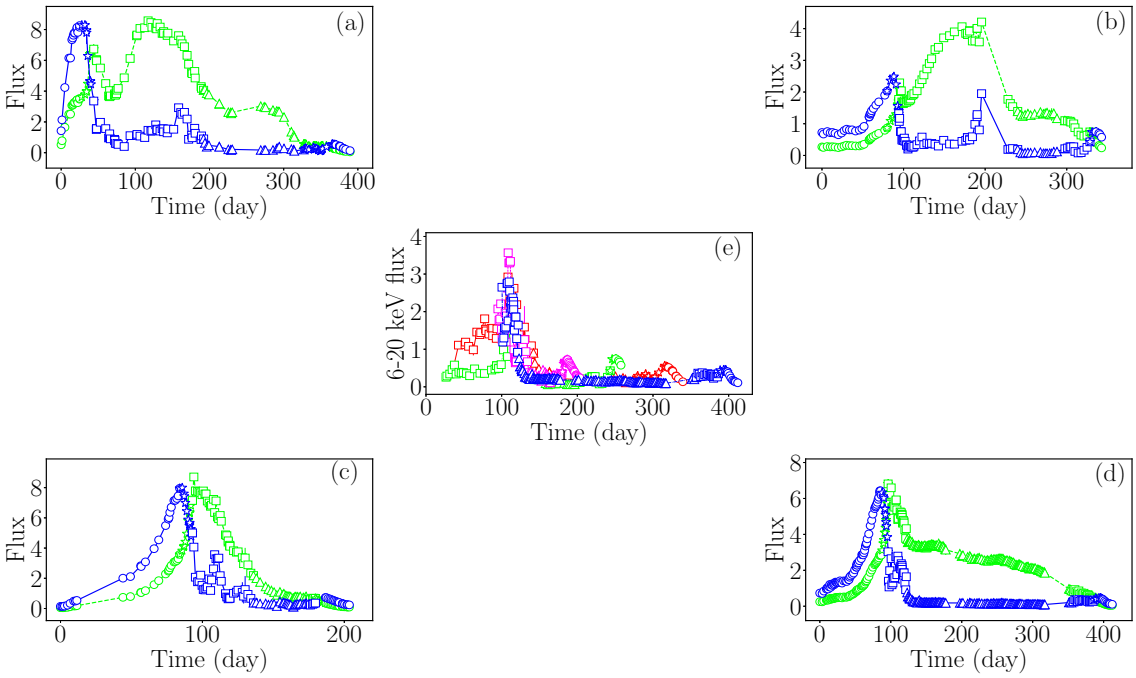

Figure 5.17: 3.0-6.0 keV (green-dash) and 6.0-20.0 keV (blue-solid) PCA light curves of GX 339-4 during (a) 2002/03, (b) 2004/05, (c) 2006/07 and (d) 2010/11 outburst respectively. The flux is expressed in the units of $10^{-9}\mathrm{erg/cm^2/s}$. The different symbols represent the following: circle marks LHS; star marks HIMS; square marks SIMS and triangle marks HSS. Panel (e) shows the evolution of 6.0-20.0 keV flux after 50 days for 2002 (red-solid) and 95 days for 2004 (green-dot) onward along with other two outbursts. Then the hard peak-I for 2006/07 and 2010/11 outbursts also should appear in the figure but it makes the figure very clumsy. Hence for presentation purpose, we have plotted 6.0-20.0 keV flux for 2006/07 (magenta-dash) and 2010/11 (blue-dash dot) outbursts after hard peak-I with time zero at the beginning of the outburst.

(2013) have calculated the amount of cooling of PSR due to inverse-Comptonization with the increase of Keplerian rate and have shown that shock moves inward with the increase of Keplerian rate. Hence, the shock travels at speed determined by the rate of change of $\dot{m}_d$ and a typical value is few r_g/day. Nandi et al. (2018) have shown that an accelerated motion of the shock is required to model the QPO evolution of 1999 outburst of XTE J1859+226. But from Table 5.2 we could see for GX 339-4 the shock front moves inward and outward with constant speed and are very similar between outbursts. Also, the constant value (v_0) of shock speed may differ during the rising and decay of outbursts.

The shock location in two component model is the truncation radius of the Keplerian disc. We find from the spectral modeling of all the outbursts data that the minimum value of the shock location is $\sim 5r_g$ in the soft state. Although it can be even lower depending on the position of the multiple sonic points of the flow. In general, one expects the trunca-

tion radius to move inwards due to the progress of the outburst, being close to the central object in the soft state and move apart in the decline phase. Hence, in the hard state, the truncation radius of the Keplerian disc is expected to be far from the BH. Although, García et al. (2015) indicated a huge disagreement of the inner edge radius from the reflection modelling of different observations data in the hard state of this source. This could be due to the inherent dependency of inclination angle in the reflection models to determine the truncation radius of the disc. Also, in LHS, the corona contribution is dominant and generally the reflection signature is weak. Hence, a proper continuum modeling of the data is required to constrain the reflection contribution. The continuum contributions from variety of corona models may differ significantly and may result different reflection contributions. Hence, the disc truncation radius calculated using reflection modeling may suffer some uncertainty due to corona models as well.

The rising phase of the outburst is controlled by two time scales (t_h and t_r). One expects $t_h < t_r$ (see Table 5.2), if two independent components of accreting matter regulate the hard and soft photons which are discussed in §5.5.2. To illustrate this, we separately plot the 3.0-6.0 keV (soft) and 6.0-20.0 keV (hard) light curves for all outbursts in Figure 5.17a,b,c,d, where the green line represents the soft flux and the blue line indicates the hard flux. We observe that the hard flux leading the soft flux by 8-12 days for all outbursts and the same have been found in many other sources (Smith et al., 2001, 2002a, 2007). The time scale t_d and t_s regulate the decline phase. We note that t_s represents beginning of HIMS in the decline phase whereas t_d is possibly associated with SIMS or HSS but does not have a very defined identification like other time scales. In general $t_d < t_s$ i.e., the Keplerian disc rate starts to decrease before shock location could move outward and the increase of halo rate to initiate the dimming of outburst. This is what we see from Table 5.2 for all outbursts except 2004/05 outburst. This could be the reason that Figure 5.15b shows deviation from the model trend in the decay phase. In this case the shock start to recede back in the soft state itself before the declination of the Keplerian accretion rate.

5.6 A Unified View of Outbursts with Irradiated DIM

One noticeable feature in the 3.0-20.0 keV light curves (Figure 5.2) is that 2002/03 and 2004/05 outbursts have two peaks whereas a second peak is not obvious in the other outbursts. But Figure 5.17a,b,c,d show that in all outbursts 6.0-20.0 keV light curves are having different peaks (I and II in order of their appearance with time) whereas 3.0-6.0 light curves of 2002/03 and 2004/05 outbursts only show two peaks. The properties of the

Table 5.3: Properties at peaks in light curves of different energy band

Outburst	Peak No	F_{3-6}	t_{3-6} (day)	F_{6-20}	t_{6-20} (day)
2002/03	Peak I	6.73	44	8.29	32
	Peak II	8.57	117	2.92	158
2004/05	Peak I	2.29	95	2.49	88
	Peak II	4.21	195	1.95	195
2006/07	Peak I	8.71	94	8.00	86
	Peak II	—	—	3.57	108
2010/11	Peak I	6.81	96	6.43	85
	Peak II	—	—	2.79	110

Note: F_{3-6} and F_{6-20} are fluxes in units of $10^{-9}\mathrm{erg/s/cm^2}$ in 3.0-6.0 keV and 6.0-20.0 keV respectively. Whereas t_{3-6} and t_{6-20} are the time since triggering that the lightcurves peak in these two energy band respectively.

light curves at peaks are summarized in Table 5.3.

Unlike other outbursts of this source during the RXTE era, 2002 outburst has shown a very extended quasi-steady activity with a second peak (peak-II). The 2002 outburst witnessed a four year long quiescence phase in comparison with the outburst in every couple of years. This means the Keplerian disc got enough time to rebuild and extended much inside (smaller X_{s_0} in Table 5.2). Along with this a shorter rising time ($\sim$ 40 days) and more symmetric rise-decay profile of the peak-I of 2002 outburst indicates that possibly the outburst did not trigger at the outer edge of the disc. The standard picture of irradiated DIM (van Paradijs & McClintock, 1994; Shahbaz & Kuulkers, 1998) suggests that it was rather triggered as an in-outward outburst which enhanced the mass accretion rate in Keplerian disc and the disc has moved close to the central object faster, reaching the flux at peak-I. The irradiation of the outer disc due to central X-ray source keeps the outer disc hot and sub-Keplerian rate decrease sharply (Figure 5.15a) due to enhanced viscosity at the outer edge. But after a few days, the sub-Keplerian rate halts to another constant value ~ 0.03 and $\dot{m}_h$ always remains constant during triggering of outburst. This indicates that the irradiation possibly affects the binary companion as well with an enhanced mass accretion at the outer part of the disc and hence sub-Keplerian rate does not decrease further. Considering that the second phase of mass transfer triggered after peak-I, the duration between the soft peak-II and hard peak-I is $\sim$ 85 days which is comparable to the rising time of other outbursts. This continued accretion onto the central object produces a quasi-steady flaring activity till it reaches peak-II. Unlike the normal outburst triggering in LHS, the second triggering has happened in SIMS with a much higher value of $\dot{m}_d$ and a lower value of $\dot{m}_h$. After soft peak-II, $\dot{m}_h$ finally starts to decline again and finally the outburst starts

dimming when almost the entire Keplerian disc mass is engulfed by the central BH. The 2004 outburst is different from 2002 outburst, having usual rise time ~ 90 days (Table 5.2) and faintest among all the outbursts. The 2004 outburst triggered at the outer edge of the disc and propagate as out-inwards due to the long rise time. The rest of the dynamics is very similar to 2002 outburst proposed above. The low luminosity of 2004 outburst is due to a lower Keplerian disc accretion rate (Figure 5.16b) than other outbursts and possibly this indicates a lower disc mass prior to the outburst. Thus the existence of the second soft peak where the overall flux has a maximum in both 2002/03 and 2004/05 outburst, can be thought of a combination of two successive triggering of outbursts i.e., a second triggering of outburst may have happened after peak-I. The second triggering of 2002/03 and 2004/05 outburst are represented by a solid black line in Figure 5.15a,b with the same parameters as in Table 5.2 but t_h =150 days and 200 days respectively.

Interestingly, King & Ritter (1998); Shahbaz et al. (1998), suggested the presence of secondary maxima after $\sim 10 - 15$ days of the overall peak in the outburst profile of BH XRBs due to irradiation in DIM. The thermal instability at the outer edge due to irradiation triggers small outburst, adding central accretion rate during decay phase. The 2006/07 and 2010/11 outbursts are more of classical irradiation DIM type with a hint of peak-II and here the sub-Keplerian matter continuously decrease (Figure 5.15c,d) after the peak flux. Recently, Tetarenko et al. (2018a,b) have done notable works to unify the lightcurve profiles and have quantitatively estimated the α-viscosity parameter for different XRBs by fitting the light curve with an irradiated accretion disc model. Though they did not apply their model for 2002 and 2004 outbursts of GX 339-4 where double peaks have been observed.

5.6.1 Characteristics of Hard Peak-II

The hard peak-II (Figure 5.17) have very interesting characteristics. We see that the hard flare (Peak-II) for all outbursts are appearing at a similar time with a time shifting for 2002 and 2004 outbursts. For 2006/07 and 2010/11 outbursts, they appear ~ 108 days after triggering. Since both 2002 and 2004 outbursts have two soft peaks corresponds two successive triggering discussed above, we consider the time zero to reach the hard peak-II corresponds to the time when $\dot{m}_h$ in Figure 5.15a,b approach the second constant value (beginning of solid line). This is 50 days (2002 outburst) and 95 days (2004 outburst) after the first triggering respectively. Finally, in Figure 5.17e (middle panel), we plot the 6.0-20.0 keV hard flux after 50 days (2002) and 95 days (2004) onwards along with the other two outbursts. The red-solid, green-dot, magenta-dash and blue-dash dot lines represent

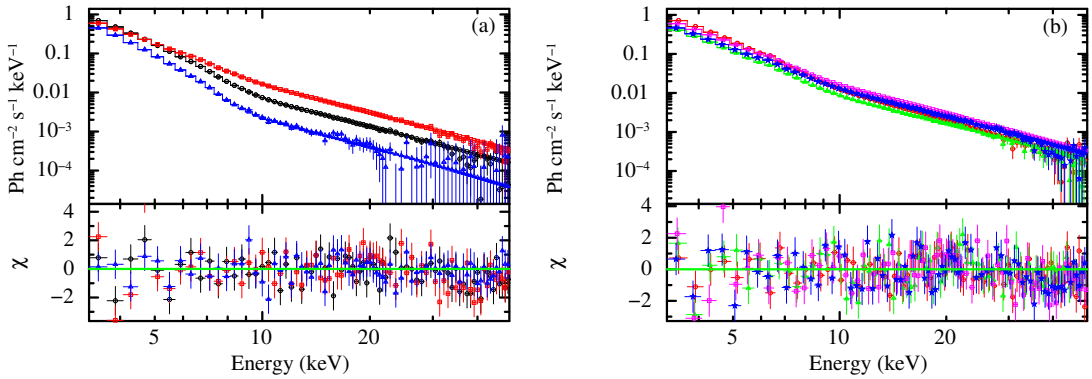

Figure 5.18: (a) Spectral fitting before (black-circle on MJD 54159.51), after (blue-triangle on MJD 54172.39) and at the peak-II (red-square on MJD 54161.67) of the hard flare during 2006/07 outburst. (b) Spectral characteristics at hard peak-II for 2002/03 (red-circle), 2004/05 (green-triangle), 2006/07 (magenta-square) and 2010/11 (blue-star) outbursts.

the hard flares (peak-II) for 2002/03. 2004/05, 2006/07 and 2010/11 outburst respectively. We see that Peak-II appears after $\sim$ 110 days in all cases i.e., the hard flaring signature after the maximum of soft flux in SIMS are generic to every outburst of this source. This is possibly a direct indication of irradiation DIM origin of outburst for this source.

We study the spectral characteristic around the hard flare and as a representative case in Figure 5.18a, we have shown PCA spectra before (black-circle), after (blue-triangle) and at peak-II (red-square) of 2006/07 outburst. It shows that the hard component of flux at peak-II is significantly more than the flux before and after the peak-II and we see a similar spectral behaviour around peak-II in all other outbursts. The existence of hard flares in SIMS (Brocksopp et al., 2002; Tomsick et al., 2003; Corbel et al., 2004; Joinet et al., 2005; Cadolle Bel et al., 2009; Nandi et al., 2018) are observed in many other BH outbursting sources as well. This may be due to the evacuation of the inner portion of the disc such that low energy flux reduces and the overall spectrum becomes harder. Also, radio jets are commonly observed (Fender, 2001; Corbel & Fender, 2002; Fender, 2001) during hard flares in SIMS but no radio observations exist during hard peak-II of this source. In Figure 5.18b, we have shown a comparison of PCA spectra during hard peak-II for all outbursts. The figure shows spectra with very similar spectral indices and flux values. Thus, all four outbursts can be unified with similar rising time (after introducing a second triggering for 2002/03, 2004/05 outbursts), the appearance of hard flare at similar time scales even though they have very different flux at maxima.

5.6.2 Long vs Short Rise Time Outburst: A Possible Scenario

We can calculate the outer radius (Frank et al., 1986) of the Keplerian disc, $R_0 \sim 4.4 \times 10^{11}$ cm (given $M \sim 9.0 M_\odot$, mass ratio $q \sim 0.18$ and binary period of $P_{orb} \sim 1.75$ days). This provides a critical accretion rate $\dot{m}_{dc} \sim 4 \times 10^{18}$ gm/s $\sim 0.3 \dot{M}_{Edd}$ (Frank et al., 1986, Equ 5.106). If $\dot{m} < \dot{m}_{dc}$ the source shows a transient behavior without any irradiation. Whereas for $\dot{m} > \dot{m}_{dc}$, the irradiation forces the whole disc to be in the hot state and the disc finds a steady state with persistent activities (King & Ritter, 1998). We see from Figure 5.16 that in the flat part $\dot{m}_d \gtrsim \dot{m}_{dc}$, indicates quasi-steady activities after peak-I whereas 2004/05 outburst requires a lower value of $\dot{m}_{dc}$. The corresponding sound speed is $c_s \sim 5.8 \times 10^5$ cm/s at R_0 from the standard (Shakura & Sunyaev, 1973) picture. The hot front move inward with speed $\alpha_{vis} c_s$, where α_{vis} is the viscosity parameter in the hot branch of the disc and the rising time of the outburst is $R_0/\alpha_{vis} c_s \sim 88.6$ days (for $\alpha_{vis} = 0.1$). This is very similar to the observed result (t_{3-6} and t_{6-20} of Table 5.3) from multiple outbursts of the source.

The outbursting source, H1743-322 is having a shorter rise time with smaller orbital parameters (§4.4.4) and therefore, the outburst triggers at a radius much smaller than GX 339. Whereas the outbursting LMXB, GRO J1655-40 has similar binary characteristics ($M \sim 7 M_\odot$, $q \sim 0.33$, $P_{orb} \sim 2.62157$ days) as GX 339-4 but having a much faster rising profile (rise time $\sim$ 12 days) for the primary outburst lightcurve. Such a short rise time indicates that outburst cannot be triggered at the outer edge of the Keplerian disc. Esin et al. (2000) have applied irradiated DIM to explain the strongly flaring plateau state but without addressing the rise time. Alternately, an outburst may also initiate due to instability in the existing sub-Keplerian halo in quiescence by a sudden enhancement of viscosity and the effect of instability can propagate in a sub-Keplerian flow faster than viscous timescale. Due to this instability, a fraction of the sub-Keplerian matter can convert into Keplerian matter keeping the total accretion rate roughly constant (Chakrabarti, 1997). Using hydrodynamic simulation, (Giri & Chakrabarti, 2013) have shown that sub-Keplerian matter can be converted into Keplerian matter with viscosity parameter above a certain critical value. Sub-Keplerian halo is generally optically thin and radiatively not very efficient, particularly in soft X-ray. That is why in LHS where the flow is mostly dominated by sub-Keplerian flow the source is low luminous. Whereas the same amount of matter in a Keplerian disc is radiatively more efficient because it could emit as a blackbody. Hence, during the evolution of outburst if sub-Keplerian matter is converting into Keplerian matter the overall luminosity increases. In addition, Mandal & Chakrabarti (2010) have shown that the general HID

profile of 2005 outburst of GRO J1655-40 can be explained with this proposal using the variation of accretion rates as powerlaw.

A logarithmic time response of accretion rates may be a signature of outburst with relatively longer rising time and very extended outer edge of the Keplerian disc. Hence, mass transfer at the outer edge continues along with the outburst. Whereas an outburst with shorter rising time associates with powerlaw nature of mass transfer (Mandal & Chakrabarti, 2010; Lipunova, 2015; Aneesha & Mandal, 2020) and having a smaller accretion disc. We have tried to model the general profiles of parameters evolution and overlooked the detailed day-to-day variations. In general, particularly in the intermediate states, the behaviour of the systems are highly non-linear and time dependent radiation-hydrodynamic studies are required to address these issues properly. Nevertheless, the detail physics behind this process is unclear and in future we aim to apply this study on a few other outbursting sources to get a more clear picture.

5.7 Discussions

In this chapter, we have studied both spectral and dynamical evolution of outbursting source GX 339-4. We have used RXTE as well as nearly simultaneous Swift/XRT and XMM-Newton/pn data during 2002-2011 for this study. The simultaneous broadband spectral modelling is shown in Figure 5.4, 5.5, 5.6. The evolution of spectral parameters are presented in §5.4.1. We see PCA data alone cannot constrain T_{in} in LHS and simultaneous observations (red-dash points in Figure 5.7d) towards lower energy are required. In all other states T_{in} have similar values for all outbursts though `diskbb norm` (Figure 5.8) have very different values. The powerlaw index (Figure 5.9) evolve between $1.5-3$ during LHS to HSS. It remains constant in LHS and follow an anti-clockwise hysteresis with the 6.0-20.0 keV flux. The `powerlaw norm` (Figure 5.10) shows high values during the rising phase and hard flare in SIMS. In Figure 5.11, we observe that the Fe line flux is week in LHS and the strength increase towards softer states. The line normalization (Figure 5.12) shows a decreasing requirement of line during successive outbursts after 2002/03 and the minimum value of the line normalization increases for later outbursts.

The spectral modeling using two-component accretion flow is presented in §5.5. We can understand the evolution of the spectral parameters (§5.4.1) from the evolution of the accretion parameters (§5.5.2). Figure 5.16 and Figure 5.7 show that as $\dot{m}_d$ increases T_{in} also increases in the rising phase and both decrease in the declining phase. The photon index (Figure 5.9) remains constant in LHS as $\dot{m}_h$ is constant (Figure 5.15) and $\dot{m}_d$ has a

low value (Figure 5.16). As $\dot{m}_d$ increases, the supply of soft photons becomes more and it cools the PSR which decreases the 6.0-20.0 keV flux and the spectral index increase towards softer states. The reflection signature (and hence line flux) is low (Figure 5.11) in LHS as the source is faint and the Keplerian disc is far apart. As the source evolves towards softer state, the Keplerian disc reaches closer to the source. Also the presence of significant hard flux from the PSR makes the line flux strongest in SIMS. We can understand the dynamical evolution of the system during all outbursts from Figures 5.14, 5.15, 5.16. We present a logarithmic evolution of accretion rate (Equation 5.1 and Equation 5.2) to understand the outburst evolution and expect to hold for outburst with longer duration. In this case, the total accretion rate is not constant and Keplerian disc extends to very large distance. We have explained the evolution of all the outbursts of GX 339-4 in the light of irradiate DIM using two-component accretion flow (§5.5.2). For outbursts with shorter duration may have a smaller accretion disc and the accreting matter pileup at the outer edge. The sudden enhancement of viscosity triggers the outbursts with a conversion of sub-Keplerian matter into Keplerian matter and keeping the total accretion rate roughly constant. Here, we have tried to understand the general behaviour of accretion parameters evolution and ignoring the small scale variations. In Figure 5.14, 5.15, 5.16, we have done a manual fitting to understand the behaviour of the general profile and did not estimate the errors in the parameters given in Table 5.2. This is one of the caveats in the current study.

The observed light curves of 2002/03 and 2004/05 outbursts appear very different from 2006/07 and 2010/11 outbursts. But introducing a second triggering of outburst after the hard peak-I due to irradiation from the central X-ray source resembles that soft peak-II in 2002/03 and 2004/05 outbursts appear at a similar rising time of 2006/07 and 2010/11 outbursts. This unified picture of all four outbursts are supported by the two-component model fitting as well (Figure 5.15a,b) by halting the decreasing trend of $\dot{m}_h$ after peak-I. The presence of hard flares in SIMS have been observed in many outbursting galactic black hole sources. But the appearance of hard flares (Figure 5.17e) around similar time (~ 110 days) after triggering (from second triggering time for 2002 and 2004 outbursts) for all outbursts is associated with the intrinsic nature of this source that the soft flux reaches the maxima at similar time scale. This can be attributed to the irradiation in the accretion disc by the central source. In future, we would like to implement these two pictures in other outbursting sources as well and may be able to get a better understanding of these systems.

Chapter 6

AstroSat View of Persistent Black Holes GRS 1758-258 and 1E 1740.7-2942

The persistent XRBs show continuous X-ray activity due to ongoing accretion of material from the companion star over years. Usually, they have high accretion rate ($\dot{M} \sim 10^{-10}\,\mathrm{M_\odot\,yr^{-1}}$) (Tanaka & Shibazaki, 1996) with high X-ray luminosity. In contrary, transient XRBs are generally found to be in quiescence state having very low accretion rate.

1E 1740.7-2942 and GRS 1758-258 along with Cygnus X-1 are only three persistent black hole binaries in our galaxy which are generally observed to be in the LHS whereas the persistent black hole binaries 4U1957+11, LMC X-1 and LMC X-3, are mostly found in the soft state. In the low energy X-ray band ($< 40\,\mathrm{keV}$) about ten sources have been detected within 10° around the galactic centre. But the major contribution above 40 keV (Mirabel & Rodríguez, 1994) comes from 1E 1740.7-2942 and GRS 1758-258. It was understood from the BATSE/CGRO light curves that both the sources show two distinct spectral states (LHS and HSS), and the time scale of a spectral state transition is around several months to years (Zhang et al., 1997). These sources are categorised as black hole candidates because they show similar X-ray spectral and timing behaviour as that of Cygnus X-1 in the hard sate. The power density spectra of these two sources show a flat topped noise, breaking to a powerlaw (Smith et al., 1997). The high energy spectral modelling of both the sources require additional high-energy powerlaw component (Pottschmidt et al., 2008).

Generally, black hole sources are found to be luminous in the HSS but both 1E 1740.7-2942 and GRS 1758-258 show dim soft state (soft flux decrease when entering into the thermally dominated soft state) (Heindl, 2001; Pottschmidt et al., 2006; Obst et al., 2011; Hirsch et al., 2020). Possibly, the high interstellar absorption makes it too difficult to find them in soft X-ray states. Also, the binary companions have not been identified yet due to the high extinction towards these sources. The presence of double sided radio emitting jet

classifies these sources as microquasar (Mirabel et al., 1992; Rodriguez et al., 1992).

In this chapter, we discuss the spectral studies of two persistent black hole sources 1E 1740.7-2942 and GRS 1758-258 using the AstroSat observations during 2016 - 2018. This work is based on our announcement opportunity (AO) observations as well as AstroSat archival data on these sources. We have performed detailed broadband spectral modelling of the sources and estimate the spectral and accretion parameters. We want to investigate the spectral transitions, if any, in these persistent sources during AstroSat observations. Also, it is interesting to explore the nature of the HID in comparison with the transient sources studied in the previous chapters. We aim to address the persistent nature of the sources using the same accretion model applied to transient sources. One manuscript based on this work is under preparation.

6.1 Source Properties

GRS 1758-258: The black hole binary source, located 5° away from the galactic centre at $\mathrm{RA} = 17^{\mathrm{h}}58^{\mathrm{m}}06^{\mathrm{s}}.40$ and $\mathrm{DEC} = -25^{\circ}44'22''.6$, was discovered by Granat satellite in 1990 (Mandrou, 1990). Due to the proximity with the source GX 5-1, it is not possible to isolate the source using all sky monitor. The source mostly stays in the powerlaw dominated hard state (Soria et al., 2011) with an occasional transition to a thermal component dominated soft state (Pottschmidt et al., 2006). GRS 1758-258 shows a brightening hard state and a dim soft state (Pottschmidt et al., 2008) contrary to transient black hole sources. In the soft state, the flux above 3 keV is observed to decrease (Soria et al., 2011) whereas the black hole transients generally exhibit pivoting of flux around 10 keV. The HID of the source shows an occasional hysteresis pattern between hard and soft state in the energy range < 20 keV, but never return to the hard state observed in quiescence (Obst et al., 2011). Whereas above 20 keV the behaviour in HID is very similar like other persistent sources with no signature of hysteresis. Keck et al. (2001) estimated the mass of the black hole in the range $8 - 9\,\mathrm{M}_{\odot}$ with an assumed distance of $8.5\,\mathrm{kpc}$. Rothstein et al. (2002); Smith et al. (2002b) proposed that the most likely GRS 1758-258 is having a low mass companion, which is a K0 III giant with 18.45 ± 0.10 day binary orbit and accretes materials through Roche lobe overflow. But the identification of giant companion has come under doubt when more accurate astrometry (Muñoz-Arjonilla et al., 2010; Luque-Escamilla et al., 2014) is used. Hirsch et al. (2020) observed significant peaks drift between 18.47 and 18.04 day in the dynamic power spectra using PCA data. Therefore, the system may be classified as LMXB. The radio image shows the presence of jets and lobes. The radio lobes have a

Z-shaped winged morphology that mimics many extragalactic winged radio galaxies Martí et al. (2017).

1E 1740.7-2942: The X-ray source 1E 1740.7-2942 located $50'$ apart from galactic center at a position RA=$17^h40^m42^s.99$ and DEC=$-29°43'25''.3$. This source was discovered in 1984 by the EINSTEIN observatory (Hertz & Wood, 1984). The hard X-ray emission nature of this source was first reported by Skinner et al. (1987). The French imaging telescope SIGMA discovered variable $e^+ - e^-$ annihilation radiation from this source and the source is known as "Great Annihilator" (Bouchet et al., 1991; Sunyaev et al., 1991). The high amount of absorption and its position near the galactic centre favours the distance $\sim 8.5\,\mathrm{kpc}$ and the occurrence of bipolar jets disfavors the face on geometry of the accretion disc (Natalucci et al., 2014). del Santo et al. (2005) studied the spectral and temporal evolution of the source using RXTE and INTEGRAL data. The broadband spectral modelling of XMM-Newton, NuSTAR and INTEGRAL data with reflection component provides a lower limit of inclination angle to be $> 50°$ (Stecchini et al., 2020). Also, modelling broadband spectra with a different combination of disc models provides a mass range $3 - 10M_\odot$ with the best estimate as $4.7\,\mathrm{M}_\odot$ (Stecchini et al., 2020).

6.2 Observation

In this work, we consider the simultaneous AstroSat SXT and LAXPC observations of GRS 1758-258 and 1E 1740.7-2942. These sources were observed by Astrosat based on the accepted proposal for the announcement opportunity (A02 and A03 cycles) during 2016 and 2017 respectively. Apart from these, we also consider AstroSat archival data (G08 cycle). GRS 1758-258 has been observed by AstroSat in four epoch. The first observation was for 30 ksec (AO2) on 14-15th October 2016. The second and third observations (AO3) were on 28th July and 20th September 2017 with 20 ksec exposure time. Finally, the fourth observation (G08) was conducted on 8-9th April 2018 for an exposure of 82 ksec in LAXPC and 45 ksec in SXT.

The second source, 1E 1740.7-2942 was observed by AstroSat for a duration of 10 ksec (AO2) on 6th October 2016. Also, we have considered observation performed during 25-26th February and 11-12th May 2018 for 30 ksec of LAXPC and 16.6 ksec of SXT data. A detailed observation-log are given in Table A2 (GRS 1758-258) and Table A3 (1E 1740.7-2942).

We note that both these sources are close to the galactic centre and may be in prox-

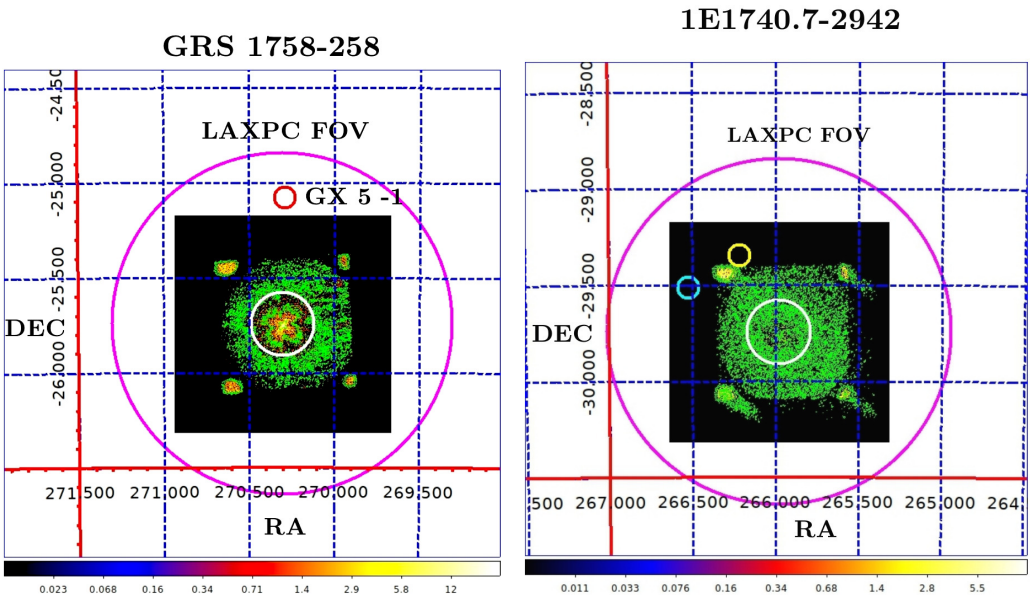

Figure 6.1: SXT image of GRS 1758-258 (left) and 1E 1740.7-2942 (right) during the 2016 observations. The target source region is shown by white circle of radius $10'$. The LAXPC field of view is shown in magenta circle of radius $0.9°$. Also, other sources in the LAXPC FoV are marked as: GX 5-1 (red circle); KS 1741-293 (yellow circle) and 1A 1742-294 (cyan circle).

imity of other X-ray sources. Therefore, we are particularly careful to check any possible contamination in the target data by the neighbouring sources.

6.3 Contamination due to Neighboring Sources

We have created SXT image of GRS 1758-258 during October, 2016 and it is shown in the left panel of Figure 6.1. The source region is marked with a white circle of radius 10 arcmin. Also, the LAXPC field of view is plotted in magenta circle of radius $0.9°$. We could identify one neighboring source GX 5-1 (marked in red circle) within the LAXPC FoV but outside the SXT source region. Therefore, SXT data of GRS 1758-258 is free from any contamination whereas there may be possible contamination in the LAXPC data by GX 5-1. We consider only SXT data of GRS 1758-258 for this study.

SXT image of 1E 1740.7-2942 is plotted in the right panel of Figure 6.1 for October, 2016 observation. The source region is shown by the white circle of radius 10 arcmin and the LAXPC FoV is represented by the magenta circle. We identify two neighbouring sources KS 1741-293 (yellow circle) and 1A 1742-294 (cyan circle) within the LAXPC FoV. These two are neutron star binary systems and may produce thermonuclear bursts. Therefore, we expect possible contamination from these two sources in the LAXPC data.

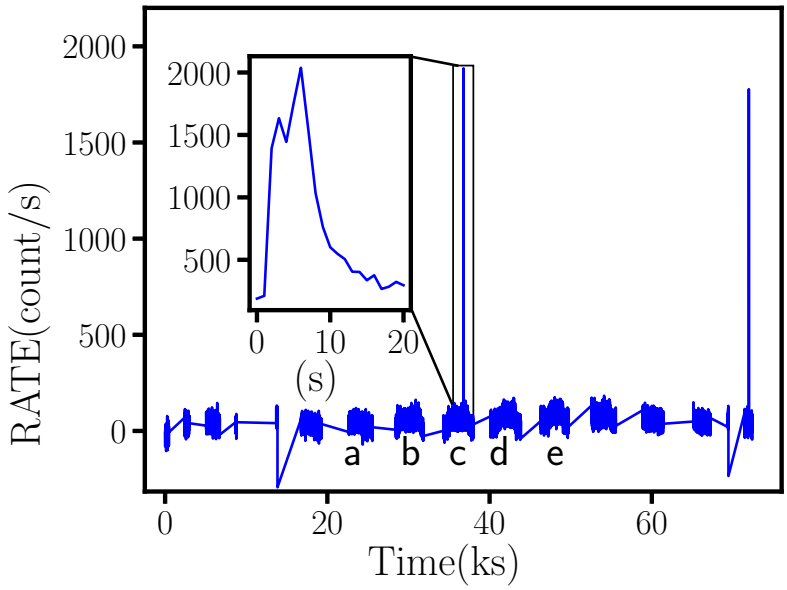

Figure 6.2: LAXPC light curve of 1E 1740.7-2942 for orbit 05561 (2016-10-07). The spikes in the lightcurve are having a type-I burst characteristic which is shown in the inset.

We have checked the MAXI and Swift/BAT light curve of 1A 1742-294 during AstroSat observations of 1E 1740.7-2942 and did not find any significant activity from this source. The second source, KS 1741-293 was not observed by MAXI or Swift/BAT but was monitoring by INTEGRAL. There was no INTEGRAL observation exactly overlapping with AstroSat observation of 1E 1740.7-2942. This does not rule out possible contamination in the LAXPC data due to type-I burst in KS 1741-293. We generate LAXPC light curve of 1E 1740.7-2942 for different orbits and could see the occasional appearance of high count rate. One such light curve generated for the October 2016 (orbit 05561) is shown in Figure 6.2. The data gaps in the light curve represent the SAA region passage and earth occultation. We see two spikes signature with very high counts and one of them is zoomed in the inset. It shows a type-I burst characteristic (fast rise and exponential decay) with a duration of 20 sec which is not expected from a black hole system. This burst profile may come from 1A 1742-294 and KS 1741-293. We could detect a total of six such burst activities during AstroSat observations and we exclude all the six segments of LAXPC data from our analysis. Also, we have done the spectral study to understand if there is any significant contribution in the LAXPC data by the source KS 1741-293 before and after the burst activity. We generate individual LAXPC spectrum of four full segments, two before the burst (segment **a** and **b** in Figure 6.2) and two after the burst (segment **d** and **e** in Figure 6.2). These spectra are fitted with the model `tbabs×edge(gaussian+powerlaw)` and are

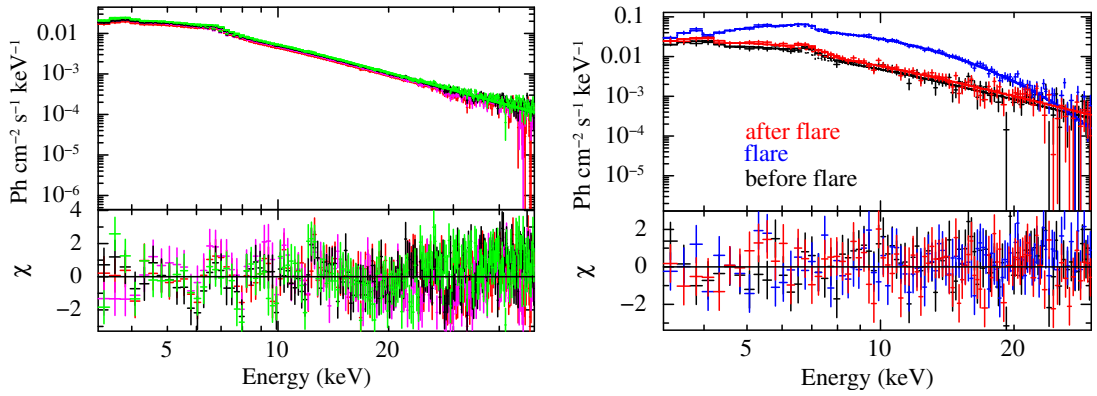

Figure 6.3: Left panel: The comparison of LAXPC spectrum of 1E 1740.7-2942 generated from segments (**a**, **b**, **d**, **e** in Figure 6.2). Different colour represents spectrum of different segments as: red (segment **a**), magenta (segment **b**), black (segment **d**) and lime (segment **e**) respectively. Right panel: LAXPC spectra of 1E 1740.7-2942 (from the segment **c** in Figure 6.2) for a duration of 20 sec just before (black), during (blue) and after (red) the flare respectively.

shown in the left panel of Figure 6.3. Here, different colours represent spectrum of the data segments as follows: red line (segment **a**), magenta (segment **b**), black (segment **d**) and lime (segment **e**) respectively. All the four spectra show very similar spectral characteristic having a photon index 2.48. Also, we fit only SXT spectra (no contamination) during the LAXPC observations and find very similar spectral index. This shows that the LAXPC data of 1E 1740.7-2942 can be used simultaneously with SXT whenever flaring activities are absent.

We also check the spectral characteristics of flaring and non-flaring data of the lightcurve (segment **c** in Figure 6.2). We generate spectrum having the same duration as that of the burst (20 sec) just prior to the onset of the burst (black), during burst (blue) and just after the burst (red) which are plotted in the right panel of Figure 6.3. The burst spectrum (blue) shows the presence of a strong `diskbb` signature with inner disk temperature 3.21 keV whereas the persistent spectra (black and red) are fitted with powerlaw. We see that the burst activity is prominent in the energy range 4-25 keV (see right panel of Figure 6.3) with maximum flux around 5-7 keV whereas X-ray activity of 1E 1740.7-2942 extends beyond 50 keV (left panel of Figure 6.3).

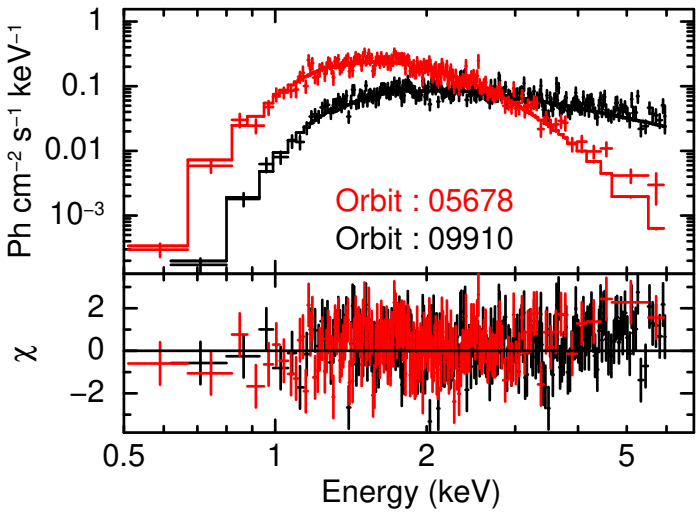

Figure 6.4: SXT spectrum of GRS 1758-258 on 2016-10-15 (MJD 57676) is fitted with the model `tbabs×diskbb` (red) whereas SXT spectrum on 2017-07-28 (MJD 57962.33) is fitted with the model `tbabs×powerlaw` (black).

6.4 Spectral Analysis

We have analysed the AstroSat data obtained from ISRO's archival webpage hosted at ISSDC[1]. The observed data are reduced following the reduction techniques summerised in §3.2.5 and §3.2.6. We choose SXT data with a minimum exposure time of 500 sec for better statistics in spectral analysis whereas a minimum exposure of 1000 sec has been considered for LAXPC data. We have added a systematic error of 2% to account the residual uncertainties in the LAXPC instrumental calibration as suggested by the instrument team. We have used 0.5% systematic error for the residual uncertainty in SXT instrument calibration. In the case of SXT data analysis, for both the source we have used the background spectra provided by the SXT instrument team.

6.4.1 Phenomenological Modelling of GRS 1758-258

Several studies have been done to estimate the hydrogen column density (n_H) along the line of sight. Mereghetti et al. (1997) have quoted hydrogen column density $(1.5 \pm 0.1) \times 10^{22}\,\mathrm{cm}^{-2}$ from ASCA observations whereas Keck et al. (2001) found $n_H = (0.98 \pm 0.08) \times 10^{22}\,\mathrm{cm}^{-2}$ using ROSAT observations. Lin et al. (2000) reported $n_H = (0.93 - 2.0) \times 10^{22}\,\mathrm{cm}^{-2}$ from RXTE observations and Goldwurm et al. (2001) estimated $n_H =$

[1] https://www.issdc.gov.in/astro.html

Table 6.1: Phenomenological model fitting parameters of GRS 1758-258

Orbit	Date (MJD)	kT_{in} (keV)	N_d	Γ_p	N_p	$F_{0.5-6}$	χ^2/dof
05678	2016-10-15 (57676.7)	0.53 ± 0.02	2986.3 ± 72.8	-	-	$11.11^{+0.56}_{-0.07}$	299.8/265
09904	2017-07-28(57962.3)	-	-	1.49 ± 0.03	0.36 ± 0.01	$9.66^{+0.11}_{-0.14}$	361.6/397
09910	2017-07-28 (57962.33)	-	-	1.90 ± 0.02	0.70 ± 0.02	10.32 ± 0.20	451.8/432
10708	2017-09-20 (58016)	-	-	1.82 ± 0.03	0.63 ± 0.02	11.58 ± 0.35	301.2/364
13673	2018-04-08 (58216)	-	-	1.82 ± 0.03	0.11 ± 0.03	2.12 ± 0.08	213.1/212

Note: KT_{in} is the inner disc temperature, N_d is the normalisation of `diskbb`*, Γ_p is the powerlaw photon index, N_p is the powerlaw normalisation and $F_{0.5-6}$ is the flux measured in the 0.5-6 keV given in the units of* 10^{-10} ergs/cm^2/sec.

$(1.74 \pm 0.07) \times 10^{22}\,\mathrm{cm}^{-2}$ using XMM-Newton data. We use $n_H = 1.8 \times 10^{22}\,\mathrm{cm}^{-2}$ for all the spectral modelling of the source.

In this study, we have modelled the SXT spectra during October 2016 (orbits 05663, 05671, 05673, 05678 and 05682) with the model `tbabs×diskbb`. The presence of a `diskbb` component represents a thermally dominated soft state where the accretion disc mostly contributes to the emitted flux. One such fitted spectrum for orbit number 05678 is shown in Figure 6.4 with red colour. The inner disc temperature almost remains constant $\sim 0.53\,\mathrm{keV}$ during these observations.

The SXT spectra during July 2017 are modelled with `tbabs×powerlaw` and one representative fitted spectrum is shown in the right panel of Figure 6.4. In a given epoch, we find very small variation in the estimated parameters and therefore we have tabulated the model parameters for a few selected observations in Table 6.1. Also, we have estimated the flux in the energy range 0.5-6 keV which is mentioned in the Table 6.1. During July 2017, the photon index ~ 1.5 which indicate the source was in the hard state during these observations. This means the source has gone through a state transition between October 2016 and July 2017 but the 0.5-6 keV energy flux does not show much variation. During September 2017, the photon index becomes 1.8 with a small increase in 0.5-6 keV flux which is more than the flux in the soft state. Whereas during April 2018, the photon index remains around the same value with a sharp decrease in 0.5-6 keV flux, possibly an indication of fading/dimming. Also, we did not find any Fe line signature in any epoch of these observations. We estimate the parameter uncertainty using `migrad` method within 90% confidence range.

6.4.2 Two-Component Spectral Modelling of GRS 1758-258

We also, fit all the SXT spectra of GRS 1758-258 with two-component model using interstellar absorption model `tbabs`. We use $n_H = 1.8 \times 10^{22}\,\mathrm{cm}^{-2}$ for all the spectral modelling of the source. The spectral fitting for the same two orbits (as in Figure 6.4) are

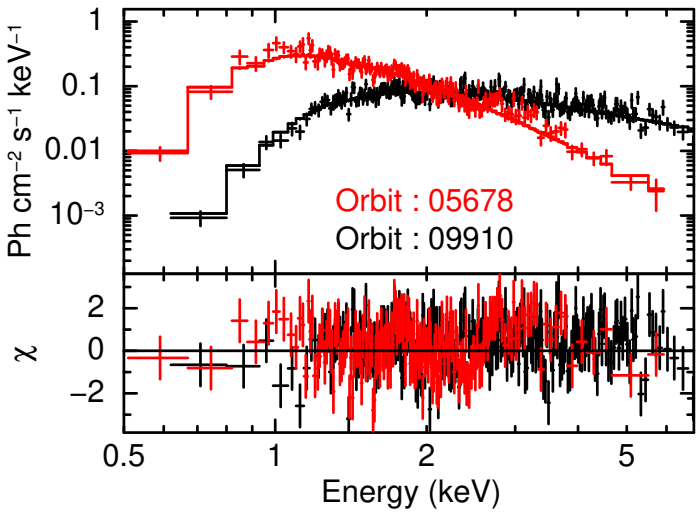

Figure 6.5: SXT spectrum of GRS 1758-258 on 2016-10-15 (red) and 2017-07-28 (black) are fitted with two-component accretion model.

shown in Figure 6.5 with red and black colour respectively. We have listed the estimated two-component model parameters in Table 6.2 for the same orbit numbers as in Table 6.1. The error in each parameter is calculated using `migrad` method with 90% confidence limit.

We see that the Keplerian disc rate is highest $\dot{m}_d \sim 0.5$ during October 2016 epoch with very little sub-Keplerian rate and the shock location is closest to the object. This shows that the Keplerian disc contributes to the flux in producing a soft state. Interesting to note that the shock location generally reach very close $(5 - 10r_g)$ to the central source in the HSS with highest luminosity of the source. In contrary for GRS 1758-258, the minimum value of $x_s \sim 55$, still far from the central object and produce a dim-soft state. In July-September 2017 epoch, we understand from Table 6.2 that x_s moves far away from the central object and $\dot{m}_h$ increases which increases the temperature of the PSR. Along with this the decline in $\dot{m}_d$ allows inverse-comptonisation to be more prominent and producing a harder spectrum. During April 2018, the relative values of $\dot{m}_h$ and $\dot{m}_d$ still keep the source in the hard state but the Comptonization contribution decreases as x_s moves inside. This decreases the 0.5-6 keV flux as indicated in Table 6.1.

The most reliable method for estimating the mass of the central source is based on the radial velocity measurement (§1.2.1) of optical/infrared counterpart. X-ray spectral modelling with the two-component model provides an opportunity to calculate the mass of the black hole source. The spectral modelling provides the mass of GRS 1758-258 in the range $9.2\mathrm{M}_\odot < \mathrm{M} < 10.6\mathrm{M}_\odot$ (Table 6.2) which is consistent with the measurement

Table 6.2: Two-component model fitting parameters for GRS 1758-258

Orbit	Date (MJD)	$m_{bh}(\mathrm{M}_{\odot})$	x_s ($\mathrm{r_g}$)	$\dot{m}_h\,(\dot{\mathrm{M}}_{\mathrm{Edd}})$	$\dot{m}_d\,(\dot{\mathrm{M}}_{\mathrm{Edd}})$	χ^2/dof
05678	2016-10-15 (57676.7)	10.0 ± 0.2	55.9 ± 0.1	0.007 ± 0.001	0.54 ± 0.01	313.6/262
09904	2017-07-28 (57962.3)	9.7 ± 0.2	107.4 ± 7.5	0.08 ± 0.004	0.16 ± 0.005	361.5/394
09910	2017-07-28 (57962.33)	10.1 ± 0.2	$148.2^{+11.2}_{-9.8}$	0.15 ± 0.002	0.12 ± 0.001	567.8/430
10708	2017-09-20 (58016)	10.3 ± 0.3	$148.2^{+7.8}_{-4.3}$	0.03 ± 0.001	0.12 ± 0.003	302.3/361
13673	2018-04-08 (58216)	9.5 ± 0.3	$75.3^{+4.1}_{-3.9}$	0.04 ± 0.002	0.11 ± 0.003	212.9/208

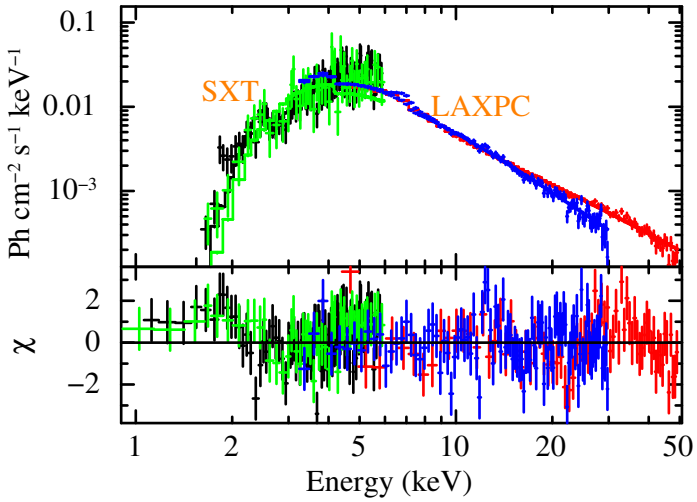

Figure 6.6: The broadband spectra of 1E 1740.7-2942 on 2016-10-06 (orbit 05548) are represented with green (SXT) and blue (LAXPC) whereas black (SXT) and red (LAXPC) denote the broadband spectra on 2018-05-11 (orbit 14160). Both the spectra are modeled with `tbabs(gauss+powerlaw)`.

available in the literature.

6.4.3 Phenomenological modelling of 1E 1740.7-2942

In order to understand the X-ray spectral characteristic, we have performed broadband spectral modelling of 1E 1740.7-2942 for all SXT and LAXPC data during 2016-2018. We note that the source region in SXT image had an offset from the centre for February 2018 observation. To take care of this, we estimate the normalisation constant for SXT data, keeping the normalisation of LAXPC at unity. The effective area of SXT is then multiplied by this factor and the modified ARF file is used for spectral analysis. We have fitted the SXT+LAXPC data of 1E 1740.7-2942 with the model `tbabs(gauss + powerlaw)` with `wilm` abundance. We use χ^2 statistics for spectral fitting and estimate the model parameters. We notice that for a given epoch the spectral variations are within the uncertainties and therefore we have summerised the model parameter values for few selected

Table 6.3: Phenomenological model fitting parameters of SXT-LAXPC spectra of 1E 1740.7-2942

Orbit	Date (MJD)	n_H (10^{22} cm^{-2})	Γ_p	N_p	$F_{0.5-6}$	F_{4-60}	χ^2/dof
05548_1	2016-10-06 (57667)	26.65 ± 2.81	2.59 ± 0.05	2.16 ± 0.57	7.59 ± 0.38	25.90 ± 0.99	222.2/178
05558_1	2016-10-07 (57668)	20.04 ± 1.03	2.31 ± 0.03	1.05 ± 0.10	7.35 ± 0.05	26.32 ± 0.14	388.7/291
13047_1	2018-02-25 (58174)	19.28 ± 1.00	2.46 ± 0.02	2.20 ± 0.28	12.30 ± 0.29	36.69 ± 0.45	422.3/267
13050_1	2018-02-25 (58174)	16.79 ± 0.90	2.33 ± 0.02	1.56 ± 0.20	11.39 ± 0.33	34.32 ± 0.50	383.8/253
14160_1	2018-05-11 (58249)	16.11 ± 1.12	2.19 ± 0.02	$0.78^{+0.10}_{-0.09}$	8.12 ± 0.12	28.54 ± 0.72	335.8/197

Note: Γ_p is the powerlaw photon index, N_p is the powerlaw normalisation and $F_{0.5-6}$ and F_{4-60} are the flux measured in the 0.5-6 keV and 4-60 keV respectively and are given in the units of 10^{-10} $\mathrm{ergs/cm^2/sec}$.

observations in Table 6.3. Also, the estimated flux in the energy range 0.5-6 keV and 4-60 keV are mentioned in the Table 6.3.

The broadband spectral fitting for the observation on 6th October 2016 (orbit 05548_1), is shown with green (SXT) and blue (LAXPC) in Figure 6.6. We could find the presence of Fe-line signature around 6.4 keV in the LAXPC data. It is possibly due to the bright 6.4 keV fluorescence emission from the Galactic center (Dogiel et al., 2009). The photon index is around 2.6 and possibly the source stays in an intermediate state. During the observation on orbit number 05558_1 i.e., 16 hours later, the spectrum hardens and photon index decreases to 2.3. During February 2018 the photon index of the spectrum remains similar but around a factor of 1.5 overall increase in flux both 0.5-6 keV and 4-60 keV band compared to October 2016. During May 2018 the spectrum becomes harder with a photon index around 2.1 and the overall flux decreases. The broadband spectrum corresponding to May 2018 is shown with black (SXT) and red (LAXPC) in Figure 6.6. Hence, the source continues to remain in the hard/intermediate state during 2016-2018 with significant variation of flux.

The estimated the hydrogen column density (Table 6.3) is higher than the typical value ($\sim 10^{22}\,\mathrm{cm^{-2}}$) in this direction of the galactic centre (Dickey & Lockman, 1990), and it might indicate that the source maybe embedded inside the molecular cloud (Yan & Dalgarno, 1997). However Sheth et al. (1996) found the hydrogen column density to be $8 \times 10^{22}\,\mathrm{cm^{-2}}$ from ASCA observation, whereas Sakano et al. (1999) determined $n_H = 10 \times 10^{22}\,\mathrm{cm^{-2}}$ again from ASCA observation. Observations based on XMM-Newton, NuSTAR and INTEGRAL provide an estimate of $n_H = (13 - 27.2) \times 10^{22}\,\mathrm{cm^{-2}}$ (Natalucci et al., 2014; Castro et al., 2014; Stecchini et al., 2020).

6.4.4 Two-Component Spectral Modelling of 1E 1740.7-2942

The SXT-LAXPC broadband spectra of 1E 1740.7-2942 are fitted with two-component model with additional model components like `gauss` and `smedge` whenever required. We have used `tbabs` model to account for the interstellar absorption in the line of sight.

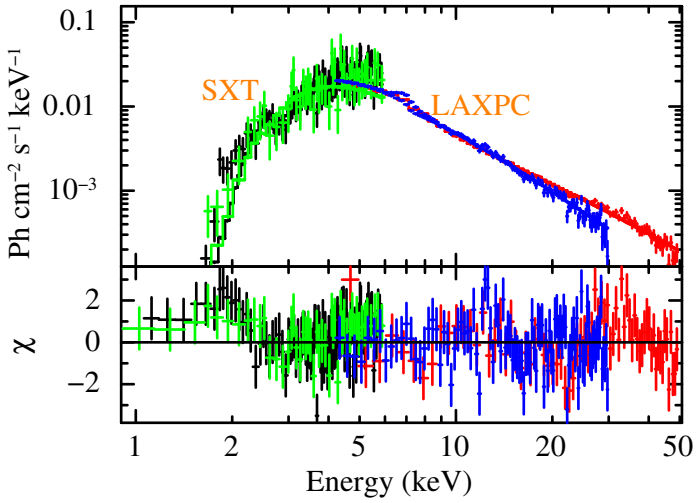

Figure 6.7: The broadband spectra of 1E 1740.7-2942 on 2016-10-06 (orbit 05548) are represented with green (SXT) and blue (LAXPC) whereas black (SXT) and red (LAXPC) show the broadband spectra on 2018-05-11 (orbit 14160). Both the spectra are fitted with the two-component model.

In Figure 6.7, we present the model fitted spectra on 2016-10-06 (orbit 05548) with green (SXT) and blue (LAXPC) whereas the same on 2018-05-11 (orbit 14160) are presented in black (SXT) and red (LAXPC). The estimated two-component model parameters are tabulated in Table 6.4 for the same orbit number as in Table 6.3.

In October 2016, the shock location is close ($\sim 8 - 10r_g$) to the central compact object and relatively higher $\dot{m}_d = 0.17$, are associated with photon index close to intermediate/soft state. The next observation within a day shows a significant decrease in $\dot{m}_d$ weakens the cooling of PSR and produces a hardened spectrum. In February 2018, an increase in $\dot{m}_d$ is consistent with the enhancement in overall flux (Table 6.3). The increase in the size of PSR (x_s moves away) enhances the number of hard photons due to Comptonization and the source continue to be in the hard state. In 2018 May epoch, both $\dot{m}_d$ and $\dot{m}_h$ decline which reduces both soft and hard photon flux. Along with this the shock location moves further apart which makes the spectrum to be even harder. Also, the spectral modelling provides the estimated mass of the black hole of 1E 1740.7-2942 in the range $8.9\mathrm{M}_\odot < \mathrm{M} < 10.5\mathrm{M}_\odot$ (Table 6.4).

6.5 Transient vs Persistent BHXRBs

We have considered two transient and two persistent low-mass BHXRBs in our study. Generally, the alternating outburst and quiescent phases in transient sources are explained very

Table 6.4: Two-component model fitting parameters from SXT-LAXPC spectra of 1E 1740.7-2942

Orbit	Date (MJD)	$m_{bh}(\mathrm{M}_{\odot})$	x_s ($\mathrm{r_g}$)	$\dot{m}_h\,(\dot{\mathrm{M}}_{\mathrm{Edd}})$	$\dot{m}_d\,(\dot{\mathrm{M}}_{\mathrm{Edd}})$	χ^2/dof
05548_1	2016-10-06 (57667)	9.5 ± 0.1	7.8 ± 0.3	0.04 ± 0.001	0.17 ± 0.001	218.9/175
05558_1	2016-10-07 (57668)	9.7 ± 0.6	9.6 ± 0.2	0.04 ± 0.003	0.13 ± 0.013	485.8/288
13047_1	2018-02-25 (58174)	9.2 ± 0.3	13.7 ± 0.6	0.03 ± 0.003	0.23 ± 0.02	416.5/263
13050_1	2018-02-25 (58174)	9.9 ± 0.3	14.9 ± 0.5	0.04 ± 0.005	0.21 ± 0.01	382.9/249
14160_1	2018-05-11 (58249)	10.1 ± 0.4	135.7 ± 6.8	0.01 ± 0.001	0.11 ± 0.02	274.2/193

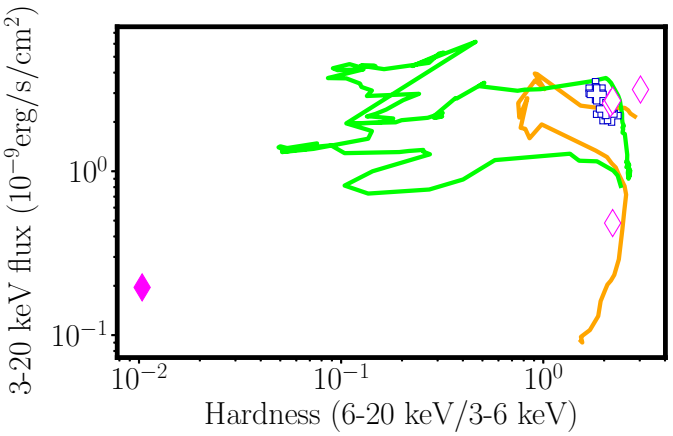

Figure 6.8: A comparison in the behaviour of GRS 1758-258 (magenta diamond) and 1E 1740.7-2942 (blue plus) in the HID of H 1743-322 (orange: 2011 outburst) and GX 339-4 (green: 2004 outburst.

well by irradiate DIM and the detailed descriptions are provided in previous chapters. It is observed that the transient sources continue to show quasi-steady persistent activity in some phase during an outburst and it is believed that a persistent accretion activity is responsible for the same. Therefore, the irradiation phase of a transient source is expected to exhibit the similar accretion physics that of the persistent source. We wish to compare the spectral and accretion evolution of persistent sources with the irradiated phase of the outbursting sources.

Both GRS 1758-258 and 1E 1740.7-2942 remain in the harder state in the majority of the time, though occasional transitions to the softer state are also seen. In the case of GRS 1758-258, we could see clear state transition between hard state and soft state in October 2016 epoch and back to the hard state ($\Gamma_p < 2$) during October 2017. Whereas we could identify multiple observations with photon index > 2 for 1E 1740.7-2942 but none of these is an obvious indication of a soft state. Nevertheless, both sources show some amount of spectral variability.

In Chapter 4 and Chapter 5, we have studied two transient BHXRBs (H 1743-322 and

GX 339-4) which show clear spectral state transitions in HIDs. To understand the similarity in the accretion scenario, it is interesting to compare the hardness characteristic of persistent sources with the same of the transient sources. In Figure 6.8, we have shown the HID associated with faintest complete outbursts of H 1743-322 in 2011 (orange) and GX 339-4 in 2004 (green) using RXTE/PCA data. We choose the weak ones because the expected variation of the flux of persistent sources should be at least comparable with the irradiation phase of these weak outbursts.

The AstroSat broadband data (0.5 - 60 keV) are available for 1E 1740.7-2942 and we calculate the flux in 3-20 keV range and we follow the same definition of hardness as in Figure 4.3 and Figure 5.3. The hardness evolution of 1E 1740.7-2942 is shown with blue plus symbols in Figure 6.8. For GRS 1758-258, we have available data from SXT in 0.5-6 keV only. To calculate the flux in 3-20 keV range and the hardness, we have extended the SXT response upto 20 keV during spectral modelling. This assumes that the current model is valid upto 20 keV and this is reasonable if the data are modelled with a `powerlaw` component. In Figure 6.8, the spectral evolution of GRS 1758-258 in HID are denoted with magenta diamond symbols. The filled magenta diamond represents the soft state observed during October 2016 observation where the SXT data are modelled with `diskbb`. Here, we need to be careful in extending the SXT response to 20 keV because a `diskbb` model with $kT_{in} \sim 0.5$ keV, does not have much contribution beyond 6 keV and hence the hardness becomes superficially soft. Also, it may underestimate the 3-20 keV flux because there may be a steep powerlaw component beyond 6 keV along with `diskbb` in the soft state and this is missing while extending the SXT response in the soft state. Previous studies (Obst et al., 2011) of GRS 1758-258 during soft state using RXTE/PCA data showed typical 3-20 keV flux $\sim (1.5 - 3.5) \times 10^{-10}\,\mathrm{erg/cm^2/sec}$ which is higher than the present estimate. We include GRS 1758-258 soft state data in HID to highlight this particular issue. We see that the 3-20 keV flux (except filled magenta diamond) of both the persistent sources are comparable with the same during the persistent activity phase of the transients. For GRS 1758-258, the hard data point having a low flux is an indication of a return to the hard state observed in quiescence. The hardness of the persistent sources is consistent with the hard/intermediate state whereas the transient sources stay in HIMS/SIMS during the irradiated active phase and cover more dynamic range.

We understand that the transient sources switch to persistent activities if the accretion rate crosses the critical accretion rate of the system. The estimated $\dot{m}_{dc}$ for H 1743-322 (§4.4.4) and GX 339-4 (§5.6.2) are ~ 0.08 and ~ 0.3 respectively. Though 2004 outburst

of GX 339-4 indicates a lower $\dot{m}_{dc} \sim 0.1$ (flat part in Figure 5.16b). Fender & Hendry (2000) argued that a high (~ 0.1) accretion rate and/or dramatic physical change in the accretion flow is required for the persistent X-ray activity. Since all four sources are low-mass BHXRBs and the mass of the central objects are in the comparable range, the estimated $\dot{m}_{dc}$ may apply to the persistent sources as well. We find that the estimated disc accretion rate ($\dot{m}_d$) (Table 6.2,6.4) are greater or comparable to the critical accretion rate of the system, justifying the reason behind persistent activities in GRS 1758-258 and 1E 1740.7-2942.

Understanding the persistent accretion activity in LMXBs is difficult to perceive. The compact object can accrete during its passage through the Roche lobe of the companion and this is a small fraction of the total binary period. So the systems with long binary period ($P_{orb} \gtrsim 2$ days) and small mass ratio ($q < 0.1$) (King et al., 1996) are going to accrete very slow and tend to be transient systems. Both the transient sources considered in our study have mass ratio ~ 0.1 but the orbital period $P_{orb} < 2$ days. The orbital period and mass ratio of the persistent sources (GRS 1758-258 and 1E 1740.7-2942) are not known though there are indications of ~ 18 days period (Hirsch et al., 2020) for GRS 1758-258. A binary system having such a long period is not expected to be persistent but the proximity of these sources toward the dense galactic centre may fuel sufficient gas to the compact objects.

6.6 Discussions

We have presented the spectral variabilities shown by two persistent sources GRS 1758-258 and 1E 1740.7-2942 using SXT and LAXPC data during 2016 - 2018. We have restricted our study on GRS 1758-258 to SXT data only due to the contamination from nearby sources. The LAXPC light curve of 1E 1740.7-2942 shows the occasional appearance of burst/flare and our simultaneous broadband (SXT+LAXPC) study is restricted to the data segments which do not have flaring signature. The contamination issue is discussed in detail in §6.3.

We have done both phenomenological and two-component modelling of GRS 1758-258 data and estimated the spectral (Table 6.1) and accretion parameters (Table 6.2. The phenomenological modelling of GRS 1758-258 spectra show spectral variation in the hard state as well as occasional transition to a soft state. This is consistent with the change in the accretion parameters. It is understood that the hard state is associated with relatively high $\dot{m}_h$, low $\dot{m}_d$ and large x_s. The spectral changes in the hard state are mainly controlled by x_s. The soft sate of GRS 1758-258 is usually dimmer than in the hard state. But Soria et al. (2011) found higher luminosity in 2001 XMM-Newton soft state data than 2008/2009

Swift/XRT hard state and conclude that luminosity can not be the only driving force behind the state transition. In fact, we see from Table 6.2 (orbit 05578), that GRS 1758-258 is in the soft state because of high $\dot{m}_d$ but it is dim because of the truncation (x_s) of the disc further outside. With the same $\dot{m}_d$, it could have produced HSS if x_s could have close to the central objects. This indicates that only one disc component can not explain both observations (HSS and dim soft sate) and inclusion of dynamic sub-Keplerian component is necessary.

During AstroSat observations, 1E 1740.7-2942 remains in the hard/intermediate state with variation in both flux and photon index. Table 6.3 shows a trend of spectral hardening (Γ_p decreases) which is consistent with the increase in the size of PRS (x_s increases in Table 6.4) and this enhances the number of Comptonized photons. The enhancement of overall flux is due to an increase of $\dot{m}_d$. Also, the LAXPC data show the presence of Fe line almost in all AstroSat observations of 1E 1740.7-2942. The two-component spectral modelling provides an estimate of the mass of 1E 1740.7-2942 in the range $8.9\mathrm{M}_\odot < \mathrm{M} < 10.5\mathrm{M}_\odot$ whereas the same for GRS 1758-258 lies between $9.2\mathrm{M}_\odot < \mathrm{M} < 10.6\mathrm{M}_\odot$.

Finally, we could link the behaviour of persistent sources in HID (Figure 6.8) with that of the transient sources during irradiation. We see similar spectral and accretion evolution during this phase and the two-component model could able to explain the behaviour of both persistent and transient sources. We find that the disc accretion rate in persistent sources is always greater or comparable to the critical accretion of the system. In future, we would like to extend this study towards HMXBs as well with simultaneous broadband data.

Chapter 7

Summary and Future work

Compact objects are powered by the accretion process due to their extreme nature of the gravity. In Chapter 1, we introduce the basic accretion processes in XRBs. It was understood that the spherical accretion is radiatively inefficient because of high radial velocity and the need for high angular momentum flow was justified. The standard accretion disc (Shakura & Sunyaev, 1973) was very successful in explaining the *Big Blue Bump* in AGN as well as the soft X-ray spectrum of XRBs. But sensitive observations showed the presence of high energy non-thermal component which initiated several developments on thick, hot accretion flow.

The main aim of the thesis is to understand the accretion physics around transient as well as persistent BHXRBs. We achieve this goal by exploring the spectral signatures as well as the accretion dynamics. We use the two-component accretion model (Chakrabarti & Titarchuk, 1995) to understand the accretion dynamics and the salient features of this model is discussed in Chapter 2. Whereas we use X-ray data from various space observatories to study the spectral characteristics of XRBs. The data reduction methods and extraction of scientific outputs (images, lightcurves and spectra) are summarised in Chapter 3.

The multiple outbursts of H 1743-322 (Chapter 4), show a large dynamic range in rising time, duration and luminosity whereas all the outbursts of GX 339-4 are having much longer rise time and duration. We use mainly RXTE/PCA data during 2002-2012 for the phenomenological as well as two-component spectral modelling of all the outbursts. The spectral modelling of GX 339-4 (Chapter 5) shows that the PCA data alone cannot constrain T_{in} in LHS, and simultaneous observations in lower energy are required. We have used simultaneous RXTE/XMM-Newton and RXTE/Swift observations, whenever available, for the spectral modelling of GX 339-4 but could not find the same for H1743-322. Both sources exhibit canonical HID pattern and spectral state transitions during outbursts. Also, the evolution photon index with the hard flux (6-20 keV) shows a hysteresis behaviour with

a much larger dynamic range in the rising part of the outbursts. We study the evolution of the phenomenological model parameters and understand that the spectral changes are explained by the relative variation of the accretion parameters. We employ the irradiated DIM into the two-component accretion flow scenario to understand the evolution of the accretion parameters and have proposed toy models for the time variation of accretion rates. Few important findings from our study on these outbursting sources are the followings.

- A powerlaw variation of accretion rates with a uniform motion of x_s could able to reproduce the evolution of the accretion parameters for sources (like H1743-322) with shorter rising time. Whereas the transient source GX 339-4, which is having longer rising time, show a logarithmic variation of accretion rates.

- We identify the characteristic rise and decline timescale of $\dot{m}_d$ (t_r, t_d) and $\dot{m}_h$ (t_h, t_s) in the soft ($3-6$ keV) and hard ($6-20$ keV) lightcurves. Here, t_r and t_h are associated with the first peak in the 3-6 keV and 6-20 keV flux respectively. It is expected that $t_h < t_r$ as the hard flux is associated with $\dot{m}_h$ which responses in infall timescale whereas t_r is linked with viscous timescale. We observe $8 - 12$ days delay (Figure 5.17) between the peaks of the hard and soft flux of GX 339-4 whereas the same has not been seen in H 1743-322, possibly due to short rise time. We understand that t_d is possibly associated with SIMS or HSS beyond which there is no more activity at the outer part of the Keplerian disc. We note that t_s represents the beginning of HIMS in the decline phase where the hard flux always dominates over the soft flux.

- In the absence of dynamical measurement, the two-component spectral modelling of X-ray data provides the mass of H 1743-322 within the range $8.58 - 10.98\,M_{\odot}$. The complete outburst in 2011 and the marginally failed outburst in 2008b provides an opportunity to estimate the critical accretion of H 1743-322 observationally. We find $0.076 < \dot{m}_{dc} < 0.086$ for triggering an outburst in H 1743-322. Whereas, we estimate $\dot{m}_{dc}$ for GX 339-4 using the orbital parameters and find $\dot{m}_{dc} \sim 0.3$. Though 2004 outburst of GX 339-4 indicates a lower value ($\dot{m}_{dc} \sim 0.1$). We understand that a transient source shows persistent behaviour as long as $\dot{m}_d > \dot{m}_{dc}$. We also estimate the orbital parameters of H 1743-322 and find a smaller orbital period ($P_{orb} \sim 15$ hrs) in compared with the same ($P_{orb} \sim 1.75$ days) for GX 339-4. This is possibly the reason for more frequent outbursts in H 1743-322.

- Also, we have calculated the rise time of the outburst using the orbital parameters and a typical assumption on viscosity parameter in the hot phase. We find $t_r \sim 25$

days for H 1743-322 which is consistent with the rise time of the 2003 outburst. The shorter rise time ($\sim$ 10 days) of the other outbursts of H 1743-322 indicates that the strong irradiation phase of the 2003 outburst may have pushed the pileup radius inside. The estimated rise time (t_r $\sim$ 88 days) for GX 339-4 closely matches with the observed value.

- We associate the three distinct peaks in the 2003 outburst lightcurve of H 1743-322 as the triggering of the outburst (first peak), irradiation of the cold outer disc (second peak), and irradiation of the secondary (third peak) respectively.

- For 2003 and 2004 outburst of GX 339-4, the initial X-ray activity possibly affects the binary companion and enhances the supply of matter at the outer part of the disc. This induces the second triggering of outburst and the sub-Keplerian rate comes to a halt (Figure 5.15a,b). We provide a unified view of all the outbursts of GX 339-4 by introducing a second instant of triggered instability in the accretion disc. Also, the outbursts show a second peak in the hard flux after 10-15 days from the overall maximum flux and the spectral characteristics at the second hard peak are very similar for all outbursts.

- The very luminous 2003 outburst of H 1743-322 could not be modelled with the `Xspec` implemented two-component accretion model. An additional non-thermal component along with the two-component model is required to fit the data. We propose that the additional powerlaw component is originated from the base of the jet and this is consistent with both X-ray and radio observations.

- Using the radio observations during 2009 outburst of H 1743-322, we could able to connect the jet activity with the accretion dynamics. We see steady jet and radio emission at the beginning and end of the outburst due to the high contribution of $\dot{m}_h$ and the absence (or very small contribution) of a jet in the HSS due to the cooling of PSR by the high rate of accretion of Keplerian matter

To complement our understanding of transient sources, we have also studied two persistent sources (GRS 1758-258 and 1E 1740.7-2942) using AstroSat data in Chapter 6. We could not use LAXPC data for GRS 1758-258 due to contamination from the nearby source. The broadband spectral studies of the sources are carried out by both phenomenological and two-component model. We find that most of the time these sources are in hard/intermediate state. Though they show spectral variation in the hard/intermediate state and GRS 1758-258 makes an occasional transition to a soft state. It is understood that the hard state

is associated with relatively high $\dot{m}_h$, low $\dot{m}_d$ and large x_s. The spectral changes in the hard state are mainly controlled by x_s. The soft sate of GRS 1758-258 is usually dimmer than in the hard state. We see from Table 6.2 (orbit 05578), that GRS 1758-258 is in the soft state because of high $\dot{m}_d$ but it is dim because of the truncation (x_s) of the disc further outside. With the same $\dot{m}_d$, it could have produced HSS if x_s could have close to the central objects. This indicates that only one disc component can not explain both observations (HSS and dim soft sate) and inclusion of dynamic sub-Keplerian component is necessary. During AstroSat observations, 1E 1740.7-2942 shows a trend of spectral hardening (Γ_p decreases) which is consistent with the increase in the size of PSR (x_s increases). We could constrain the mass of GRS 1758-258 in the range $9.2\mathrm{M}_\odot < \mathrm{M} < 10.6\mathrm{M}_\odot$ and $8.9\mathrm{M}_\odot < \mathrm{M} < 10.5\mathrm{M}_\odot$ for 1E 1740.7-2942 from the two component modelling.

Finally, we could connect the behaviour of persistent sources in HID (Figure 6.8) with that of the transient sources during irradiation. We see similar spectral and accretion evolution during this phase and the two-component model could able to explain the behaviour of both persistent and transient sources. The critical accretion rate of these persistent sources is expected to be ~ 0.1, assuming similar orbital parameters as all four sources are LMXBs. We find that the disc accretion rate of the persistent sources are always greater or comparable to the critical accretion of the system and therefore justify their persistent nature.

7.1 Future work

We have understood that the very luminous 2003 outburst of H 1743-322 cannot be modelled with the existing two-component model and an additional powerlaw component is required. In future, we plan to create a combined disc-jet model to extend our study into a more general situation.

Also, we aim to continue our study towards other outbursting sources which very rarely show any outburst and compare their properties with sources like GX 339-4 or H 1743-322. Another study of our interest is to explore the accretion properties of persistent and transient HMXBs.

So far, we have tried to understand the accretion dynamics of BHXRBs using solely the spectral analysis. We plan to extend similar studies based on timing analysis utilising the state of art timing instruments like RXTE/PCA, AstroSat/LAXPC etc.

Bibliography

Abramowicz, M. A., Czerny, B., Lasota, J. P., & Szuszkiewicz, E. 1988, ApJ, 332, 646, doi: 10.1086/166683

Abramowicz, M. A., & Zurek, W. H. 1981, ApJ, 246, 314, doi: 10.1086/158924

Agrawal, P. C. 2017, Journal of Astrophysics and Astronomy, 38, 27, doi: 10.1007/s12036-017-9449-6

Alfonso-Garzón, J., Sánchez-Fernández, C., Charles, P. A., et al. 2018, A&A, 620, A110, doi: 10.1051/0004-6361/201834102

Aneesha, U., & Mandal, S. 2020, A&A, 637, A47, doi: 10.1051/0004-6361/202037577

Aneesha, U., Mandal, S., & Sreehari, H. 2019, MNRAS, 486, 2705, doi: 10.1093/mnras/stz1000

Antia, H. M., Yadav, J. S., Agrawal, P. C., et al. 2017, ApJS, 231, 10, doi: 10.3847/1538-4365/aa7a0e

Augusteijn, T., Kuulkers, E., & Shaham, J. 1993, A&A, 279, L13

Baba, D., Nagata, T., Iwata, I., Kato, T., & Yamaoka, H. 2003, IAUC, 8112, 2

Belloni, T., Homan, J., Casella, P., et al. 2005, A&A, 440, 207, doi: 10.1051/0004-6361:20042457

Belloni, T., Méndez, M., van der Klis, M., Lewin, W. H. G., & Dieters, S. 1999, ApJL, 519, L159, doi: 10.1086/312130

Belloni, T. M. 2010, States and Transitions in Black Hole Binaries, ed. T. Belloni, Vol. 794, 53, doi: 10.1007/978-3-540-76937-8_3

Bhattacharjee, A., Banerjee, I., Banerjee, A., Debnath, D., & Chakrabarti, S. K. 2017, MNRAS, 466, 1372, doi: 10.1093/mnras/stw3117

Blandford, R. D., & Payne, D. G. 1982, MNRAS, 199, 883, doi: 10.1093/mnras/199.4.883

Bondi, H. 1952, MNRAS, 112, 195, doi: 10.1093/mnras/112.2.195

Bouchet, L., Mandrou, P., Roques, J. P., et al. 1991, ApJL, 383, L45, doi: 10.1086/186237

Brocksopp, C., Corbel, S., Fender, R. P., et al. 2005, MNRAS, 356, 125, doi: 10.1111/j.1365-2966.2004.08427.x

Brocksopp, C., Fender, R. P., McCollough, M., et al. 2002, MNRAS, 331, 765, doi: 10.1046/j.1365-8711.2002.05230.x

Burleigh, M. R., & Jordan, S. 1998, in American Astronomical Society Meeting Abstracts, Vol. 191, American Astronomical Society Meeting Abstracts #191, 15.11

Burrows, D. N., Hill, J. E., Nousek, J. A., et al. 2005, SSRv, 120, 165, doi: 10.1007/s11214-005-5097-2

Cadolle Bel, M., Prat, L., Rodriguez, J., et al. 2009, A&A, 501, 1, doi: 10.1051/0004-6361/200810744

Cannizzo, J. K. 1993, The Limit Cycle Instability in Dwarf Nova Accretion Disks, 6–40, doi: 10.1142/9789814350976_0002

Cannizzo, J. K., Chen, W., & Livio, M. 1995, ApJ, 454, 880, doi: 10.1086/176541

Capitanio, F., Belloni, T., Del Santo, M., & Ubertini, P. 2009, MNRAS, 398, 1194, doi: 10.1111/j.1365-2966.2009.15196.x

Castro, M., D'Amico, F., Braga, J., et al. 2014, A&A, 569, A82, doi: 10.1051/0004-6361/201323290

Chakrabarti, S., & Titarchuk, L. G. 1995, ApJ, 455, 623, doi: 10.1086/176610

Chakrabarti, S. K. 1989, ApJ, 347, 365, doi: 10.1086/168125

—. 1990, Theory of Transonic Astrophysical Flows, doi: 10.1142/1091

—. 1996, ApJ, 464, 664, doi: 10.1086/177354

—. 1997, ApJ, 484, 313, doi: 10.1086/304325

Chakrabarti, S. K., Debnath, D., & Nagarkoti, S. 2019, Advances in Space Research, 63, 3749, doi: 10.1016/j.asr.2019.02.014

Chakrabarti, S. K., & Mandal, S. 2006, ApJL, 642, L49, doi: 10.1086/504319

Chandrasekhar, S. 1939, Ciel et Terre, 55, 412

Chatterjee, D., Debnath, D., Chakrabarti, S. K., Mondal, S., & Jana, A. 2016, ApJ, 827, 88, doi: 10.3847/0004-637X/827/1/88

Chaty, S., Muñoz Arjonilla, A. J., & Dubus, G. 2015, A&A, 577, A101, doi: 10.1051/0004-6361/201424004

Chen, W., Livio, M., & Gehrels, N. 1993, ApJL, 408, L5, doi: 10.1086/186817

Chen, X., & Taam, R. E. 1993, ApJ, 412, 254, doi: 10.1086/172916

Chen, Y. P., Zhang, S., Torres, D. F., et al. 2010, A&A, 522, A99, doi: 10.1051/0004-6361/201014017

Colpi, M., Maraschi, L., & Treves, A. 1984, ApJ, 280, 319, doi: 10.1086/161998

Connors, R. M. T., van Eijnatten, D., Markoff, S., et al. 2019, MNRAS, doi: 10.1093/mnras/stz604

Corbel, S. 2011, in IAU Symposium, Vol. 275, Jets at All Scales, ed. G. E. Romero, R. A. Sunyaev, & T. Belloni, 205–214, doi: 10.1017/S1743921310016054

Corbel, S., Coriat, M., Brocksopp, C., et al. 2013, MNRAS, 428, 2500, doi: 10.1093/mnras/sts215

Corbel, S., & Fender, R. P. 2002, ApJL, 573, L35, doi: 10.1086/341870

Corbel, S., Fender, R. P., Tomsick, J. A., Tzioumis, A. K., & Tingay, S. 2004, ApJ, 617, 1272, doi: 10.1086/425650

Corbel, S., Kaaret, P., Fender, R. P., et al. 2005, ApJ, 632, 504, doi: 10.1086/432499

Corbel, S., Nowak, M. A., Fender, R. P., Tzioumis, A. K., & Markoff, S. 2003, A&A, 400, 1007, doi: 10.1051/0004-6361:20030090

Coriat, M., Corbel, S., Prat, L., et al. 2011, MNRAS, 414, 677, doi: 10.1111/j.1365-2966.2011.18433.x

Corral-Santana, J. M., Casares, J., Muñoz-Darias, T., et al. 2016, A&A, 587, A61, doi: 10.1051/0004-6361/201527130

Cowley, A. P., Schmidtke, P. C., Hutchings, J. B., & Crampton, D. 2002, AJ, 123, 1741, doi: 10.1086/339028

de Korte, P. A. J., Bleeker, J. A. M., den Boggende, A. J. F., et al. 1981, SSRv, 30, 495, doi: 10.1007/BF01246070

Debnath, D., Chakrabarti, S. K., & Nandi, A. 2010, A&A, 520, A98, doi: 10.1051/0004-6361/201014990

—. 2013, Advances in Space Research, 52, 2143, doi: 10.1016/j.asr.2013.09.002

del Santo, M., Bazzano, A., Zdziarski, A. A., et al. 2005, A&A, 433, 613, doi: 10.1051/0004-6361:20042058

Dickey, J. M., & Lockman, F. J. 1990, ARA&A, 28, 215, doi: 10.1146/annurev.aa.28.090190.001243

Dogiel, V., Cheng, K.-S., Chernyshov, D., et al. 2009, PASJ, 61, 901, doi: 10.1093/pasj/61.4.901

Done, C., Gierliński, M., & Kubota, A. 2007, A&ARv, 15, 1, doi: 10.1007/s00159-007-0006-1

Eardley, D. M., Lightman, A. P., & Shapiro, S. L. 1975, ApJL, 199, L153, doi: 10.1086/181871

Ebisawa, K. 1991, PhD thesis, Insititute of Space and Astronautical Science/Japan Aerospace Exploration Agency

Ebisawa, K., Ogawa, M., Aoki, T., et al. 1994, PASJ, 46, 375

Emelyanov, A. N., Aleksandrovich, N. L., & Sunyaev, R. A. 2000, Astronomy Letters, 26, 297, doi: 10.1134/1.20394

Esin, A. A., Lasota, J.-P., & Hynes, R. I. 2000, A&A, 354, 987

Fender, R., Corbel, S., Tzioumis, T., et al. 1999, ApJL, 519, L165, doi: 10.1086/312128

Fender, R. P. 2001, MNRAS, 322, 31, doi: 10.1046/j.1365-8711.2001.04080.x

Fender, R. P., Belloni, T. M., & Gallo, E. 2004, MNRAS, 355, 1105, doi: 10.1111/j.1365-2966.2004.08384.x

Fender, R. P., Gallo, E., & Jonker, P. G. 2003, MNRAS, 343, L99, doi: 10.1046/j.1365-8711.2003.06950.x

Fender, R. P., & Hendry, M. A. 2000, MNRAS, 317, 1, doi: 10.1046/j.1365-8711.2000.03443.x

Fender, R. P., Stirling, A. M., Spencer, R. E., et al. 2006, MNRAS, 369, 603, doi: 10.1111/j.1365-2966.2006.10193.x

Frank, J., King, A., & Raine, D. 1992, Accretion power in astrophysics., Vol. 21

Frank, J., King, A. R., Raine, D. J., & Shaham, J. 1986, Physics Today, 39, 124, doi: 10.1063/1.2815178

Fukue, J. 1987, PASJ, 39, 309

Fürst, F., Nowak, M. A., Tomsick, J. A., et al. 2015, ApJ, 808, 122, doi: 10.1088/0004-637X/808/2/122

Gallo, E. 2006, in VI Microquasar Workshop: Microquasars and Beyond, 9.1. https://arxiv.org/abs/astro-ph/0611413

Gallo, E., Fender, R. P., & Pooley, G. G. 2003, MNRAS, 344, 60, doi: 10.1046/j.1365-8711.2003.06791.x

García, J. A., Steiner, J. F., McClintock, J. E., et al. 2015, ApJ, 813, 84, doi: 10.1088/0004-637X/813/2/84

Giacconi, R., Kellogg, E., Gorenstein, P., Gursky, H., & Tananbaum, H. 1971, ApJL, 165, L27, doi: 10.1086/180711

Gilfanov, M., & Merloni, A. 2014, SSRv, 183, 121, doi: 10.1007/s11214-014-0071-5

Giri, K., & Chakrabarti, S. K. 2013, MNRAS, 430, 2836, doi: 10.1093/mnras/stt087

Giri, K., Garain, S. K., & Chakrabarti, S. K. 2015, MNRAS, 448, 3221, doi: 10.1093/mnras/stv223

Goldwurm, A., Israël, D., Goldoni, P., et al. 2001, in American Institute of Physics Conference Series, Vol. 587, Gamma 2001: Gamma-Ray Astrophysics, ed. S. Ritz, N. Gehrels, & C. R. Shrader, 61–65, doi: 10.1063/1.1419372

Grimm, H. J., Gilfanov, M., & Sunyaev, R. 2002, A&A, 391, 923, doi: 10.1051/0004-6361:20020826

Haardt, F., & Maraschi, L. 1993, ApJ, 413, 507, doi: 10.1086/173020

Hameury, J. M., & Lasota, J. P. 2016, A&A, 594, A87, doi: 10.1051/0004-6361/201628434

Harrison, F. A., Boggs, S., Christensen, F., et al. 2010, in Society of Photo-Optical Instrumentation Engineers (SPIE) Conference Series, Vol. 7732, Space Telescopes and Instrumentation 2010: Ultraviolet to Gamma Ray, 77320S, doi: 10.1117/12.858065

Heida, M., Jonker, P. G., Torres, M. A. P., & Chiavassa, A. 2017, ApJ, 846, 132, doi: 10.3847/1538-4357/aa85df

Heindl, W. 2001, The Low/soft State in the Microquasar 1E1740.7-2942, Chandra Proposal

Hertz, P., & Wood, K. S. 1984, in Bulletin of the American Astronomical Society, Vol. 16, 469

Hirsch, M., Pottschmidt, K., Smith, D. M., et al. 2020, A&A, 636, A51, doi: 10.1051/0004-6361/201834647

Homan, J. 2001, PhD thesis, University of Amsterdam

Homan, J., & Belloni, T. 2005, Ap&SS, 300, 107, doi: 10.1007/s10509-005-1197-4

Homan, J., Miller, J. M., Wijnands, R., et al. 2005, ApJ, 623, 383, doi: 10.1086/424994

Hopman, C., Portegies Zwart, S. F., & Alexander, T. 2004, ApJL, 604, L101, doi: 10.1086/383616

Hynes, R. I. 2010, arXiv e-prints, arXiv:1010.5770. https://arxiv.org/abs/1010.5770

Hynes, R. I., Steeghs, D., Casares, J., Charles, P. A., & O'Brien, K. 2003, ApJL, 583, L95, doi: 10.1086/368108

—. 2004, ApJ, 609, 317, doi: 10.1086/421014

Ilovaisky, S. A., Chevalier, C., Motch, C., & Chiappetti, L. 1986, A&A, 164, 67

Iyer, N., Nandi, A., & Mandal, S. 2015, ApJ, 807, 108, doi: 10.1088/0004-637X/807/1/108

Jahoda, K., Markwardt, C. B., Radeva, Y., et al. 2006, ApJS, 163, 401, doi: 10.1086/500659

Jahoda, K., Swank, J. H., Giles, A. B., et al. 1996, in Society of Photo-Optical Instrumentation Engineers (SPIE) Conference Series, Vol. 2808, EUV, X-Ray, and Gamma-Ray Instrumentation for Astronomy VII, ed. O. H. Siegmund & M. A. Gummin, 59–70, doi: 10.1117/12.256034

Janiuk, A., & Czerny, B. 2011, MNRAS, 414, 2186, doi: 10.1111/j.1365-2966.2011.18544.x

Jansen, F., Lumb, D., Altieri, B., et al. 2001, A&A, 365, L1, doi: 10.1051/0004-6361:20000036

Jaroszynski, M., Abramowicz, M. A., & Paczynski, B. 1980, AcA, 30, 1

Joinet, A., Jourdain, E., Malzac, J., et al. 2005, ApJ, 629, 1008, doi: 10.1086/431576

Jonker, P. G., Miller-Jones, J., Homan, J., et al. 2010, MNRAS, 401, 1255, doi: 10.1111/j.1365-2966.2009.15717.x

Kalemci, E., Tomsick, J. A., Corbel, S., & Tzioumis, T. 2008, The Astronomer's Telegram, 1378, 1

Kalemci, E., Tomsick, J. A., Rothschild, R. E., et al. 2006, ApJ, 639, 340, doi: 10.1086/499222

Kaluzienski, L. J., & Holt, S. S. 1977, IAUC, 3099, 3

Katz, J. I. 1976, ApJ, 206, 910, doi: 10.1086/154455

Keck, J. W., Craig, W. W., Hailey, C. J., et al. 2001, ApJ, 563, 301, doi: 10.1086/323686

Kilic, M., Allende Prieto, C., Brown, W. R., & Koester, D. 2007, ApJ, 660, 1451, doi: 10.1086/514327

King, A. R., Kolb, U., & Burderi, L. 1996, ApJL, 464, L127, doi: 10.1086/310105

King, A. R., & Ritter, H. 1998, MNRAS, 293, L42, doi: 10.1046/j.1365-8711.1998.01295.x

Kong, A. K. H., Kuulkers, E., Charles, P. A., & Homer, L. 2000, MNRAS, 312, L49, doi: 10.1046/j.1365-8711.2000.03334.x

Kumar, R., & Chattopadhyay, I. 2013, MNRAS, 430, 386, doi: 10.1093/mnras/sts641

Lasota, J.-P. 2016, Astrophysics and Space Science Library, Vol. 440, Black Hole Accretion Discs, ed. C. Bambi, 1, doi: 10.1007/978-3-662-52859-4_1

Lattimer, J. M. 2012, Annual Review of Nuclear and Particle Science, 62, 485, doi: 10.1146/annurev-nucl-102711-095018

Levine, A. M., Bradt, H., Cui, W., et al. 1996, ApJL, 469, L33, doi: 10.1086/310260

Li, Z. B., Zhang, S., Qu, J. L., et al. 2013, MNRAS, 433, 412, doi: 10.1093/mnras/stt737

Lin, D., Smith, I. A., Liang, E. P., et al. 2000, ApJ, 532, 548, doi: 10.1086/308553

Lipunova, G. V. 2015, ApJ, 804, 87, doi: 10.1088/0004-637X/804/2/87

Lochner, J. C., & Roussel-Dupre, D. 1994, ApJ, 435, 840, doi: 10.1086/174863

Longair, M. S. 2011, High Energy Astrophysics

Ludlam, R. M., Miller, J. M., & Cackett, E. M. 2015, ApJ, 806, 262, doi: 10.1088/0004-637X/806/2/262

Luque-Escamilla, P. L., Martí, J., & Muñoz-Arjonilla, Á. J. 2014, ApJL, 797, L1, doi: 10.1088/2041-8205/797/1/L1

Lutovinov, A., Revnivtsev, M., Molkov, S., & Sunyaev, R. 2005, A&A, 430, 997, doi: 10.1051/0004-6361:20041677

Lynden-Bell, D. 1978, Physica Scripta, 17, 185, doi: 10.1088/0031-8949/17/3/009

Maejima, Y., Makishima, K., Matsuoka, M., et al. 1984, ApJ, 285, 712, doi: 10.1086/162549

Makishima, K., Maejima, Y., Mitsuda, K., et al. 1986, ApJ, 308, 635, doi: 10.1086/164534

Mandal, S., & Chakrabarti, S. K. 2005, A&A, 434, 839, doi: 10.1051/0004-6361:20041235

—. 2010, ApJL, 710, L147, doi: 10.1088/2041-8205/710/2/L147

Mandrou, P. 1990, IAUC, 5032, 1

Marcel, G., Ferreira, J., Petrucci, P.-O., et al. 2018, A&A, 617, A46, doi: 10.1051/0004-6361/201833124

Markert, T. H., Canizares, C. R., Clark, G. W., et al. 1973, ApJL, 184, L67, doi: 10.1086/181290

Markoff, S., Nowak, M. A., & Wilms, J. 2005, ApJ, 635, 1203, doi: 10.1086/497628

Martí, J., Luque-Escamilla, P. L., Bosch-Ramon, V., & Paredes, J. M. 2017, Nature Communications, 8, 1757, doi: 10.1038/s41467-017-01976-5

Matsuoka, M., Kawasaki, K., Ueno, S., et al. 2009, PASJ, 61, 999, doi: 10.1093/pasj/61.5.999

McClintock, J. E., & Remillard, R. A. 2006, Black hole binaries, ed. W. H. G. Lewin & M. van der Klis, 157–213

McClintock, J. E., Remillard, R. A., Rupen, M. P., et al. 2009, ApJ, 698, 1398, doi: 10.1088/0004-637X/698/2/1398

Méndez, M., & van der Klis, M. 1997, ApJ, 479, 926, doi: 10.1086/303914

Mereghetti, S., Cremonesi, D. I., Haardt, F., et al. 1997, ApJ, 476, 829, doi: 10.1086/303659

Meyer, F., & Meyer-Hofmeister, E. 1981, A&A, 104, L10

Miller, J. M., Raymond, J., Fabian, A., et al. 2006a, Natur, 441, 953, doi: 10.1038/nature04912

Miller, J. M., Raymond, J., Homan, J., et al. 2006b, ApJ, 646, 394, doi: 10.1086/504673

Miller, J. M., Reynolds, C. S., Fabian, A. C., et al. 2008, ApJL, 679, L113, doi: 10.1086/589446

Miller-Jones, J. C. A., Sivakoff, G. R., Altamirano, D., et al. 2012, MNRAS, 421, 468, doi: 10.1111/j.1365-2966.2011.20326.x

Mirabel, I. F., & Rodríguez, L. F. 1994, in American Institute of Physics Conference Series, Vol. 304, American Institute of Physics Conference Series, ed. C. E. Fichtel, N. Gehrels, & J. P. Norris, 413–420, doi: 10.1063/1.45597

Mirabel, I. F., Rodriguez, L. F., Cordier, B., Paul, J., & Lebrun, F. 1992, Natur, 358, 215, doi: 10.1038/358215a0

Mitsuda, K., Inoue, H., Koyama, K., et al. 1984, PASJ, 36, 741

Mitsuda, K., Bautz, M., Inoue, H., et al. 2007, PASJ, 59, S1, doi: 10.1093/pasj/59.sp1.S1

Miyamoto, S., Kimura, K., Kitamoto, S., Dotani, T., & Ebisawa, K. 1991, ApJ, 383, 784, doi: 10.1086/170837

Miyamoto, S., Kitamoto, S., Hayashida, K., & Egoshi, W. 1995, ApJL, 442, L13, doi: 10.1086/187804

Molla, A. A., Chakrabarti, S. K., Debnath, D., & Mondal, S. 2017, ApJ, 834, 88, doi: 10.3847/1538-4357/834/1/88

Mondal, S., & Chakrabarti, S. K. 2013, MNRAS, 431, 2716, doi: 10.1093/mnras/stt361

Mondal, S., Debnath, D., & Chakrabarti, S. K. 2014, ApJ, 786, 4, doi: 10.1088/0004-637X/786/1/4

Motta, S., Belloni, T., & Homan, J. 2009, MNRAS, 400, 1603, doi: 10.1111/j.1365-2966.2009.15566.x

Motta, S., Muñoz-Darias, T., & Belloni, T. 2010, MNRAS, 408, 1796, doi: 10.1111/j.1365-2966.2010.17246.x

Motta, S., Muñoz-Darias, T., Casella, P., Belloni, T., & Homan, J. 2011, MNRAS, 418, 2292, doi: 10.1111/j.1365-2966.2011.19566.x

Muñoz-Arjonilla, A. J., Martí, J., Luque-Escamilla, P. L., et al. 2010, A&A, 519, A15, doi: 10.1051/0004-6361/201014211

Muñoz-Darias, T., Casares, J., & Martínez-Pais, I. G. 2008, MNRAS, 385, 2205, doi: 10.1111/j.1365-2966.2008.12987.x

Muñoz-Darias, T., Coriat, M., Plant, D. S., et al. 2013, MNRAS, 432, 1330, doi: 10.1093/mnras/stt546

Nandi, A., Debnath, D., Mandal, S., & Chakrabarti, S. K. 2012, A&A, 542, A56, doi: 10.1051/0004-6361/201117844

Nandi, A., Mandal, S., Sreehari, H., et al. 2018, Ap&SS, 363, 90, doi: 10.1007/s10509-018-3314-1

Narayan, R., & Yi, I. 1994, ApJL, 428, L13, doi: 10.1086/187381

—. 1995, ApJ, 452, 710, doi: 10.1086/176343

Natalucci, L., Tomsick, J., Bazzano, A., et al. 2014, in American Astronomical Society Meeting Abstracts, Vol. 223, American Astronomical Society Meeting Abstracts #223, 438.18

Novikov, I. D., & Thorne, K. S. 1973, in Black Holes (Les Astres Occlus), ed. C. Dewitt & B. S. Dewitt, 343–450

Nowak, M. A. 2000, MNRAS, 318, 361, doi: 10.1046/j.1365-8711.2000.03668.x

Obst, M., Pottschmidt, K., Lohfink, A., et al. 2011, Acta Polytechnica, 51, 49

Osaki, Y. 1974, PASJ, 26, 429

Paczyński, B., & Wiita, P. J. 1980, A&A, 500, 203

Parker, M. L., Tomsick, J. A., Kennea, J. A., et al. 2016, ApJL, 821, L6, doi: 10.3847/2041-8205/821/1/L6

Parmar, A. N., Angelini, L., & White, N. E. 1995, ApJL, 452, L129, doi: 10.1086/309730

Pétri, J. 2008, Ap&SS, 318, 181, doi: 10.1007/s10509-008-9916-2

Petrucci, P. O., Merloni, A., Fabian, A., Haardt, F., & Gallo, E. 2001, MNRAS, 328, 501, doi: 10.1046/j.1365-8711.2001.04897.x

Piraino, S., Santangelo, A., Ford, E. C., & Kaaret, P. 1999, A&A, 349, L77. https://arxiv.org/abs/astro-ph/9910115

Plant, D. S., Fender, R. P., Ponti, G., Muñoz-Darias, T., & Coriat, M. 2014, MNRAS, 442, 1767, doi: 10.1093/mnras/stu867

Ponti, G., Fender, R. P., Begelman, M. C., et al. 2012, MNRAS, 422, L11, doi: 10.1111/j.1745-3933.2012.01224.x

Ponti, G., Muñoz-Darias, T., & Fender, R. P. 2014, MNRAS, 444, 1829, doi: 10.1093/mnras/stu1742

Portegies Zwart, S. F., Dewi, J., & Maccarone, T. 2004, MNRAS, 355, 413, doi: 10.1111/j.1365-2966.2004.08327.x

Pottschmidt, K., Chernyakova, M., Zdziarski, A. A., et al. 2006, A&A, 452, 285, doi: 10.1051/0004-6361:20054077

Pottschmidt, K., Chernyakova, M., Lubiński, P., et al. 2008, in The 7th INTEGRAL Workshop, 98

Prat, L., Rodriguez, J., Cadolle Bel, M., et al. 2009, A&A, 494, L21, doi: 10.1051/0004-6361:200811393

Radhika, D., & Nandi, A. 2014, Advances in Space Research, 54, 1678, doi: 10.1016/j.asr.2014.06.039

Rees, M. J., Begelman, M. C., Blandford, R. D., & Phinney, E. S. 1982, Natur, 295, 17, doi: 10.1038/295017a0

Remillard, R. A., & McClintock, J. E. 2006, ARA&A, 44, 49, doi: 10.1146/annurev.astro.44.051905.092532

Remillard, R. A., McClintock, J. E., Orosz, J. A., & Levine, A. M. 2006, ApJ, 637, 1002, doi: 10.1086/498556

Reynolds, A. P., Parmar, A. N., Hakala, P. J., et al. 1999, A&AS, 134, 287, doi: 10.1051/aas:1999140

Rhoades, C. E., & Ruffini, R. 1974, PRL, 32, 324, doi: 10.1103/PhysRevLett.32.324

Rodriguez, L. F., Mirabel, I. F., & Marti, J. 1992, ApJL, 401, L15, doi: 10.1086/186659

Rothschild, R. E., Blanco, P. R., Gruber, D. E., et al. 1998, ApJ, 496, 538, doi: 10.1086/305377

Rothstein, D. M., Eikenberry, S. S., Chatterjee, S., et al. 2002, ApJL, 580, L61, doi: 10.1086/345546

Rupen, M. P., Mioduszewski, A. J., & Dhawan, V. 2005, The Astronomer's Telegram, 490, 1

Rupen, M. P., Mioduszewski, A. J., & Dhawan, V. D. 2004, in American Astronomical Society Meeting Abstracts, Vol. 204, American Astronomical Society Meeting Abstracts #204, 05.16

Russell, D. M., Gallo, E., & Fender, R. P. 2013, MNRAS, 431, 405, doi: 10.1093/mnras/stt176

Rybicki, G. B., & Lightman, A. P. 1979, Radiative processes in astrophysics

Sakano, M., Imanishi, K., Tsujimoto, M., Koyama, K., & Maeda, Y. 1999, ApJ, 520, 316, doi: 10.1086/307441

Schanne, S., Cordier, B., Gros, M., et al. 2003, in Society of Photo-Optical Instrumentation Engineers (SPIE) Conference Series, Vol. 4851, X-Ray and Gamma-Ray Telescopes and Instruments for Astronomy., ed. J. E. Truemper & H. D. Tananbaum, 1132–1143, doi: 10.1117/12.461604

Shahbaz, T., Charles, P. A., & King, A. R. 1998, MNRAS, 301, 382, doi: 10.1046/j.1365-8711.1998.01991.x

Shahbaz, T., & Kuulkers, E. 1998, MNRAS, 295, L1, doi: 10.1046/j.1365-8711.1998.29511221.x

Shakura, N. I., & Sunyaev, R. A. 1973, A&A, 500, 33

Shapiro, S. L., & Teukolsky, S. A. 1984, S&T, 67, 238

Sheth, S., Liang, E., Luo, C., & Murakami, T. 1996, ApJ, 468, 755, doi: 10.1086/177731

Shimura, T., & Takahara, F. 1995, ApJ, 445, 780, doi: 10.1086/175740

Singh, K. P., Stewart, G. C., Westergaard, N. J., et al. 2017, Journal of Astrophysics and Astronomy, 38, 29, doi: 10.1007/s12036-017-9448-7

Skinner, G. K., Willmore, A. P., Eyles, C. J., Bertram, D., & Church, M. J. 1987, Natur, 330, 544, doi: 10.1038/330544a0

Smith, D. M., Dawson, D. M., & Swank, J. H. 2007, ApJ, 669, 1138, doi: 10.1086/521822

Smith, D. M., Heindl, W. A., Markwardt, C. B., & Swank, J. H. 2001, ApJL, 554, L41, doi: 10.1086/320928

Smith, D. M., Heindl, W. A., Swank, J., et al. 1997, ApJL, 489, L51, doi: 10.1086/310963

Smith, D. M., Heindl, W. A., & Swank, J. H. 2002a, ApJ, 569, 362, doi: 10.1086/339167

—. 2002b, ApJL, 578, L129, doi: 10.1086/344701

Soria, R., Broderick, J. W., Hao, J., et al. 2011, MNRAS, 415, 410, doi: 10.1111/j.1365-2966.2011.18714.x

Spitzer, L. 1965, Physics of fully ionized gases

Sreehari, H., Iyer, N., Radhika, D., Nandi, A., & Mandal, S. 2019, Advances in Space Research, 63, 1374, doi: 10.1016/j.asr.2018.10.042

Stecchini, P. E., D'Amico, F., Jablonski, F., Castro, M., & Braga, J. 2020, MNRAS, 493, 2694, doi: 10.1093/mnras/staa417

Steeghs, D., Miller, J. M., Kaplan, D., & Rupen, M. 2003, The Astronomer's Telegram, 146, 1

Steiner, J. F., McClintock, J. E., & Reid, M. J. 2012, ApJL, 745, L7, doi: 10.1088/2041-8205/745/1/L7

Steiner, J. F., Remillard, R. A., García, J. A., & McClintock, J. E. 2016, ApJL, 829, L22, doi: 10.3847/2041-8205/829/2/L22

Stiele, H., Motta, S., Muñoz-Darias, T., & Belloni, T. M. 2011, MNRAS, 418, 1746, doi: 10.1111/j.1365-2966.2011.19616.x

Stoeger, W. R. 1978, MNRAS, 182, 647, doi: 10.1093/mnras/182.4.647

—. 1980, ApJ, 235, 216, doi: 10.1086/157626

Strüder, L., Briel, U., Dennerl, K., et al. 2001, A&A, 365, L18, doi: 10.1051/0004-6361:20000066

Sun, W.-H., & Malkan, M. A. 1989, ApJ, 346, 68, doi: 10.1086/167986

Sunyaev, R., & Revnivtsev, M. 2000, A&A, 358, 617. https://arxiv.org/abs/astro-ph/0003308

Sunyaev, R., Churazov, E., Gilfanov, M., et al. 1991, ApJL, 383, L49, doi: 10.1086/186238

Sunyaev, R. A., & Titarchuk, L. G. 1980, A&A, 500, 167

—. 1985, A&A, 143, 374

Swank, J. 2004, The Astronomer's Telegram, 301, 1

Swank, J. H., Remillard, R., & Markwardt, C. B. 2005, The Astronomer's Telegram, 576, 1

Tanaka, Y., & Shibazaki, N. 1996, ARA&A, 34, 607, doi: 10.1146/annurev.astro.34.1.607

Tetarenko, B. E., Dubus, G., Lasota, J. P., Heinke, C. O., & Sivakoff, G. R. 2018a, MNRAS, 480, 2, doi: 10.1093/mnras/sty1798

Tetarenko, B. E., Lasota, J. P., Heinke, C. O., Dubus, G., & Sivakoff, G. R. 2018b, Natur, 554, 69, doi: 10.1038/nature25159

Tetarenko, B. E., Sivakoff, G. R., Heinke, C. O., & Gladstone, J. C. 2016, ApJS, 222, 15, doi: 10.3847/0067-0049/222/2/15

Thorne, K. S., & Price, R. H. 1975, ApJL, 195, L101, doi: 10.1086/181720

Titarchuk, L. 1994, ApJ, 434, 570, doi: 10.1086/174760

Tomsick, J. A., Kalemci, E., Corbel, S., & Kaaret, P. 2003, ApJ, 592, 1100, doi: 10.1086/375811

Truemper, J. 1982, Advances in Space Research, 2, 241, doi: 10.1016/0273-1177(82)90070-9

Turner, M. J. L., Abbey, A., Arnaud, M., et al. 2001, A&A, 365, L27, doi: 10.1051/0004-6361:20000087

Tursunov, A. A., & Kološ, M. 2018, Physics of Atomic Nuclei, 81, 279, doi: 10.1134/S1063778818020187

Ueda, Y., Murakami, H., Yamaoka, K., Dotani, T., & Ebisawa, K. 2004, ApJ, 609, 325, doi: 10.1086/420973

van Paradijs, J. 1996, ApJL, 464, L139, doi: 10.1086/310100

van Paradijs, J., & McClintock, J. E. 1994, A&A, 290, 133

Verner, D. A., Ferland, G. J., Korista, K. T., & Yakovlev, D. G. 1996, ApJ, 465, 487, doi: 10.1086/177435

Vyas, M. K., & Chattopadhyay, I. 2017, MNRAS, 469, 3270, doi: 10.1093/mnras/stx967

Weisskopf, M. C., Tananbaum, H. D., Van Speybroeck, L. P., & O'Dell, S. L. 2000, in Society of Photo-Optical Instrumentation Engineers (SPIE) Conference Series, Vol. 4012, X-Ray Optics, Instruments, and Missions III, ed. J. E. Truemper & B. Aschenbach, 2–16, doi: 10.1117/12.391545

Wilms, J., Allen, A., & McCray, R. 2000, The Astrophysical Journal, 542, 914, doi: 10.1086/317016

Wilms, J., Allen, A., & McCray, R. 2000, ApJ, 542, 914, doi: 10.1086/317016

Winter, L. M., Mushotzky, R. F., & Reynolds, C. S. 2006, ApJ, 649, 730, doi: 10.1086/506579

Xue, Y. Q., & Cui, W. 2007, A&A, 466, 1053, doi: 10.1051/0004-6361:20066791

Yadav, J. S., Misra, R., Verdhan Chauhan, J., et al. 2016, ApJ, 833, 27, doi: 10.3847/0004-637X/833/1/27

Yan, M., & Dalgarno, A. 1997, ApJ, 481, 296, doi: 10.1086/304034

Yu, W., van der Klis, M., & Fender, R. 2004, ApJL, 611, L121, doi: 10.1086/423953

Zdziarski, A. A. 1998, MNRAS, 296, L51, doi: 10.1046/j.1365-8711.1998.01682.x

Zdziarski, A. A., Gierliński, M., Mikołajewska, J., et al. 2004, MNRAS, 351, 791, doi: 10.1111/j.1365-2966.2004.07830.x

Zdziarski, A. A., Lubiński, P., Gilfanov, M., & Revnivtsev, M. 2003, MNRAS, 342, 355, doi: 10.1046/j.1365-8711.2003.06556.x

Zdziarski, A. A., Poutanen, J., Mikolajewska, J., et al. 1998, MNRAS, 301, 435, doi: 10.1046/j.1365-8711.1998.02021.x

Zhang, S. N., Harmon, B. A., & Liang, E. P. 1997, in American Institute of Physics Conference Series, Vol. 410, Proceedings of the Fourth Compton Symposium, ed. C. D. Dermer, M. S. Strickman, & J. D. Kurfess, 873–877, doi: 10.1063/1.54155

Zhou, J. N., Liu, Q. Z., Chen, Y. P., et al. 2013, MNRAS, 431, 2285, doi: 10.1093/mnras/stt326

List of Publications

Refereed Journals

1. **Aneesha U.**, Samir Mandal, & Sreehari H (2019), "Study of the long-term evolution of the accretion dynamics of GX 339-4", **MNRAS**, 486, 2705

2. **Aneesha U.**, Samir Mandal (2020), "Spectral and accretion evolution of H1743-322 during outbursts in RXTE era", **Astronomy & Astrophysics**, 637, A47

3. Bhuvana G. R., **Aneesha, U.** et al., (2020), "AstroSat view of persistent black holes GRS 1758-258 and 1E 1740.7-2942", **MNRAS** (under preparation)

Appendix A

Observation Log

Table A1: XMM-Newton, Swift/XRT and RXTE Simultaneous Observation Catalog of GX 339-4

2002/03 outburst			
XMM Obs Id	XMM Obs date (MJD)	RXTE Obs Id	RXTE Obs date (MJD)
0148220301	52718.055	50117-01-04-02	52718.173
0148220201	52706.731	50117-01-03-01	52706.840
2006/07 outburst			
XRT Obs Id	XRT Obs date (MJD)	RXTE Obs Id	RXTE Obs date (MJD)
00030919001	54213.031	92704-03-02-00	54213.387
00030919002	54216.520	92704-03-01-02	54216.939
00030919003	54220.071	92704-03-05-01	54220.226
00030919005	54227.298	92704-03-08-01	54227.613
00030919006	54231.913	92704-03-10-00	54231.604
00030919007	54234.922	92704-03-11-00	54234.837
00030919008	54237.331	92704-04-01-03	54237.290
00030919010	54240.884	92704-03-13-02	54240.301
00030919012	54244.715	92704-03-14-03	54244.971
00030943001	54245.711	92704-04-02-00	54245.749
2010/11 outburst			
XRT Obs Id	XRT Obs date (MJD)	RXTE Obs Id	RXTE Obs date (MJD)
00030943005	55217.673	95409-01-02-02	55217.810
00030943006	55259.964	95409-01-08-03	55259.791
00030943007	55260.240	95409-01-09-04	55260.071

00030943008	55260.518	95409-01-09-05	55260.445
00030943010	55261.044	95409-01-09-06	55261.189
00030943011	55281.744	95409-01-12-00	55281.581
00030943012	55285.733	95409-01-12-02	55285.778
00030943013	55289.302	95409-01-13-00	55289.618
00030943014	55293.036	95409-01-13-01	55293.087
00030943015	55297.782	95409-01-14-02	55297.874
00030943016	55301.388	95409-01-14-07	55300.919
00030943017	55301.789	95409-01-14-05	55301.790
00030943018	55302.411	95409-01-15-00	55302.196
00030943019	55302.800	95409-01-15-00	55302.196
00030943020	55303.809	95409-01-15-01	55303.604
00031687002	55316.986	95409-01-17-00	55316.115
00031687005	55334.061	95409-01-19-04	55334.382
00031687010	55366.381	95409-01-24-01	55366.514

Table A2: Observation Log for AstroSat/SXT of GRS 1758-258

Date(MJD)	Orbit	Segment	Start Time (UTC hh:mm:ss)	Stop Time (UTC hh:mm:ss)	Exposure(s)
2016-10-14(57675.68)	05663	01	16:24:05.022	16:42:50.690	1124.5
2016-10-15(57676.15)	05671	01	03:46:09.553	03:58:01.423	710.8
2016-10-15(57676.22)	05671	02	05:23:36.633	05:40:31.814	1015.1
2016-10-15(57676.29)	05673	01	07:01:04.010	07:19:47.242	1122.1
2016-10-15(57676.36)	05673	02	08:38:39.382	08:57:13.100	1112.6
2016-10-15(57676.69)	05678	01	16:46:06.965	17:04:19.761	1091.2
2016-10-15(57676.76)	05678	02	18:23:35.653	18:39:10.113	934.34

2016-10-15(57676.76)	05682	01	18:23:42.914	18:41:45.833	1081.7
2016-10-15(57676.83)	05682	02	20:03:31.573	20:18:58.788	927.21
2016-10-15(57676.90)	05682	03	21:48:00.781	21:56:41.447	520.66
2017-07-28(57962.26)	09904	01	06:18:17.786	06:48:31.798	1814.0
2017-07-28(57962.33)	09910	01	07:55:58.026	08:35:30.814	2372.7
2017-07-28(57962.39)	09910	02	09:33:09.841	10:15:14.717	2524.8
2017-07-28(57962.46)	09910	03	11:10:35.987	11:52:41.782	2484.4
2017-07-28(57962.53)	09910	04	12:48:20.000	13:30:09.220	2467.8
2017-07-28(57962.60)	09910	05	14:25:35.164	15:07:35.380	2520.1
2017-07-28(57962.66)	09910	06	16:03:02.539	16:45:01.438	2517.7
2017-07-28(57962.73)	09910	07	17:40:26.250	17:59:09.390	1122.6
2017-09-20(58016.53)	10708	01	12:50:40.764	13:14:05.850	1405.0
2017-09-20(58016.87)	10713	01	21:04:32.330	21:21:13.609	1000.9
2017-09-20(58016.95)	10713	02	22:49:01.732	22:58:37.080	575.34
2018-04-08 (58216.35)	13665	01	08:25:15.01	09:35:36.58	1046.08
2018-04-08 (58216.46)	13667	01	11:05:47.02	13:13:06.10	1721.29
2018-04-08 (58216.59)	13669	01	14:22:11.75	16:41:44.95	1726.04
2018-04-08 (58216.82)	13672	01	19:46:11.84	21:53:25.59	1730.80
2018-04-08 (58216.89)	13673	01	21:24:56.44	23:38:37.57	1600.00
2018-04-08 (58216.95)	13675	01	22:55:38.09	01:21:15.08	1084.12
2018-04-09 (58217.03)	13676	01	00:51:04.00	03:11:29.12	779.81
2018-04-09 (58217.26)	13679	01	06:21:09.82	08:19:18.99	696.59
2018-04-09 (58217.33)	13680	01	07:59:54.26	09:56:40.78	1212.51
2018-04-09 (58217.40)	13681	01	09:41:05.91	11:34:32.96	1723.66
2018-04-09 (58217.54)	13683	01	13:00:43.69	15:19:28.97	1742.68
2018-04-09 (58217.61)	13684	01	14:47:35.59	17:06:23.15	1699.89
2018-04-10 (58218.36)	13694	01	06:45:31.53	08:40:59.09	832.11
2018-04-10 (58218.42)	13696	01	10:08:42.69	11:55:49.06	1756.95

Table A3: Observation Log for AstroSat/SXT/LAXPC for 1E 1740.7−2942.

Date(MJD)	Orbit	Instrument	Segment	Start Time (UTC hh:mm:ss)	Stop Time (UTC hh:mm:ss)	Exposure(s)
2016-10-06(57667)	5547	SXT	1	21:47:30.03	21:56:27.34	537.3
		LAXPC	2	21:48:24.73	21:56:05.07	460.343
2016-10-06(57667)	5548	SXT	1	21:47:30.03	21:56:01.22	499.7
		LAXPC	1	21:48:24.73	21:56:05.07	460.343
2016-10-07(57668)	5556	SXT	2	02:30:15.13	02:42:32.15	737
		LAXPC	2	01:47:40.11	02:28:42.61	2462.49
		SXT	3	04:08:58.69	04:25:30.86	991.4
		LAXPC	3	03:25:05.68	04:13:12.30	2886.62
		SXT	4	05:45:16.85	06:03:06.69	1053.2
		LAXPC	4	05:02:31.51	05:57:42.00	3310.5
2016-10-07(57668)	5557	SXT	1	07:22:28.61	07:40:58.89	1081.7
		LAXPC	1	07:06:11.04	07:40:42.34	2071.3
		SXT	2	09:00:15.76	09:18:29.51	1093.6
		LAXPC	2	08:17:23.14	09:18:08.79	3645.64
		SXT	3	10:38:00.76	10:55:55.39	1074.6
		LAXPC	3	09:59:56.03	10:55:34.78	3338.76
		SXT	4	12:15:47.72	12:33:18.88	1050.8
		LAXPC	4	11:44:33.11	12:33:01.03	2907.92

2016-10-07(57668)	5558	SXT	1	13:52:43.65	14:10:47.78	1084.1
		LAXPC	1	13:34:54.52	14:10:27.10	2132.57
2016-10-07(57668)	5561	SXT	1	15:30:12.00	15:48:16.19	1084.1
		LAXPC	13	15:13:20.86	15:47:53.68	2072.82
		SXT	2	17:07:23.27	17:14:27.54	423.1
		LAXPC	15	16:58:33.26	17:14:02.73	929.465
2018-02-25 (58174)	13047	SXT	1	14:40:03.83	15:24:05.33	1183.9
		LAXPC	1	14:44:24	15:19:10	2086.0
2018-02-25 (58174)	13049	SXT	1	16:22:19.80	16:42:19.80	1200.6
		LAXPC	2	16:21:50	17:03:42	2511.99
		SXT	2	18:00:39.80	18:18:59.80	1098.3
		LAXPC	3	17:59:15.00	18:48:11.00	2936.04
2018-02-25 (58174)	13050	SXT	1	19:14:46.37	21:21:34.06	1000.9
		LAXPC	1	19:36:40	20:32:40	3360.00
2018-02-26 (58175)	13054	SXT	1	00:30:10.52	02:35:35.37	962.8
		LAXPC	1	00:33:40	01:31:29	3469.05
		LAXPC	2	02:18:11	02:35:35	1044.06
2018-05-11 (58249)	14156	SXT	1	11:32:41.62	13:42:47.02	2448.7
		LAXPC	1	12:09:34	12:32:57	1403.05
	14158	SXT	1	15:02:46.48	17:08:46.69	2400
	14159	LAXPC	2	18:39:13	18:53:30	857.00
	14160	SXT	1	18:40:08.99	19:20:08.99	2400
		LAXPC	1	18:39:13	19:40:43	3690.06